CENTRO DE INVESTIGACIÓN Y DE ESTUDIOS AVANZADOS DEL INSTITUTO POLITÉCNICO NACIONAL

Unidad Mérida

DEPARTAMENTO DE FÍSICA APLICADA

"La búsqueda de celdas solares de ZnO sensibilizadas por tinte de alta eficiencia: interacciones en la interface semiconductor/tinte/par redox"

TESIS

Que presenta

M. en C. Esdras Josué Canto Aguilar

Para obtener el grado de

Doctor en Ciencias

en

Fisicoquímica

Director de Tesis:

Dr. Gerko Oskam

Mérida, Yucatán, México Marzo, 2018

CENTRO DE INVESTIGACIÓN Y DE ESTUDIOS AVANZADOS DEL INSTITUTO POLITÉCNICO NACIONAL

Unidad Mérida

DEPARTMENT OF APPLIED PHYSICS

"The quest for high efficiency ZnO-based dye-sensitized solar cells: Interactions at the semiconductor/dye/redox couple interface"

THESIS

Presented by

M. Sc. Esdras Josué Canto Aguilar

To obtain the degree of

Doctor of Science

in

Physical Chemistry

Thesis Director:

Dr. Gerko Oskam

Mérida, Yucatán, México March, 2018

Agradecimientos

A mi familia (Leonel, Irma y Jael) quienes han sido un apoyo constante en todos los aspectos de mi vida.

Al Dr. Gerko Oskam por todas sus enseñanzas, confianza y apoyo hacia mi trabajo durante tantos años; de igual manera que a todos los miembros del laboratorio de Nanomateriales (anteriores y actuales), cuya dinámica y compañerismo hizo de lo más llevadero y ameno hasta los momentos más atareados.

Al Dr. Frank E. Osterloh (UC-Davis, EUA) y Dr. Shogo Mori (Shinshu University, Japón) por la oportunidad de realizar estancias en sus respectivos laboratorios, experiencias de gran valor para mí.

Al Dr. Maximo Pech Canul, Dr. David Reyes Coronado, Dr. David Meneses y Dr. Ignacio González por sus invaluables observaciones y comentarios sobre el trabajo presentado.

Al CONACYT por la beca otorgada durante mi periodo de estudiante de doctorado en el departamento de física aplicada del CINVESTAV-Mérida

Agradezco el apoyo recibido por parte del Instituto de Energías Renovables (IER-UNAM), a través del Centro Mexicano de Innovación en Energía Solar (CeMIE-Sol), en el marco de la convocatoria 2013-02, del fondo sectorial CONACYT-SENER-SUSTENTABILIDAD ENERGÉTICA, dentro del proyecto estratégico No. 27, por medio del cual fue posible desarrollar la investigación y apoyar la formación de recursos humanos a nivel posgrado.

A todos: Gracias.

Resumen

La celda solar sensibilizada por tinte (DSSC) resulta ser un interesante sistema fotoelectroquímico cuyo desempeño se encuentra determinado por la optimización de las propiedades eléctricas del material transportador de electrones, las propiedades ópticas del absorbedor molecular y las características cinéticas y electroquímicas del par redox utilizado; sin embargo diferente a lo esperado teóricamente, interacciones complejas en las interfaces involucradas conducen a rendimientos aún por debajo de los observados en otras tecnologías fotovoltaicas. Los fenómenos que originan dichas interacciones y su efecto sobre los parámetros energéticos que definen la eficiencia de las celdas solares, y de forma específica en celdas solares basadas en ZnO, es el tema de estudio de este trabajo.

Hacia la fabricación de dispositivos económicamente redituables, la obtención de películas de ZnO mediante métodos electroquímicos ha sido de nuestro interés, por lo que parte de esta tesis presenta un estudio detallado sobre el efecto que la composición del baño electrolítico, aditivos, precursores y condiciones de depósito utilizadas tienen sobre la morfología y propiedades estructurales de los materiales depositados. El uso de tintes orgánicos y su combinación con diferentes tipos de pares redox ha sido abordado a lo largo de este trabajo, como una ruta viable hacia la obtención de dispositivos fotovoltaicos más eficientes al incrementar la absorción de luz y la cantidad de electrones colectados debido a las mejores propiedades de transporte teóricamente esperadas para el ZnO. La caracterización de los procesos de transferencia de carga y los mecanismos de recombinación involucrados en el funcionamiento de los dispositivos preparados en este trabajo mediante técnicas físicas y electroquímicas han dado pauta a la comprensión de las modestas eficiencias obtenidas, dejando claras directrices para el planteamiento y diseño de mejoras en dichos sistemas.

Abstract

The dye-sensitized solar cell (DSSC) is an interesting photoelectrochemical system whose performance is determined by an optimization of the electrical properties of the electron transporting layer, optical properties of the molecular absorber as well as the kinetics and electrochemical features of the redox couple used. However, in contrast to the theoretical results expected, complex interactions at the interfaces involved lead to low yields when comparing with other photovoltaic technologies. The phenomena that originate these interactions and their effect on the energetic parameters that define the efficiency of the dye-sensitized solar cells, and in specific that of ZnO-based solar cells, is the topic of interest in this work.

In order to move toward the fabrication of economically profitable devices, the synthesis of ZnO films through electrochemical methods has been of our interest; hence, part of this work presents a detailed study of the effect of the bath composition, additives, precursors and deposition conditions used on the morphology and structural features of the deposited materials. The use of organic dyes and their combination with different redox couples has been explored in this work as a viable route toward more efficient photovoltaic devices to increase the light absorption and the amount of the electrons collected, related to the better transport properties theoretically expected for ZnO. The characterization of the charge transfer processes and the recombination mechanisms involved in the operation of the devices prepared in this work through physical and electrochemical techniques has resulted in a better understanding of the modest efficiencies obtained, leading to clear guidelines for the planning and design of improvements in such systems.

Contents

1. Introduction

Currently, significant attention is given to the increasing global energy demand resulting from a constant acceleration in the rate of growth of the world population [1]. On the basis of such global emergency, great scientific and technological advances have been made in the field of renewable energies, driven by the idea of satisfying the consumption in an accessible and sustainable way. Between all the renewable energy sources at our disposal, the sun has shown to have the capacity to supply almost completely the energy required, and can be transformed to chemical, thermal or electrical energy.

For the last 50 years, photovoltaics, i.e. the conversion of solar energy to electricity, has been the dominant form of renewable energy in terms of research and installations, however, until recently the high cost of existing systems prevented a fast growth of the installed capacity. This has changed dramatically in the past 10 years, and photovoltaics is essentially cost effective and competitive with fossil fuels; the remaining obstacle is the high cost of investment up front. Solar cells have developed from single crystalline silicon and GaAs, to nanostructured, hybrid or all-organic materials in three generations: The first generation consists of bulk, single or polycrystalline high-purity semiconductors, mainly silicon, which still dominates the market. The second generation aims to lower the cost of the semiconductor materials by designing amorphous or thin film solar cells, of which the best known examples are CdS/CdTe (e.g. First Solar Inc; USA) and CIGS (Cu-In-Ga, S, Se). The third generation is based on novel concepts, nanomaterials, hybrid and organic materials, with as best known systems the dye-sensitized solar cell, organic photovoltaics (bulk heterojunction cells; small-molecule systems), and the very recent rise of the hybrid perovskite solar cell [2]. The main

advantages would be low cost of materials, fabrication methods, and easy installation, especially in niche applications.

In 1991, Brian O'Regan and Michael Grätzel reported on the construction of photovoltaic devices based on crystalline TiO_2 nanoparticles sensitized with a ruthenium complex as molecular absorber to harvest light, the dye-sensitized solar cell (DSSC). The ≈7% of conversion efficiency shown [3] generated expectations around the world, since DSSCs are based on inexpensive and stable materials, and especially because they can be prepared at low temperature conditions. These characteristics make DSSC an attractive solar technology with the promise of low production costs at large-scale. The DSSC is conformed by a nanostructured metal oxide film with high surface area, on which dye molecules are attached, embedded in an electrolyte solution with an appropriate redox couple. Hence, the solar cell combines nanotechnology, molecular light absorption, and photoelectrochemistry. The dye absorbs the light and transforms it in an electrical current through the nanostructured film to the external circuit; corresponding ion transport in the electrolyte solution in contact with the dye molecules and a counter electrode closes the circuit. As a result of the processes described above, an electrical current flows and, as a consequence, work can be performed, all this without changing the internal chemistry of the solar cell; i.e., the DSSC is a fully regenerative solar cell.

Nowadays, DSSCs have reached efficiencies as high as 14% [4], achieved by the optimization of the cell components and a better understanding of the mechanisms of generation and loss of electrons involved in the solar cell functioning. Based on this observation, the selection of the most promising components (the film material, the dye and

the redox couple) related with their single properties, is the starting point in the efficiency-improvement process.

We begin our efficiency-improvement process with the selection of ZnO as the electron transporting material, not only for its much better electrical properties (when comparing with the commonly used TiO_2 [5]), but also for the simple synthesis methods by which it can be obtained. However, by changing one component, all inter-related processes and kinetics change, which makes it necessary to re-evaluate all other components of the solar cell. The use of ZnO in DSSCs has been reported before in the literature [6–10], however, there are still many questions on the fundamental aspects governing their performance. Hence, in this project, we focus on several aspects of this system, by carefully designing the components of the solar cell, including several methods to prepare the ZnO substrate, several dyes as molecular absorbers, and several redox couples in the electrolyte solution.

In chapter 5 we study the preparation of ZnO films from $ZnCl_2$ and $Zn(NO_3)_2$ solutions by electrodeposition (a low temperature and scalable deposition technique), showing the effect that the deposition conditions and composition of the solutions have on the materials obtained. The combination of this material with organic dyes able to absorb higher amounts of light, promise an increase on the currents and voltages developed in the solar devices by increasing the light captured and diminishing the electron losses due to undesirable reactions at the interfaces formed by integration of all the components in the operative solar cell.

In parallel, our optimization process also tries to solve specific issues related with the ZnO, such as the poor chemical stability it shows in relatively acidic conditions, which usually depends on the nature of the dye used. Thus, chapter 6 evaluates the performance of an

organic dye that not only absorbs more light than the widely used ruthenium-based dyes, but also shows a less acidic character to work on the stability problem. In addition, its "bulky" structure allows us to consider to combine it with novel redox couples, such as the $[Co(bpy)_3]^{2+/3+}$ coordination complex to take advantage of the interesting kinetic and electrochemical properties they exhibit [11].

Chapter 7 takes this approach a step further, focusing on a series of non-acidic dyes that makes them excellent candidates to interact with ZnO. The high light absorption they also show, promise not only to overcome the ZnO stability issue, but also to increase the energetic parameters of the cell and, finally, the overall performance.

Hence, the following work evaluates the performance of ZnO-based systems that were carefully selected to give new insights in the factors that determine solar cell performance, and the results obtained have led us to develop more specific strategies to achieve more efficient ZnO-based DSSCs.

2. Background

2.1 Solar energy and solar cells

Solar energy has shown to be one of the most promising candidates to help cover the current energy demand, and this is because the sun irradiates the earth in one hour with more energy than the total energy consumed in one year [12]. From the total energy received by the earth, about 30% of this is reflected by clouds and particles present in the atmosphere, returning to outer space, 14% is absorbed by the atmosphere and only 56% reaches the surface of the earth, approximately 1000 W m^{-2} or 1 sun at sea level distributed along a broad range of wavelengths (fig. 1)

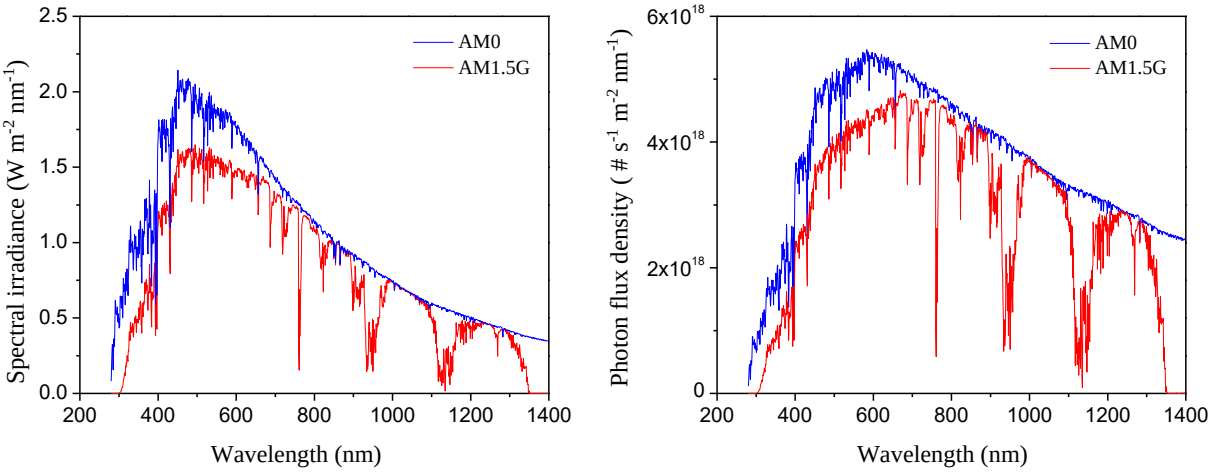

Figure 1.- a) Spectral irradiance and b) photon flux at the earth surface (AM1.5G) [13].

Solar cells are devices that transform solar energy into electricity, either directly via the photovoltaic effect, or indirectly through its transformation to heat or chemical energy.

Since its discovery, solar cells have evolved, basing their functioning on different technologies; thus, they can be classified in three generations, indicating their order of importance and historical relevance. The first generation of photovoltaic cells consisted of bulk single crystal semiconductor p-n junctions, generally silicon. Today this technology dominates the world production as well as the market. The second generation is based on the use of very thin, epitaxial semiconductor devices, with cadmium telluride (CdTe), thin films of amorphous and polycrystalline silicon, and $Cu(In,Ga)Se_2$ (CIGS), being the most investigated materials. In the third generation, the photovoltaic devices are based on new materials, including carbon nanotubes, nanocrystals, quantum dots, polymers and photoelectrochemical systems; in general, attractive emerging technologies due to the low cost projected for their large-scale production, as in the case of the dye sensitized solar cells (DSSCs) [2].

2.2 The dye sensitized solar cell (DSSC): Description, energetics and kinetics

The DSSC consists of a thin mesoporous and nanostructured metal oxide film (≈ 10 μm thick) with a wide band gap energy, sensitized to solar radiation by anchoring a large number of dye molecules with a high absorption coefficient in the visible on its surface. Upon light absorption an electron is injected from an excited dye molecule (D*) into the metal oxide conduction band, which travels through the nanostructured film toward the external circuit, and on to the counter electrode. After charge separation, an oxidized dye molecule (D^+) is generated, which is reduced to its original state (D^o) by an electron donor in the electrolytic

solution and, subsequently, the oxidized form of the electron donor travels to the counter electrode where it is regenerated, thus closing the cycle (graphically described in fig. 2).

The DSSC works on the principles of electron transfer processes between interfaces, for which the presence of a driving force is necessary. Hence, for the three main processes described here, the driving forces are given by the difference in the quasi-Fermi level of the semiconductor under illumination and the redox potential of the redox couple, the difference between the excited state level of the dye molecule and the position of the conduction band in the semiconductor, and the difference between the redox potential of the redox mediator and the redox potential of the ground state level in the dye (HOMO), for electron flow through the film, electron injection into the semiconductor, and the regeneration of the oxidized dye molecules, respectively.

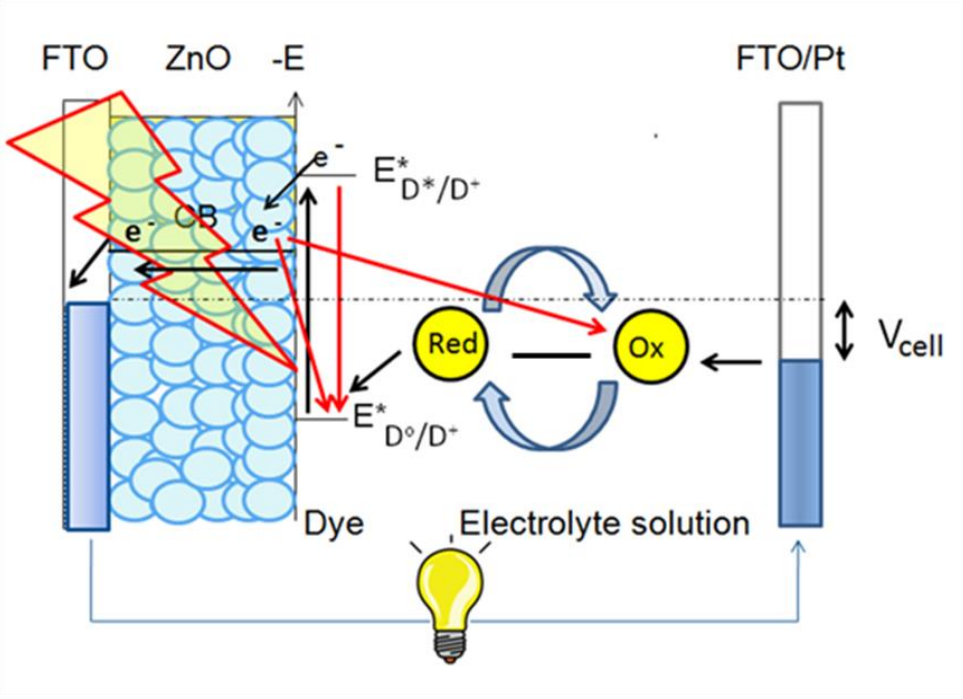

Figure 2.- Schematic diagram of the DSSC. The black arrows indicate the processes that lead to a photocurrent, while the red ones indicate the most important recombination pathways.

The efficiency of the electron transfer processes mentioned above depends on an effective competition with the main recombination mechanisms in the device; Table 1 summarizes these processes and their respective time constants.

Table 1.- Kinetics processes in DSSCs. The time constants were taken from reference [14].

Light absorption	$D° + h\nu \rightarrow D^*$	
Electron injection	$D^* \rightarrow D^+ + e^-$ (CB)	$\approx 10^{-11}$ s
Dye relaxation	$D^* \rightarrow D° + h\nu$	$\approx 10^{-8}$ s
Electron transport	e^-(CB)$\rightarrow e^-$(FTO)	$\approx 10^{-3}$ s
Dye regeneration	$D^+ + Red \rightarrow D° + Ox$	$\approx 10^{-6}$ s
recombination with the redox couple	e^-(CB)$+ Ox \rightarrow Red$	$\approx 10^{-2}$ s
recombination with the oxidized dye	e^- (CB)$+ D^+ \rightarrow D°$	$\approx 10^{-4}$ s
recombination from the bare FTO	e^-(FTO)$+ Ox \rightarrow Red$	

From table 1 it can be seen that if electron injection into the semiconductor is not fast enough, the relaxation of the excited dye molecule is the most favored process and, as a consequence, charge separation does not occur. Once the electrons have been injected, they can recombine from the semiconductor conduction band through two pathways: with the oxidized dye molecules attached on the semiconductor surface and with the electron acceptors in the electrolyte solution; however, dye regeneration is usually a fast and efficient process so that recombination with the acceptors in the electrolyte tends to be the most dominant electron loss mechanism. Thus, as explained before, in the design of the interfaces involved the energetic and kinetics features of each component have to be taken into account, and it is the

balance between the generation and loss process what determines the current density and voltage measured in the solar cell.

2.3 Components of the DSSC

2.3.1 The dye

The dye is the heart of the DSSC: through its photoexcitation, an electron is injected into the conduction band of the metal oxide, and a hole to the electrolyte solution.

In 1993, the N3 dye was the first ruthenium-based dye reported and was for many years the most used related to its high charge separation efficiency and spectral features [15]; however, materials such as ZnO have shown a poor chemical stability at long sensitizing times in N3 and N719 (another Ru-based complex) dye solutions, leading to the formation of Zn^{2+}-dye aggregates on the semiconductor surface, which decrease the ability of the molecule to inject electrons [16] [17] [18][19][20]. In this way, the choice of the dye not only depends on its optical features, but also on the type of semiconductor to be used; hence, a large number of dyes, either organic or organometallic, have been developed over time of more than three decades.

The dyes to be used in these devices must cover some special requirements:

1) A wide absorption spectrum in the visible and even in the near infrared part of the electromagnetic solar radiation spectrum.

2) An excited state lifetime large enough to avoid its relaxation before charge injection into the semiconductor.

3) The position of the excited state level has to provide enough driving force to promote the electron transfer to the accepting states in the semiconductor.

4) The redox potential of the ground state has to be more positive than the redox potential of the electron donor in the electrolyte solution in order to be regenerated after charge injection.

5) The dye has to be firmly grafted on the semiconductor surface through one or more functional groups, which also provide a means for the electron injection.

Conversion efficiencies as high as 13% under standard irradiation conditions have been reported in recent years, achieved through a better understanding on the design of these molecular absorbers [21].

2.3.2 The mesoporous nanostructured semiconducting film

The nanostructured, semiconducting film is fabricated from crystalline nanoparticles commonly synthesized by methods such as sol-gel, pyrolysis, and of our particular interest by electrochemical routes. For applications in DSSCs, the film has to have a large surface area as well as a good electrical contact with the substrate; in this way, a large amount of sensitizing dye molecules will be able to adsorb at the surface, injecting electrons that will be rapidly transported. Different to other photovoltaic devices, in DSSCs the transport of the electrons in the mesoporous network is a diffusion-limited process driven by an electron concentration profile along the film [22]. The dependence of this diffusive transport process on the light intensity has been successfully explained with the multiple trapping model, which assumes an exponential distribution of localized states below the conduction band edge; thus, an increase in the diffusion coefficient is expected as the quasi-Fermi level in the

semiconductor moves to higher energy (with the light intensity) due to an increase of the density of free electrons in the conduction band that trap and de-trap more easily [23].

Related to the metal oxide, almost all the research has been focused on TiO_2 due to the high efficiencies usually obtained; however, in recent years, a lot of attention has been put on a variety of metal oxides such as SnO_2, Nb_2O_5, Ta_2O_5, WO_3, Fe_2O_3, ZrO_2, CeO_2 and ZnO among others. It is due to its easy fabrication and superior electronic mobility that ZnO has been considered as one of the most promising candidates to replace TiO_2 as the electron transporting material in high efficiency DSSCs, which explains the main motivation of this work.

2.3.2.1 Electrodeposition

Electrodeposition or electroplating is an electrochemical technique used for the growth of metals and metal oxides on conducting substrates. The material deposited is obtained through the reduction or oxidation of electroactive species in the electrolytic bath when an electric current flows between the working and the counter electrode. Figure 3 shows a schematic diagram of a three-electrode electrochemical cell, which is the configuration chosen in this work. The properties exhibited by the plated layers may depend on a variety of factors, such as the pH, deposition current or voltage, agitation, time, composition of the electrolytic bath, additives, geometry of the substrate, among others. The use of additives in the deposition bath has been widely studied for the effects that they can generate not only on the kinetics of the reactions that take place at the electrode, but also for their impact on the uniformity, morphology and particle size of the materials deposited.

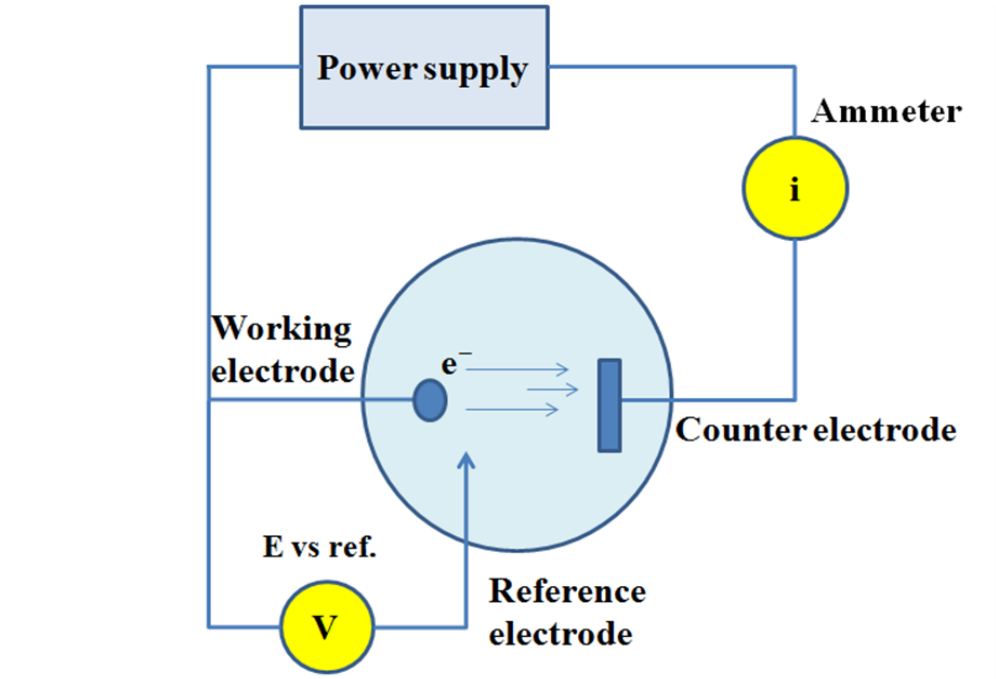

Figure 3.- Diagram of a three electrode electrochemical cell.

Interesting ZnO architectures have been generated through electrodeposition from different zinc precursors such as $Zn(NO_3)_2$ and $ZnCl_2$; it is the good quality of the films obtained and the low temperature working conditions required that have made it an attractive and widely used synthesis method for applications in DSSC [5].

2.3.3 The electrolyte solution

In order to regenerate the oxidized dye molecule (D^+) to its ground state (D^o) an electrolyte solution is incorporated into the cell, filling the space between the sensitized film (or working electrode) and the counter electrode. Usually, the electrolyte solution is based on a low viscosity non-aqueous solvent, being the acetonitrile the most used, in which additives and a redox couple (as charge carrier species) have been dissolved. Traditionally, the I^-/I_3^- redox couple has been the common choice in the construction of DSSCs; its success relies on the slow recombination kinetics observed with the electrons at the semiconductor surface and fast dye regeneration; however, the large overpotential needed for this process is its main disadvantage, limiting the voltage and conversion efficiency of the cells [24].

The use of alternative redox couples based on pseudohalogens [25], cobalt (II/III) complexes [11], copper (I/II) complexes [26], and organic radicals (such as the TEMPO/$TEMPO^+$) [27] among others, has been studied as a route to increase the cell photovoltage, to reduce the loss related to the overpotential as in the case of the I^-/I_3^- redox couple. Encouraging results have been obtained with this approach.

In the preparation of an electrolyte solution, some characteristics have to be taken into account:

1) The solvent must be stable in the potential window where the cell operates, and not be reactive with the dye-metal oxide bond.

2) Be chemically inert with all the components used in the cell.

3) The electrolytic salts and additives must have good solubility in the solvent, ensuring a high concentration of charge carriers in the solution.

4) Negligible light absorption.

5) The redox couple has to show a high diffusion coefficient and fast electron transfer kinetics to the oxidized dye molecule.

2.3.4 The counter electrode

The counter electrode is usually prepared by deposition of a thin Pt-layer onto the conducting glass substrate, which catalyzes the reduction of the oxidized electron donor in the electrolyte solution after dye regeneration; this is I_3^- in the I^-/I_3^--based electrolyte solutions. However, with the use of alternative redox couples new materials have been investigated to overcome the slow reaction kinetics that some of them show on the classical Pt-catalyzed counter electrodes, such as carbon materials and conducting polymers, showing not only good performance in the solar devices, but also lower costs [14].

3. Characterization techniques

3.1 Current- potential curves

Current-potential curves are graphical representations of the operation of the solar device, which summarize the relationship between the current and voltage at a defined temperature and light intensity (fig. 4). The measuring of these curves, the solar cell characterization, is usually performed at 1 sun of illumination (100 mW cm^{-2}, AM1.5G), by changing the external load from zero (short circuit condition) to infinite (open circuit condition) resistance.

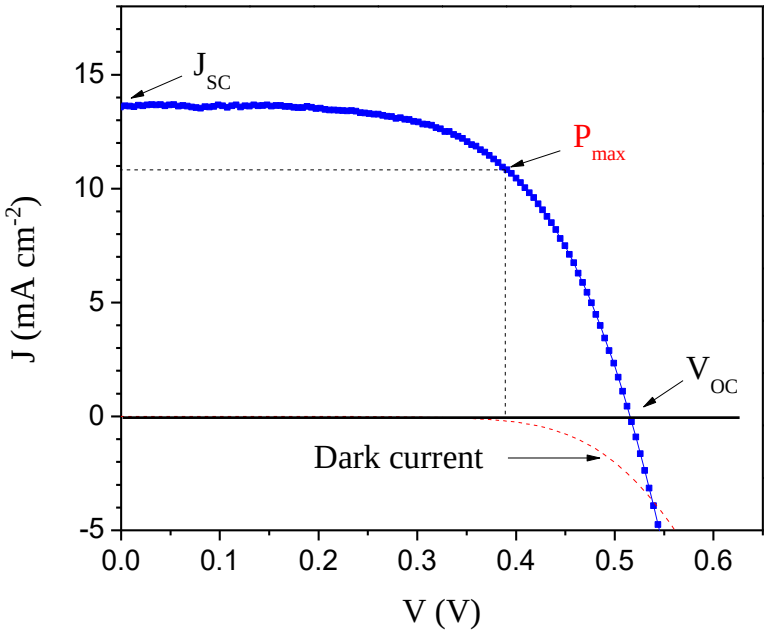

Figure 4.- Current-potential curve for a D149 sensitized solar cell (elaborated in this work) prepared with an I^-/I_3^- electrolyte solution.

The maximum power point (P_{max}), corresponds to the point in where the product of the current and voltage is maximum; with P_{max} and the power of the incident light (P_{in}= 1000 W m^{-2}) the efficiency of the solar cell can be calculated (eq. 3.1).

$$\eta = P_{max} / P_{in} = (J_{SC} * V_{OC} * FF) / P_{in} \qquad (3.1)$$

Where FF is the fill factor, which relates the maximum power point with the short circuit current density (J_{SC}) and the open circuit voltage (V_{OC}) (eq. 3.2):

$$FF = (J_{max} * V_{max}) / (J_{SC} * V_{OC}) = P_{max} / (J_{SC} * V_{OC}) \qquad (3.2)$$

The current-voltage curves can be measured in dark conditions, which makes it possible to extract information about the reaction rate of the electrons injected in the metal oxide conduction band with the electron acceptors in the electrolyte solution.

3.2 Incident photon to current conversion efficiency (IPCE)

The incident photon to current conversion efficiency, also called the external quantum efficiency (EQE), is the ratio between the number of the charge carriers collected by the solar cell and the number of photons of a given wavelength (λ) incident on the solar cell surface (eq 3.3).

$$IPCE = J_{SC} / q\Phi(\lambda) = 1240 * J_{SC}(\lambda)[A\ cm^{-2}] / \lambda\ [nm] * P_{in}(\lambda)[W\ cm^{-2}] \qquad (3.3)$$

where q is the elemental charge of the electron (q = 1.6 x 10^{-19} C).

In the ideal case in which all the incident photons of determined energy are absorbed and the resulting charge carriers are completely collected, the IPCE at that energy (wavelength) is 100%. For photons with energy below the absorption onset or band gap of the material, the IPCE is zero (fig. 5).

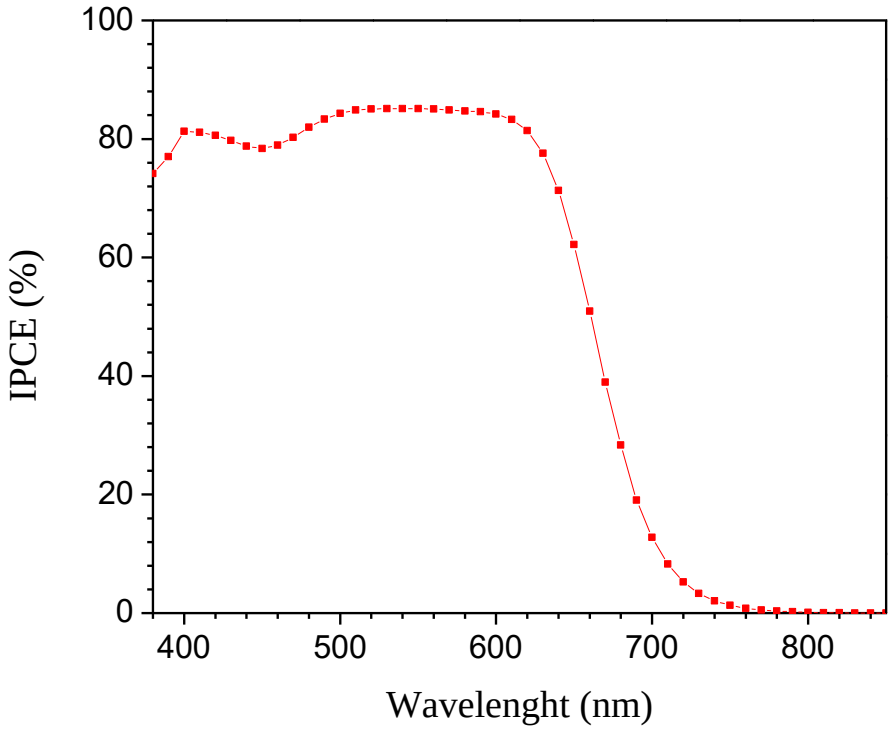

Figure 5. IPCE spectra for a D149 sensitized solar cell (elaborated in this work), prepared with an I^- /I_3^- electrolyte solution.

The IPCE can be related with the product of the efficiencies of three physical processes (eq. 3.4): The light harvesting efficiency (Φ_{lh}), the injection efficiency (Φ_{inj}), and the charge collection efficiency (Φ_{coll}).

$$IPCE = \Phi_{lh} * \Phi_{inj} * \Phi_{coll} \qquad (3.4)$$

The Φ_{lh} is determined by the optical features of the dye, as well as the number of dye molecules adsorbed to the film, and describes the fraction of light absorbed of a specific wavelength; the Φ_{inj} describes the efficiency of the charge separation process between the excited state of the dye and the semiconductor, while Φ_{coll} indicates the probability of collection of the electrons injected in the semiconductor due to the balance between transport and recombination.

3.3 Charge extraction

The charge extraction method has shown to be a useful technique to relate the charge accumulated in the semiconductor with the J_{SC} or V_{OC} in the cell. This information helps to predict shifts in the conduction band edge, when it is performed under open circuit conditions, or to present the electron lifetimes measured as function of the position of the quasi-Fermi level with respect to the conduction band edge; this latter method makes it possible to compare properly the recombination kinetics observed when working with redox couples with different redox potentials, for example.

Under open circuit conditions, the charge extraction is performed by illuminating the cell until a steady state voltage is obtained: then the illumination is switched off and at the same

time the cell is switched to short circuit conditions. Finally, integration of the resulting current transient allows calculating the charge density extracted (fig. 6). In order to analyze properly the information obtained three sources of error must be taken into account [28]:

1) Not all the photogenerated carriers are extracted at short circuit because the time required to collect electrons in deep trap states usually is too long.

2) The electrons can react with the electron acceptor in the electrolyte solution before they reach the substrate.

3) The charging of the fluorine-doped tin oxide (FTO) coated substrate when the cell is switched from open to short circuit.

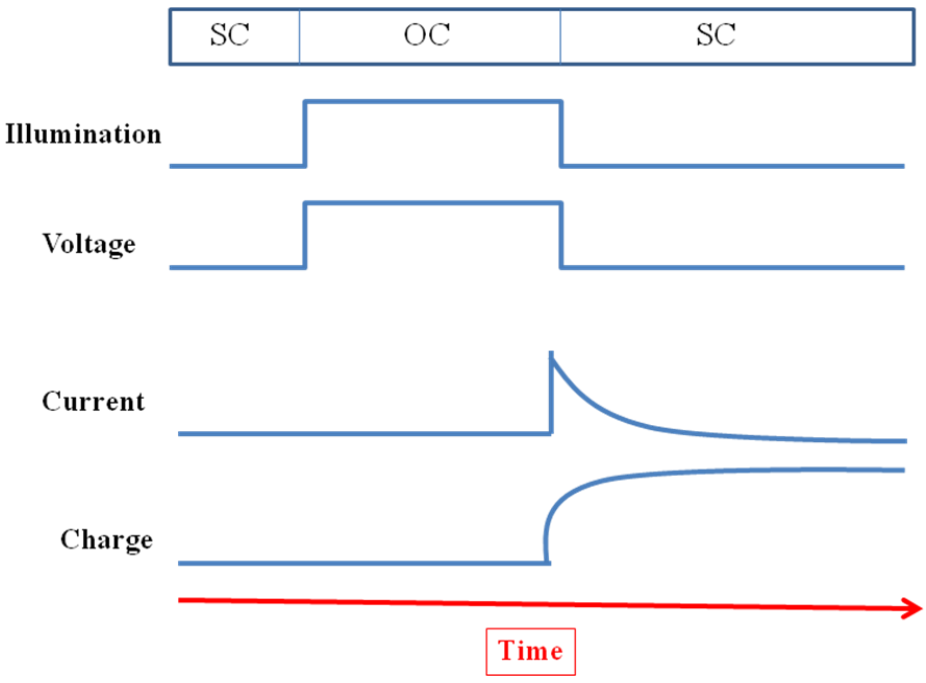

Figure 6.- Open circuit (OC)/ short circuit (SC) sequences showing the relationship between the illumination and the measurement of potential, current and charge extracted.

3.4 Stepped light-induced transient measurements of photocurrent and voltage (SLIM-PCV)

The electron diffusion coefficients (D_n) and electron lifetimes (τ_n) of dye-sensitized solar cells can be estimated through the measurement of photocurrent and voltage transients (respectively) induced by small steps in the light intensity [29]. Under short circuit conditions of the DSSC, a decrease of the light intensity induces a current transient (fig. 7a) characterized for an initial and a final state of the J_{SC}, and the time to reach the final state depends on the electron diffusion coefficient. For the case where the transients can be fitted with an exponential function, $\exp(-t/\tau_C)$, D_n (eq. 3.7) can be calculated through the approximation used by Kopidakis (eq. 3.5) [30] and the following relationships:

$$D= (L/2)^2 / t_H \qquad (3.5)$$

$$t_H= 0.693\ \tau_C \qquad (3.6)$$

$$D= L^2/ (2.77\ \tau_C) \qquad (3.7)$$

Where t_H is the time to extract half of the excess electrons and L is the thickness of the electrode.

The electron lifetime (τ_n) at open circuit can be measured from the photovoltage response of the cell after perturbation of the light intensity (fig. 7b). The solution of the rate equation of the electron density, n(x,t), by setting the final light intensity as zero, gives an exponential function:

$$dn(t)/dt= G(t) - n(t)/\tau_n \qquad (3.8)$$

$$n(t)= \Delta n \exp(-t/\tau_n) \qquad (3.9)$$

Where G(t) is the electron generation rate, and Δn is the difference of the electron densities under the initial and the final illumination conditions. Equation 3.9 can be used to fit the voltage transients, since ΔV_{OC} is proportional to Δn when the change in the electron density is very small. Note that a first-order recombination rate in electron density is assumed.

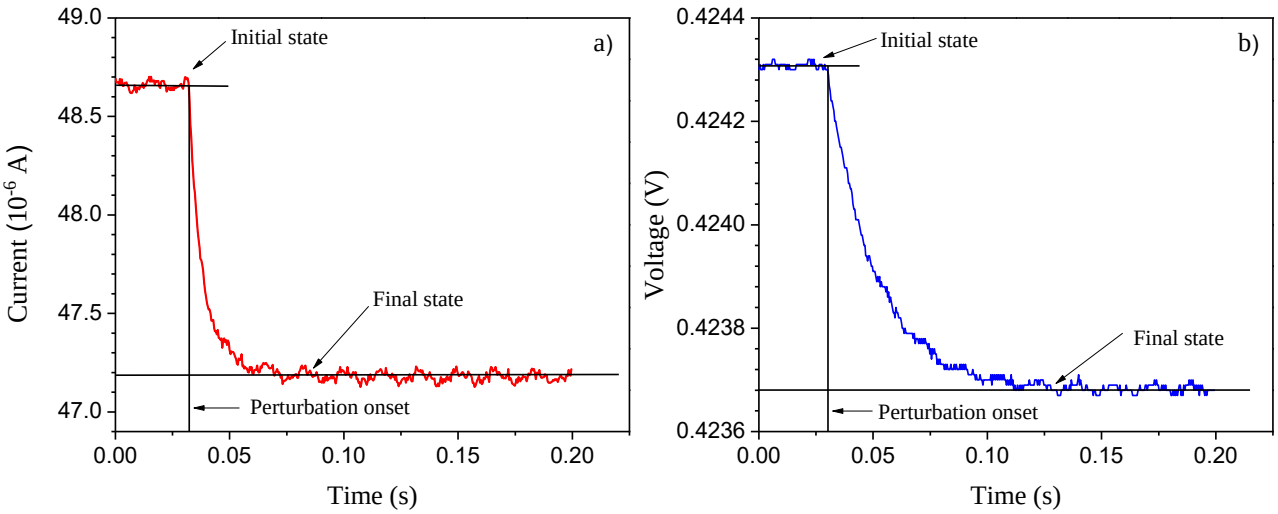

Figure 7.- Typical: a) current and b) photovoltage response of a ZnO based solar cell, elaborated with the D149 dye and an I^-/I_3^- electrolyte solution after small step down of the light intensity. In both graphs, the initial state was reached at the same illumination intensity.

3.5 Surface photovoltage spectroscopy (SPS)

Surface photovoltage (SPV) spectroscopy is a contactless technique that probes surface potential changes of materials upon excitation with light (fig. 8). It is assumed that a change in the surface work function is equal to the SPV (in absolute terms). One of the oldest techniques for determining relative changes in work functions is measuring the work function difference between two materials forming the two sides of a parallel plate capacitor. Upon short-circuiting the back contacts of the substrates, charge must flow to equilibrate the differences in Fermi levels, this charge transfer results in an electric field in the gap between the two plates and a drop in the local vacuum level across this gap. The corresponding potential drop is usually known as the contact potential difference (CPD) [31].

The Kelvin probe arrangement has been extensively applied to the measurement of illumination induced changes in work function; this is achieved by ohmically contacting the backside of the working sample to an oscillating metallic reference electrode. Since the work function of the metallic electrode does not change under illumination, the following relation is found:

$$-e\Delta SPV = \Delta W_S = e\Delta CPD \qquad (3.10)$$

For a n-type material, a negative ΔCPD indicates the movement of electrons toward the contact, and the holes to the material's surface.

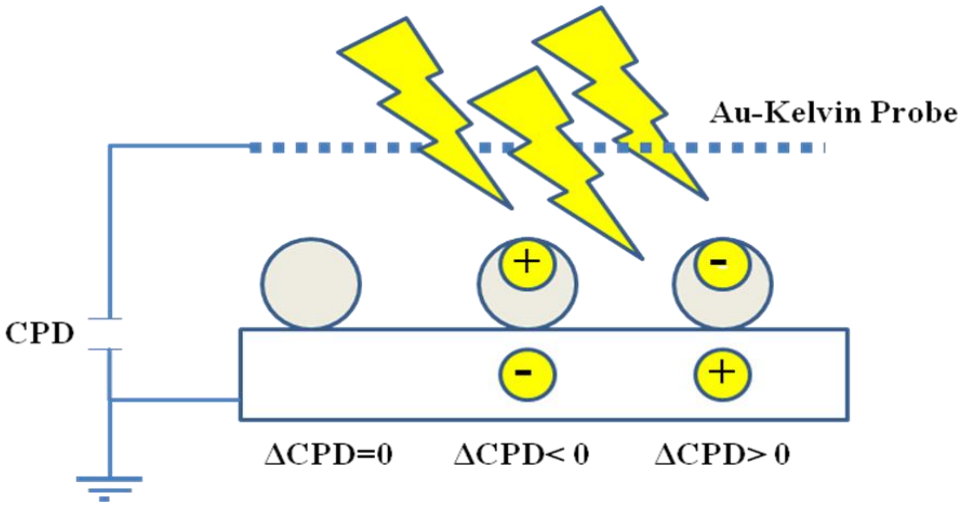

Figure 8.- Schematic description of the SPV phenomena

The sensitivity of SPS is much higher than that of photoelectrochemistry, thus allowing the detection of majority carrier type, mid-gap states, defects, and electrochemical reactions at interface. Historically, SPS has been applied to the characterization of bulk semiconductors and surfaces, but in recent years, this method has gained popularity for the characterization of nanoscale photocatalyst, organic polymers, and (as in the case of this work) for determining the factors that lead to the interfacial charge separation in photovoltaic devices [32–35] .

3.6 Cyclic voltammetry (CV)

Cyclic voltammetry is an electroanalytical technique, in where an electrochemical spectrum is obtained to present the current developed in the electrochemical cell as a function of the triangular potential wave applied, which is a cyclic voltammogram (fig. 9).

For a fast redox system:

$$Ox + ne^- \leftrightarrow Red \qquad (3.11)$$

The polarization of the working electrode to potentials more negative than the formal redox potential (E*) of the couple leads to the flow of negative charges from the electrode to the solution by means of an electrochemical reaction, favoring the reduction of the oxidized species near the electrode surface. In a similar way, by lowering the energy of the electrons to impose a more positive potential than E*, oxidation of the reduced species produced is favored. The reduction or oxidation of electrochemical species in the working solution are observed as a cathodic or an anodic current in the voltammogram, respectively, which show a maximum value (Ip^c and Ip^a respectively), indicating that at this point (Ep^c and Ep^a) the reactions are in a diffusion-controlled regime.

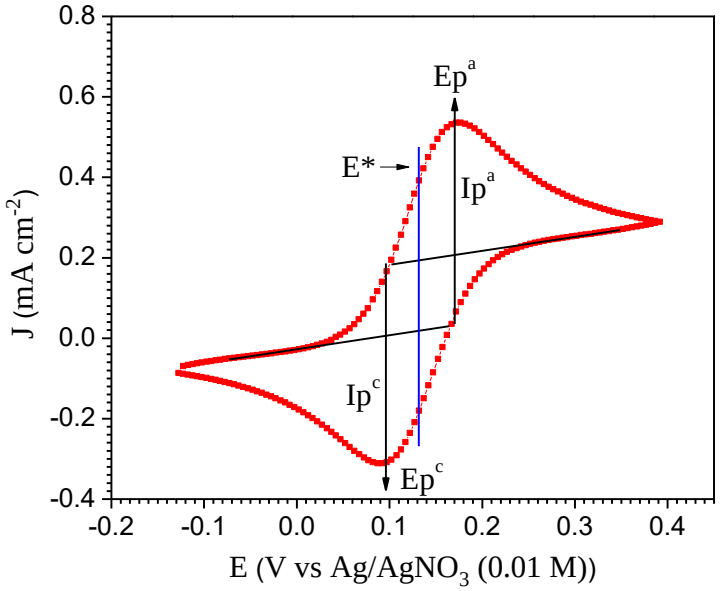

Figure 9.- Cyclic voltammogram obtained in this work for a solution 2 mM ferrocene, 0.1 $TBAPF_6$ in acetonitrile at a scan rate of 0.05 V s^{-1} on Pt, which was used to calibrate a $Ag/AgNO_3$ (0.01 M) reference electrode.

The magnitude of the currents mentioned above may depend on different parameters such as the concentration of the electroactive species in the solution, the diffusion coefficient and the scan rate, as described by the Randles-Sevcik equation:

$$Ip = (2.69x10^5)\, n^{3/2}\, A\, D^{1/2}\, C_o\, \nu^{1/2} \qquad (3.12)$$

Where:

Ip= peak current density (A cm^{-2})

D= diffusion coefficient (cm^2 s^{-1})

ν= scan rate (V s^{-1})

C_o= concentration of the electroactive specie (mol cm^{-3})

Information about the reversibility of the redox system can be extracted from the voltammogram by evaluating the following parameters:

$$\Delta E_p = Ep^a - Ep^c = 59 \text{ mV/n} \quad (3.13)$$

$$|Ip^a/Ip^c| = 1 \quad (3.14)$$

$$|Ep - E_{1/2}| = 28 \text{ mV/n} \quad (3.15)$$

$$Ip \; \alpha \; \nu^{1/2} \quad (3.16)$$

Ep independent of ν (3.17)

3.7 Uv-vis spectrophotometry

The spectral features of any substance or material that absorbs light can be determined by the use of Uv-vis spectrophotometry. The absorbance, A(λ), of a sample at a specific wavelength can be calculated from the transmittance, the fraction of light that has passed through the sample.

$$A(\lambda) = - \text{Log}_{10} T(\lambda) = -\text{Log}_{10} (I/I_o) \quad (3.18)$$

Where I_o is the intensity of the incident light and I the intensity of the light detected.

The absorbance can be related with the concentration of the absorbing substance through the Lambert-Beer law (eq. 3.19); thus, if the concentration (C) and the optical path length (L) are known, the molar extinction coefficient can be calculated (ε).

$$A(\lambda)= \varepsilon(L\ mol^{-1}\ cm^{-1})\ C(M)\ L(cm) \qquad (3.19)$$

3.8 X-ray diffraction (XRD) and scanning electron microscopy (SEM)

X-ray diffraction is a non-destructive analytical technique that allows obtaining insight about the chemical composition and crystal structure of crystalline material, on the observation that every crystalline substance generates an unrepeatable pattern, similar to a fingerprint. In this work a Siemens D-5000 diffractometer with a Cu-Kα radiation at 34 kV and 25 mA was employed to analyze and corroborate the crystallographic features of the materials deposited as thin films; the diffraction patterns were collected from 10º to 70º (2θ) with a 0.02º step size and 2 s integration time.

The morphology obtained in the materials synthesized was observed through scanning electron microscopy images. In this technique, a beam of electrons is focused on the sample with the use of electromagnets, and the signals generated for the interaction of the accelerated electrons and the electrons in the atoms that conform the material are analyzed with specific sensor to form an image. SEM images were taken with a JEOL JSM 7600 F setup, operated at an accelerating voltage of 15 kV, and using the in-lens (SEI) secondary electron detector.

4. Aim of this work

The main motivation of this work has been to explore the use and combination of novel dyes and redox couples in order to generate more efficient ZnO-based DSSCs, material of our choice due to its better electrical properties (at least, as observed in bulk ZnO) when comparing with the classically used TiO_2 semiconductor. This may be accomplished through an improvement of the J_{sc}, V_{oc} and FF developed in the solar devices by increasing the amount of light absorbed, diminish the electron losses by recombination pathways and to increase the stability of the semiconductor during the sensitization process, strategies studied in the following chapters.

In chapter 5 we present a study on the deposition of porous ZnO films from $ZnCl_2$ and $Zn(NO_3)_2$ solutions by electrochemical methods. Our interest in these synthesis methods is not only because of the morphologies and composition of the films that can be obtained as a function of the experimental parameters employed, but also for the high deposition speeds and low working temperatures; these characteristics make electrodeposition an attractive technique for large-scale production of DSSCs.

Poor chemical stability of ZnO, when comparing with TiO_2, during the sensitization process of the films before assembly of the cell has been reported as an important efficiency-limiting factor in ZnO-based DSSC, related with the acidity of the dyes and the immersion time of the films in the sensitizing solution. In chapter 6 we selected the organic dye OD-8, which only possesses one carboxylic group (as a part of the cyanoacrylic acid moiety) as anchoring group, and high light absorption in the visible as a feasible option to overcome the stability issue mentioned above; in this way, J_{sc} may be increased by increasing the amount of dye

adsorbed at the surface with sensitization time. On the other hand, if the coverage of the particle surface is good enough, an increase of the V_{oc} can be achieved with the use of fast redox mediators such as the Co(II/III) coordination complex, which not only show more positive redox potential than that the I^-/I_3^- redox couple, but also exhibit faster regeneration of the oxidized dye molecule at lower driving forces. The effect of the CDCA (chenodeoxycholic acid) co-adsorbent on the surface passivation of the particles is also investigated in this section.

In a similar way as in chapter 6, in chapter 7 we evaluate the performance of a non-commercial series of monoanhydride-perylene based dyes, in which an anhydride ring acts as precursor of the anchoring groups that attach the molecule to the particle surface. The absence of releasable protons (H^+) in the dye structure may make these sensitizers chemically suitable candidates to interact with ZnO. This may lead to an increase of the cell efficiency due to the broad light absorption range and high molar extinction coefficients that they present.

5. Electrochemical deposition of nanostructured ZnO electrodes applied to DSSCs

Mechanisms to electrodeposit ZnO from aqueous solution can broadly be divided into two groups: (i) reduction of a zinc salt solution to metallic zinc and simultaneous and subsequent oxidation of the metallic zinc by dissolved oxygen to form ZnO, and (ii) reduction of a different component of the zinc salt solution, such as nitrate, to form a large concentration of surface hydroxide resulting in deposition of $Zn(OH)_2$ and subsequent condensation to ZnO or the formation of zinc hydroxychloride compounds, depending on the composition of the bath.

In this chapter, we present a study on the electrochemical reactions that lead to the formation of ZnO films from $ZnCl_2$ and $Zn(NO_3)_2$ solutions, due to the interesting properties that the materials obtained by electrochemical routes can present as a function of the experimental parameters, such as concentration and composition of the electrolytic baths, pH of the solution, temperature, deposition current or potential, either pulsed or steady-state, etc.; to finally be applied to the construction of DSSCs.

5.1 Experimental procedure

The electrochemical spectrum of the working solutions was obtained by performing cyclic voltammetry with a Gamry potentiostat/galvanostat/ZRA 3000 employing a classic three-electrode system with a Ag/AgCl (3 M KCl) as reference electrode, a Pt counter electrode and a FTO (TEC 8) working electrode previously cleaned in an ultrasonic bath for 20 minutes

in ethanol, and sintered at 450º for 1 h. Porous films of ZnO were obtained through the use of a galvanostatic electrodeposition method using a Gamry potentiostat/ galvanostat/ZRA 3000 with Ag/AgCl (3 M KCl) as a reference electrode, Pt as counter and SnO_2:F-coated glass substrate (FTO, TEC 8 Ω sq^{-1}, Pilkington) as a working electrode. A 0.5 cm^2 area was masked with polyester tape (Cole-Parmer), and activated with 2 M H_2SO_4 followed by rinsing with deionized water. The electrolyte was prepared with 0.01 M $ZnCl_2$, 0.1 M KCl and 0.10 mM of the water-soluble PVP40 polymer (polyvinylpyrrolidone; M_W= 40,000 g mol^{-1}) in order to better control the morphology and porosity of the ZnO films. The solution was bubbled with O_2 for 20 minutes before use. For the electrodeposition process a current density of -0.5 mA cm^{-2} was applied for 8427 seconds. All the films were sintered at 450 °C for 1 h after electrodeposition. Simonkolleite films where deposited from a 0.1 M $Zn(NO_3)_2 \bullet 6H_2O$, 0.1 M KCl aqueous solution at 70 ºC and pH= 6.0, following the same steps as for the ZnO films. The deposition conditions and thermal treatments applied to these films are explicitly explained in the corresponding sections.

The dye used in this section was the (Z)-2-Cyano-3-(5-(9,9-dihexyl-7-(dihexylamino)-9H-fluoren-2-yl)thiophen-2-yl)acrylic acid (OD-8; from Eversolar); 0.5 mM OD-8 and 0.5 mM CDCA (as coabsorbent) solutions were prepared to dissolve the desired amounts of these reagents in a mixture of acetonitrile/t-butyl alcohol (1:1 v/v). ZnO films were heated at 90 °C for 20 min and immediately soaked in the dye solution (described above) in order to achieve sensitization. After sensitization, the films were removed from the dye solution and carefully washed with the same mixture of acetonitrile/t-butyl alcohol.

Dye sensitized solar cells (DSSCs) were prepared with the sensitized ZnO films described previously and a FTO counter electrode with a thin coating of Pt, prepared by spreading a

drop of Platisol (Solaronix) on the conductive side of the electrode and subsequent heating at 450 °C for 5 min. The photoanode and counter electrode were sealed in a sandwich configuration using a Surlyn (60 μm) separator by heating at 210 °C for 2.5 min. Finally, the electrolyte solution was introduced inside the cell through a pair of holes previously perforated in the counter electrode, which were subsequently sealed with Surlyn and microscope cover glass pressed under heating. Photovoltaic characterization was performed using a set-up consisting of a 450 W ozone-free Xe-lamp (Newport Corporation) with a water filter, calibrated to an irradiance of 100 mW cm^{-2} on the surface of the solar cell using an Air Mass 1.5 Global (AM 1.5G) optical filter (Newport Corporation). The intensity was calibrated using a certified 4 cm^2 monocrystalline silicon reference cell with incorporated KG-5 filter. Current–voltage curves (I–V) were recorded with an Autolab PGSTAT302N/FRA2 set-up (Metrohm Autolab).

5.2 Electrodeposition of ZnO films from aqueous $ZnCl_2$ solutions.

Figure 10 shows a cyclic voltammogram for a FTO (fluorine-doped tin oxide) working electrode and a solution containing $ZnCl_2$ + KCl at neutral pH, which was saturated with either N_2 or O_2 in order to determine the reaction mechanism leading to the formation of ZnO. Both N_2 and O_2 bubbled solutions showed a cathodic current maximum at around -1.16 and -1.21 V, respectively, related to the reduction of Zn^{2+} and nucleation and growth of mainly metallic Zn. Lincot and co-workers have shown in a very detailed study that in this specific electrolyte solution and using FTO as a working electrode, O_2 reduction does not

take place in this potential range; they show that the presence of Zn^{2+} ions in the electrolyte solution can suppress the oxygen reduction reaction due to the adsorption of zinc containing species at the surface of the FTO substrate [36]. A similar trend in the O_2 reduction reaction in $ZnCl_2$ solutions was found by Tena-Zaera et al., related with the concentration of the KCl supporting electrolyte [37]. At more negative potentials (-1.5 V vs Ag/AgCl) water reduction becomes the main electrochemical reaction. When reversing the direction of the potential sweep, an anodic current maximum is observed in both systems at -0.94 and -0.98 V, respectively, which corresponds to the electrochemical oxidation of the metallic zinc previously deposited. The anodic peak is significantly smaller for the solution saturated with oxygen, and this observation can be understood in the framework of mechanism (i) widely studied by Lincot´s group, and depicted for the ***overall*** reaction in equation 5.1 [36,38].

$$Zn^{2+} + 0.5\ O_2 + 2e^- \rightarrow ZnO \qquad (5.1)$$

Even during the cathodic sweep, electrodeposited metallic Zn reacts with the oxygen dissolved in the solution forming ZnO. Hence, upon reversing the sweep towards positive potentials, only traces of metallic zinc are present, resulting in a small electrochemical oxidation peak. In the solution saturated with nitrogen, most metallic zinc remains and is electrochemically oxidized upon sweeping the potential towards positive potentials resulting in a large oxidation peak.

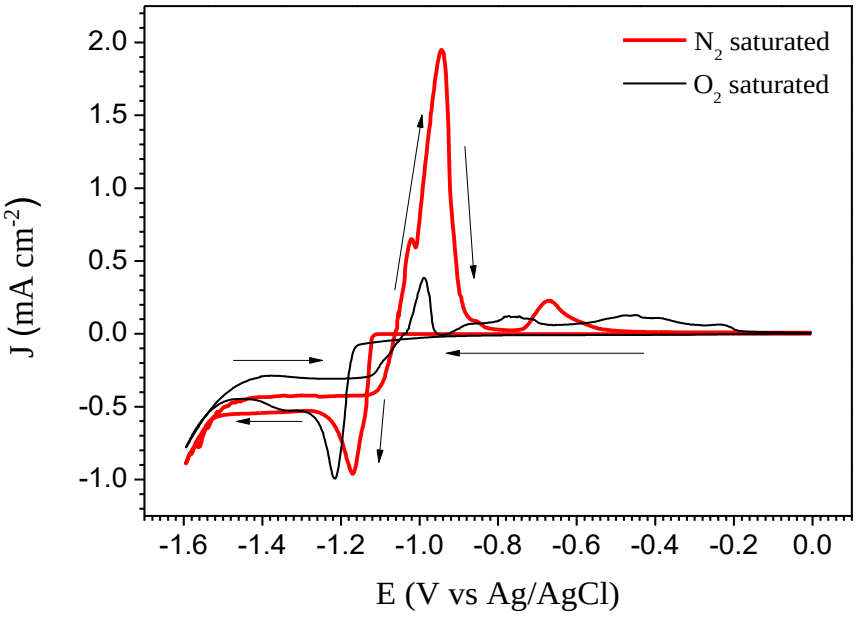

Figure 10.- Current-potential curves obtained in a solution of 0.01 M $ZnCl_2$ + 0.10 M KCl using an FTO-TEC8 working electrode after either O_2 or N_2 bubbling for 20 min. All experiments were performed at room temperature (25 °C) and at a scan rate of 2 mV s^{-1}.

Organic additives added to the electrolytic bath not only can change the properties of the material deposited, but also the kinetics of the electron transfer at the electrode/solution interface increasing the deposition overpotential; this effect can be understood in terms of adsorption of the surfactant onto the electrode surface during its polarization. However, current - potential curves in Figure 11 illustrate that the presence of PVP40 polymer does not markedly change the electrochemical behavior of the deposition bath.

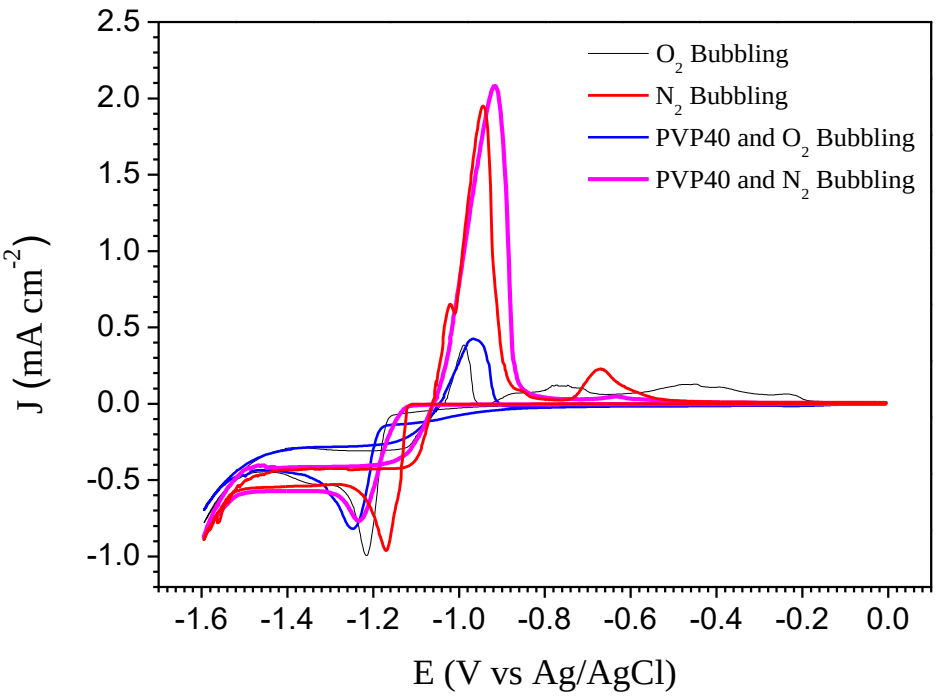

Figure 11.- Current potential curves obtained in a solution of 0.01 M $ZnCl_2$ + 0.10 M KCl using an FTO working electrode after either O_2 or N_2 bubbling for 20 min, and with and without 0.10 mM PVP40. All experiments were performed at room temperature (25 °C) and at a scan rate of 2 mV s^{-1}.

Figure 12 shows X-ray diffraction patterns of the films electrodeposited from O_2-saturated 0.01 M $ZnCl_2$ + 0.10 M KCl with 0.1 mM PVP40 solutions onto FTO, and at a current density of -0.5 mA cm^{-2} for 8427 seconds, before and after sintering at 450 °C. The patterns show that electrodeposition at room temperature results in a crystalline film. Before sintering (Fig. 12a), peaks associated with both metallic zinc and ZnO are observed, as well as reflections related to the FTO substrate; notably, peaks related to $Zn(OH)_2$ are absent, supporting the prevalence of mechanism (i). It should be noted that during the cathodic sweep, water and O_2 may also be reduced, which could lead to an increase in the surface pH, which may affect

the composition of the deposited material [36,37]. After sintering in air (Fig. 12b), metallic Zn has been oxidized to ZnO with the hexagonal crystal structure.

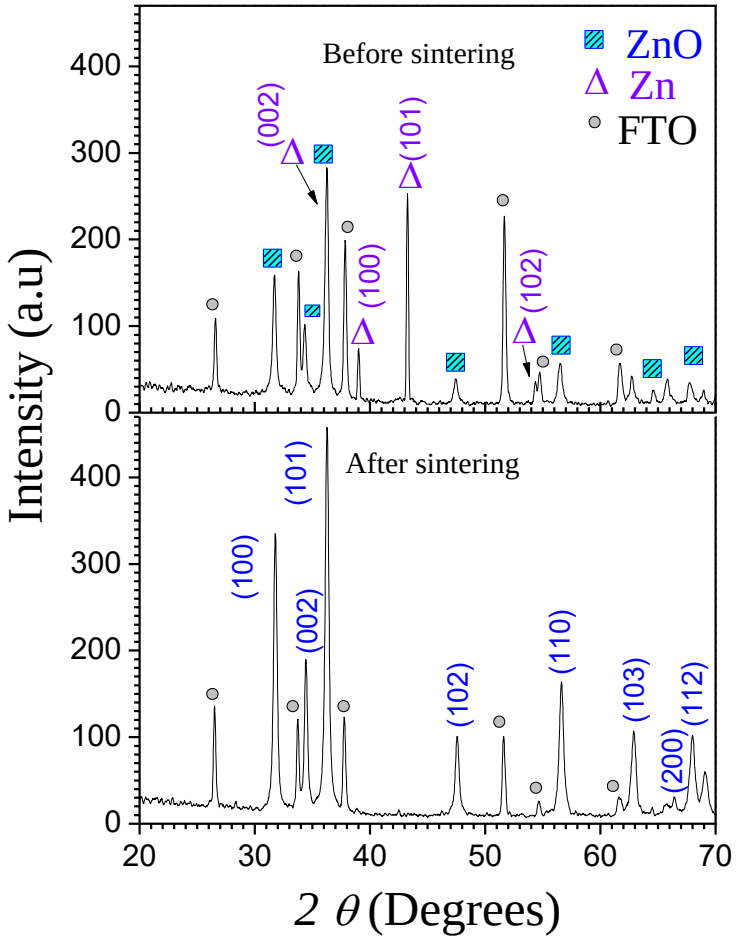

Figure 12.- X-ray diffraction patterns of electrodeposited ZnO films from the O_2-saturated 0.01 M $ZnCl_2$ + 0.10 M KCl with 0.1 mM PVP40 onto FTO, (a) before, and (b) after sintering.

The morphology of the sintered ZnO films is shown in Figure 13. The SEM images illustrate that the film is mainly composed of clusters of rounded particles with sizes between 10-50 nm, however, other structures such as thin needles with lengths of up to 1 μm, as well as non-porous agglomerates of about 1 μm, are also observed. The presence of "rounded" particles

is associated with the presence of PVP40 in the deposition bath: PVP40 adsorbs at a similar rate on the different faces of the growing ZnO particles, thus modulating grain size and morphology [39]. The presence of needles is characteristic of the preferential nucleation of ZnO by the electrodeposition route [37]. For the fabrication of DSSCs, mesoporous and nanostructured ZnO films with an average thickness of 9.23 ± 0.74 μm were obtained through galvanostatic electrodeposition; their performance will be analized in the chapter 6.

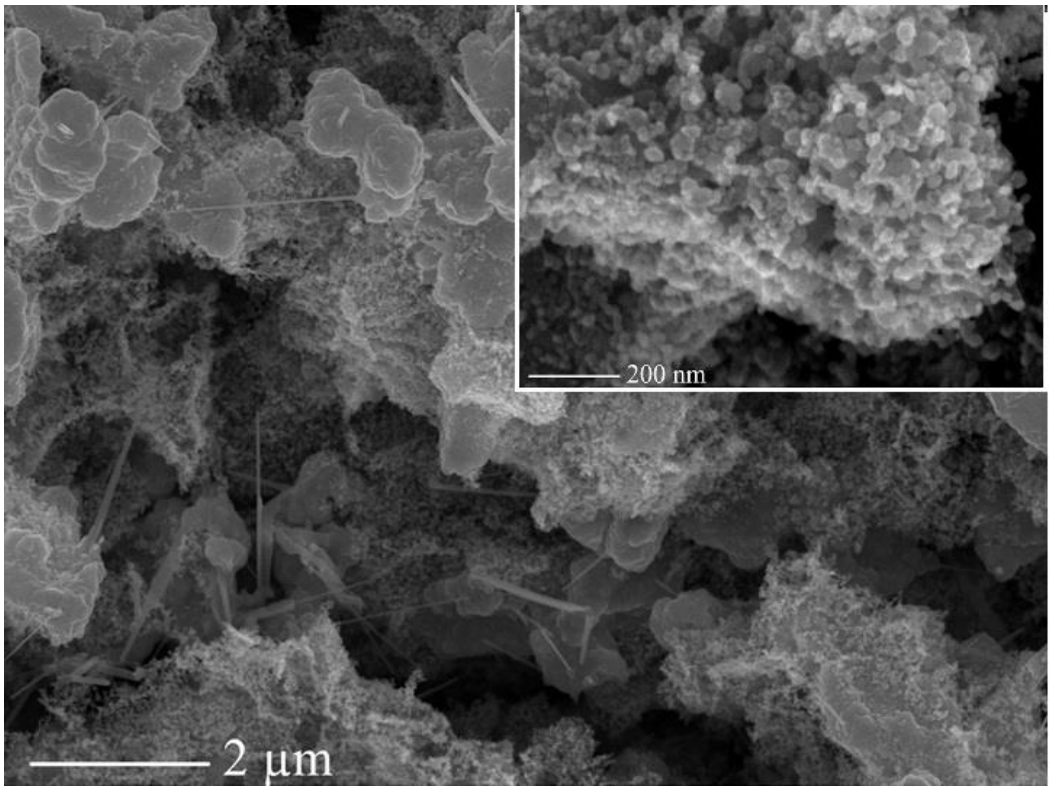

Figure 13.- SEM images of ZnO films sintered at 450 ºC and electrodeposited from O_2-saturated 0.01 M $ZnCl_2$ + 0.10 M KCl with 0.1 mM PVP40 onto FTO.

5.3 Electrodeposition of Simonkolleite as a low temperature synthesis route of crystalline ZnO electrodes

As mentioned in the beginning of this chapter, the second route used to electrodeposit ZnO consists of the electrochemical reduction of a different compound of the zinc salt to increase the concentration of hydroxide ions at the electrode surface, which leads to deposition and condensation of different zinc compounds depending on the bath composition. This work explores a novel method to electrodeposit ZnO films for DSSCs, and the preliminary results presented here indicate the promise of this system, although more work is still needed to elucidate specific mechanisms.

In this section a 0.1 M $Zn(NO_3)_2 \bullet 6H_2O$, 0.1 M KCl aqueous solution at pH= 6.0 and 70 °C was studied and characterized by cyclic voltammetry to identify the electrochemical reactions that take place in a specific potential window.

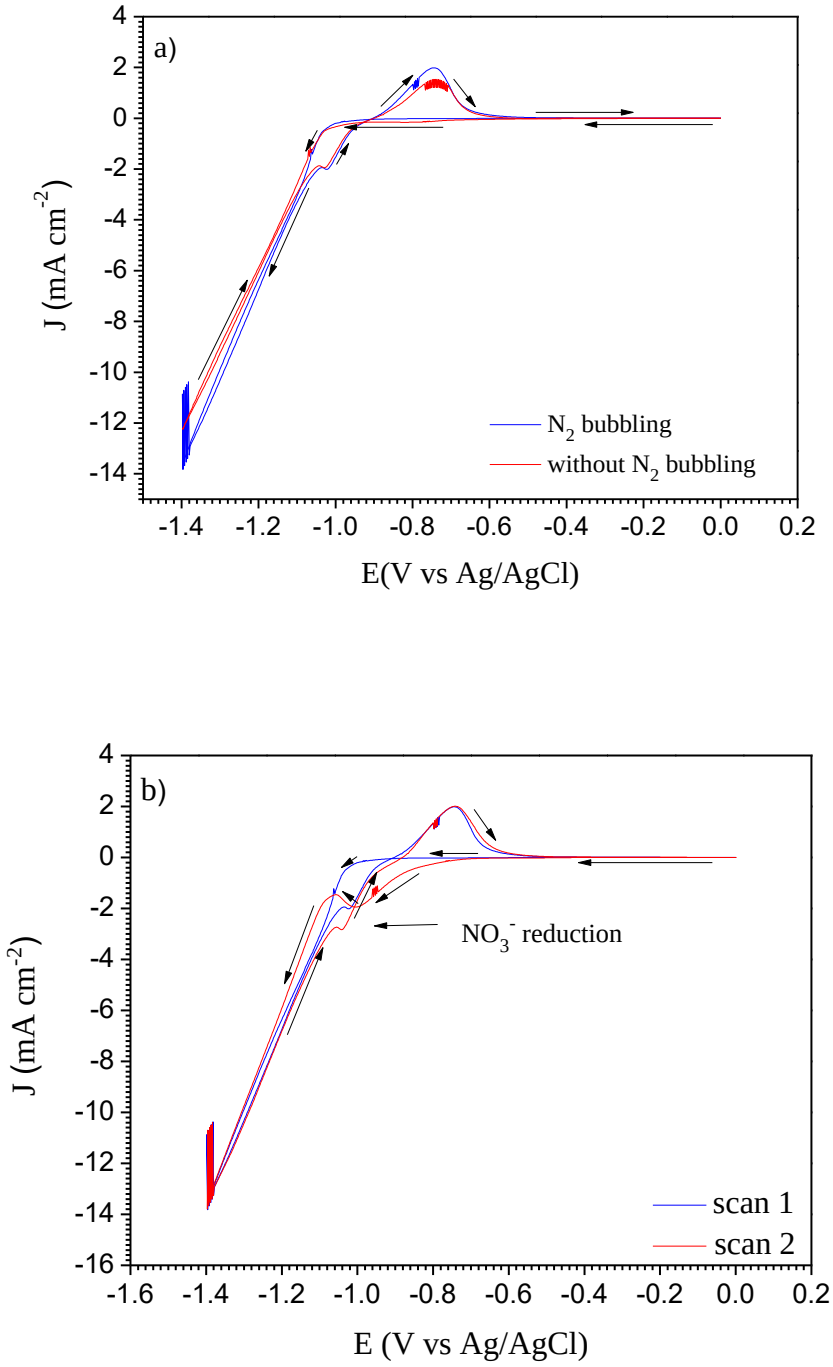

Figure 14.- Cyclic voltammetry for a $Zn(NO_3)_2 \bullet 6H_2O$ and KCl solution: a) with and without N_2 bubbling; b) 1st and 2nd scan. The measurements were performed at 10 mV s^{-1} and 70 °C on a FTO working electrode.

In the electrodeposition of ZnO from nitrate baths, a series of well-known reactions have been proposed by Yoshida et al, widely accepted in the current literature, which lead to the formation of crystalline films on the working electrode [39–45] :

$$NO_3^-(aq) + H_2O(l) + 2e^- \text{-----> } NO_2^-(aq) + 2OH^-(aq) \quad (5.2)$$

$$2H_2O + 2e^- \text{---------> } H_2 + 2OH^- \quad (5.3)$$

$$Zn^{2+}(aq) + 2OH^-(aq) \text{ -------> } Zn(OH)_2(s) \quad (5.4)$$

$$Zn(OH)_2(s) \text{ ----------> } ZnO(s) + H_2O(l) \quad (5.5)$$

Equation 5.2 describes the most important electrochemical reaction, while 5.4 and 5.5 show the condensation of Zn^{2+} as zinc hydroxide and its subsequent dehydratation to finally form the desired oxide.

Figure 14a shows cyclic voltammograms for the mentioned bath with and without previous N_2 bubbling. A significant difference in the electrochemical behavior of the solution was not observed; this is because gas solubility decreases strongly with the increase of temperature: hence, at 70 °C the effect of bubbling with oxygen has much less impact. However, as a step in the standard procedure, all the working solutions were N_2 bubbled before each experiment. An increase in the cathodic current at values more negative than -1.1 V vs Ag/AgCl (in the forward scan) was observed for both baths, related with reduction of water on the FTO surface leading to H_2 formation. When reversing the direction of the potential swept, a peak at -1.02 V vs Ag/AgCl was also observed and attributed to reduction of NO_3^- ions to NO_2^-.

Unfavorable reaction kinetics at FTO seems to be the reason of the non appreciable cathodic current in the forward scan. However, the deposition of zinc-containing compounds during the first sweep due to the condensation of Zn^{2+} ions for an increase in the concentration of OH^- at the electrode surface induced by water reduction and, to a lesser extent, NO_3^- reduction, can change the working electrode surface, and thus the electron transfer rate to the NO_3^- ions. This can make the process visible on the reverse scan and in the following sweeps, as can be seen in Figure 14b, where the current onset shifts from -0.92 V to -0.75 V vs Ag/AgCl between the 1st and the 2nd scan. A detailed study on the electroreduction of Co^{2+} ions in presence of NO_3^- ions in solution has been presented by Barrera et al.; in where the formation of metallic cobalt and reduction of NO_3^- ions was observed simultaneously, as shown by XRD and voltammetric studies [46]. However, different to the mechanism proposed for the last system, reduction of Zn^{2+} in presence of NO_3^- ions seems to be a kinetically not favored electrochemical reaction, as shown by Lizama et al. [44]. In fact, XRD patterns of films electrodeposited from a $Zn(NO_3)_2 \bullet 6H_2O$ and KCl solution did not show evidence of the presence of metallic zinc, as will be shown later. The anodic peak observed at -0.745 V vs Ag/AgCl, which in contrast to the results obtained for the $ZnCl_2$ solution is independent of the presence of oxygen, is not related to oxidation of metallic zinc, but may correspond to oxidation of nitrite or may be a capacitive peak of discharging of the formed zinc-containing compound; however, in order to determine this, more experiments are needed.

The use of KCl as supporting electrolyte to increase the conductivity of working solutions is a common practice in electrochemistry, however in zinc nitrate baths the presence of Cl^- ions favors the formation of Simonkolleite (eq 5.6) instead of $Zn(OH)_2$ [47].

$$5\ Zn^{2+}(aq) + 8\ OH^{-}(aq) + 2\ Cl^{-}(aq) + H_2O(l) \text{ -----> } Zn_5(OH)_8Cl_2 \bullet H_2O(s) \quad (5.6)$$

This way, the reduction of nitrate ions and water (Equations 5.2 and 5.3) increases the concentration of OH^- near the electrode surface, which react with zinc and chloride ions (eq. 5.6) to form a crystalline layer of zinc chloride hydroxide monohydrate as will be shown in the course of this section.

Deposition of uniform films can depend strongly on the electrolysis conditions employed as the electrocrystallization of materials occurs through two competitive processes: the nucleation of new grains and the growth of the existing ones. Nucleation can be favored with high deposition current densities (overpotentials) and low surface diffusion of adsorbed atoms of the existing grains, while grain growth can occur at conditions of low deposition current density (overpotential) and high surface diffusion of the ad-atoms, usually observed in the electrodeposition of metals [48].

As was explained earlier, reduction of nitrate ions in the presence of Zn^{2+} and onto FTO substrates seems to be not only a kinetically slow process, but also an electrode dependent one. It is well known that pulsed plating improves the morphology and properties of this type of deposits related with its positive effects on mass transport, electrode kinetics and the nucleation of growth centers [49]; for this reason, either on-off pulse plating or the use of pulsed plating to aid nucleation and a subsequent current pulse at a steady state current density for growth, were considered as suitable routes to obtain good quality films. The following deposition conditions were studied:

- Z1: 10 pulses: -3.0 mA cm^{-2}, 0.388 s; 0 mA cm^{-2}, 1 s + -150 μA cm^{-2} for 1773.05 s

- Z2: 500, 600, 700 and 1000 pulses: -3.0 mA cm^{-2}, 0.388 s; 0 mA cm^{-2}, 1 s.

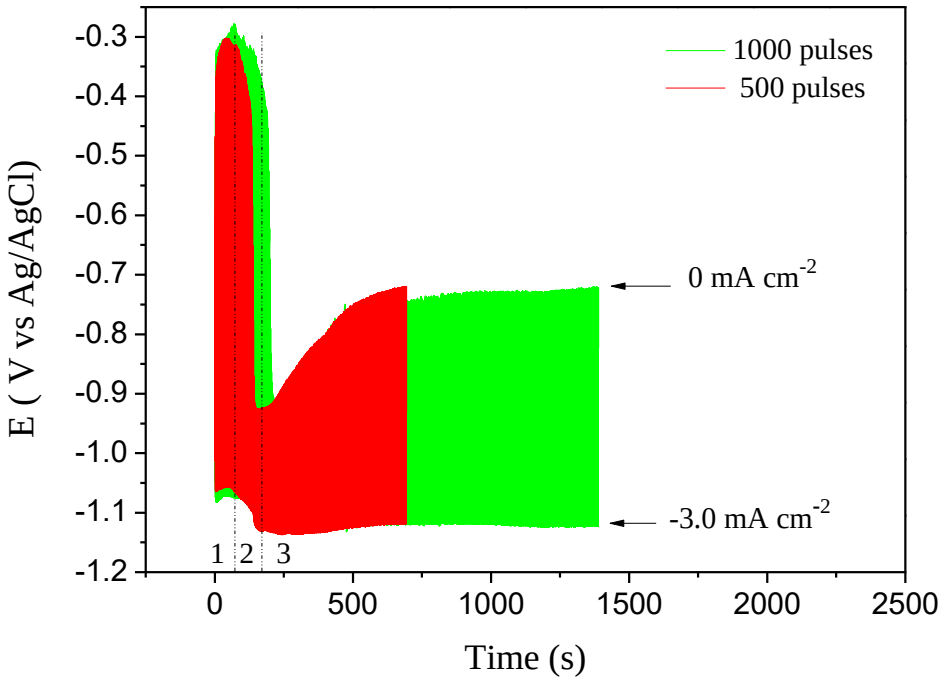

Figure 15.- Voltage transients obtained during pulsed electrodeposition. For simplicity, only the transients for the shortest and the longest procedure are presented; in addition, the regions in where different features between the pulse time (T_{on}) and the relaxation time (T_{off}) were observed are listed.

As shown in Figure A1 (in the appendix) the material deposited with the procedure Z1 exhibited low uniformity, as regions are observed with different thickness along the film. At the beginning, the electrode surface was covered completely with a homogeneous film of porous simonkolleite favored by the high charge density applied in the on-off pulsed part of Z1; however, in the second part of the procedure, the preferential growth of some areas of

the film led to the formation of large simonkolleite crystals (≈ 10 μm). Due to the unsuitable characteristics (for application in solar cell devices) of the films electrodeposited with procedure Z1, the other deposition conditions were studied in more detail.

Figure 15 shows the voltage transients for pulsed deposition under the conditions depicted by the procedure Z2. The potential in both deposition (T_{on}) and relaxation steps (T_{off}) showed changes along the procedure: three regions in where the chemical change on the surface of the working electrode due to the preceding reactions control the evolution of its behavior can be identified. At the beginning of the procedures (Region 1: 0-72 s) an almost constant value of the potential around -1.06 ~ -1.07 V vs Ag/AgCl during plating was observed, values that suggest NO_3^- and H_2O reduction at the electrode surface leading to the formation of simonkolleite crystals onto the FTO surface. When the current flow is interrupted in this region, the potential quickly falls to -0.3 V vs Ag/AgCl indicating the discharge of the FTO substrate. Region 2 (72-168 s) shows a gradual increase of the potential during plating step (from -1.06 to -1.13 V vs Ag/AgCl) accompanied by a shift in the relaxation potential. The changes observed in region 2 suggest a capacitive behavior at the substrate/solution interface as the FTO surface begins to be completely covered by simonkolleite crystals. A shift of the relaxation potential to less negative values in region 3 possibly indicates the pass of charge through the interface that leads to the reduction reactions described above onto the simonkolleite crystals previously grown, increasing the film thickness.

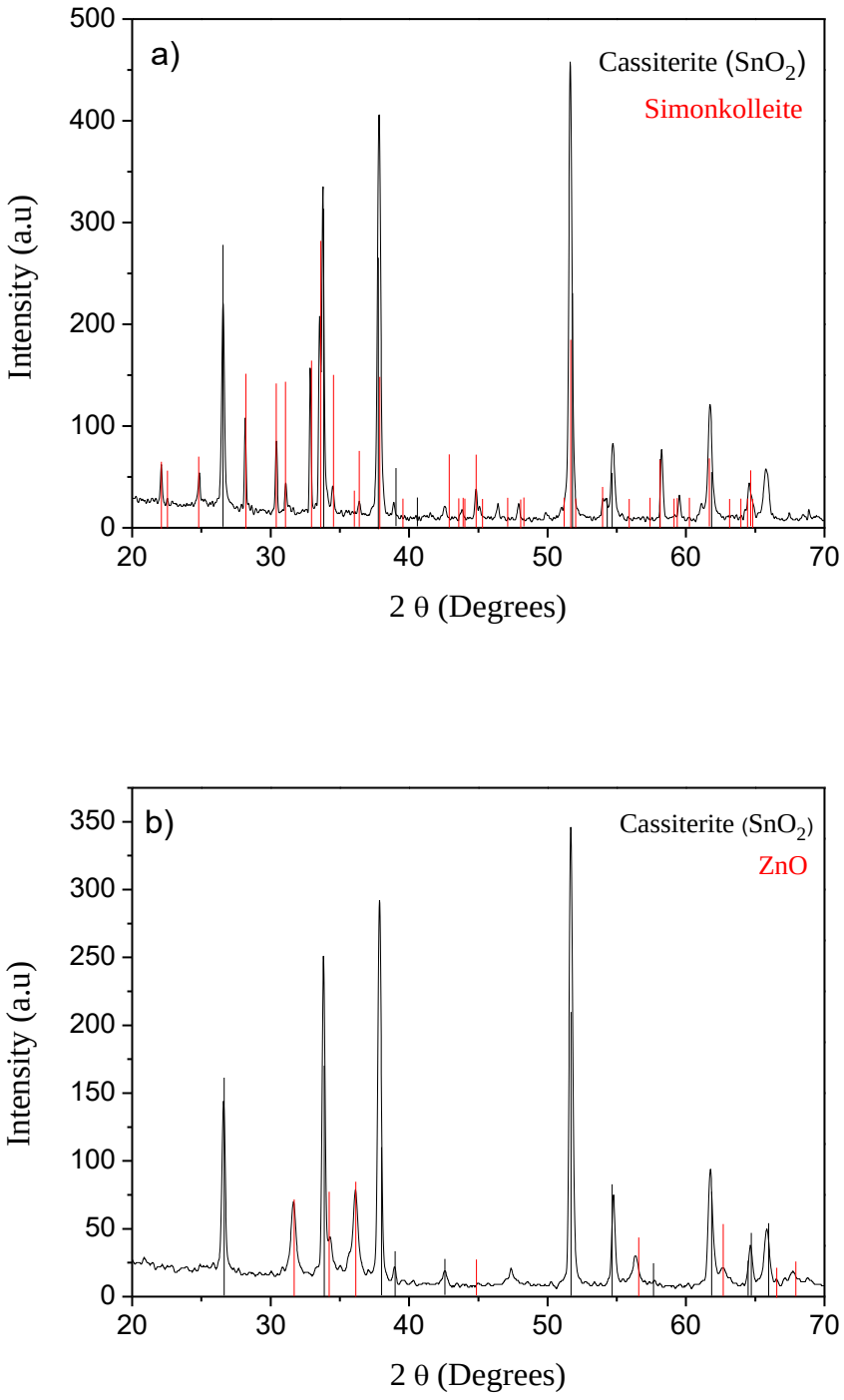

Figure 16.- X-ray diffraction patterns for a film obtained by pulsed electrodeposition onto FTO: a) without thermal treatment, b) after a 250 °C thermal treatment.

Studies on the thermal stability of the simonkolleite have shown that different Zn compounds and finally ZnO can be obtained after specific heating stages as follows [50]:

$$110\sim165\ ^{\circ}C \qquad Zn_5(OH)_8Cl_2 \bullet H_2O \text{ ----------> } Zn_5(OH)_8Cl_2 + H_2O \qquad (5.7)$$

$$165\sim210\ ^{\circ}C \qquad Zn_5(OH)_8Cl_2 \text{ ----------> } 2Zn(OH)Cl + ZnO + H_2O \qquad (5.8)$$

$$210\sim300\ ^{\circ}C \qquad 2Zn(OH)Cl \text{ ----------> } ZnCl_2 + ZnO + H_2O \qquad (5.9)$$

Figure 16a shows the XRD pattern for a film obtained by pulsed electrodeposition before the thermal treatment. Only reflections for simonkolleite and FTO were observed, confirming the prevalence of the mechanism described in equation 5.6; in addition, reflections associated to metallic Zn or $Zn(OH)_2$ were not found, indicating the high affinity that Zn^{2+} ions have to condensate as simonkolleite at that pH, temperature and bath composition.

Figure 16b presents the XRD pattern for the same film after being exposed at 250 °C for 1.5 h and soaked in distilled water for 3 h. Decomposition of simonkolleite in ZnO and $ZnCl_2$ (eq. 5.9) as well as the removal of the water soluble Zn phase can be achieved completely with these easy steps.

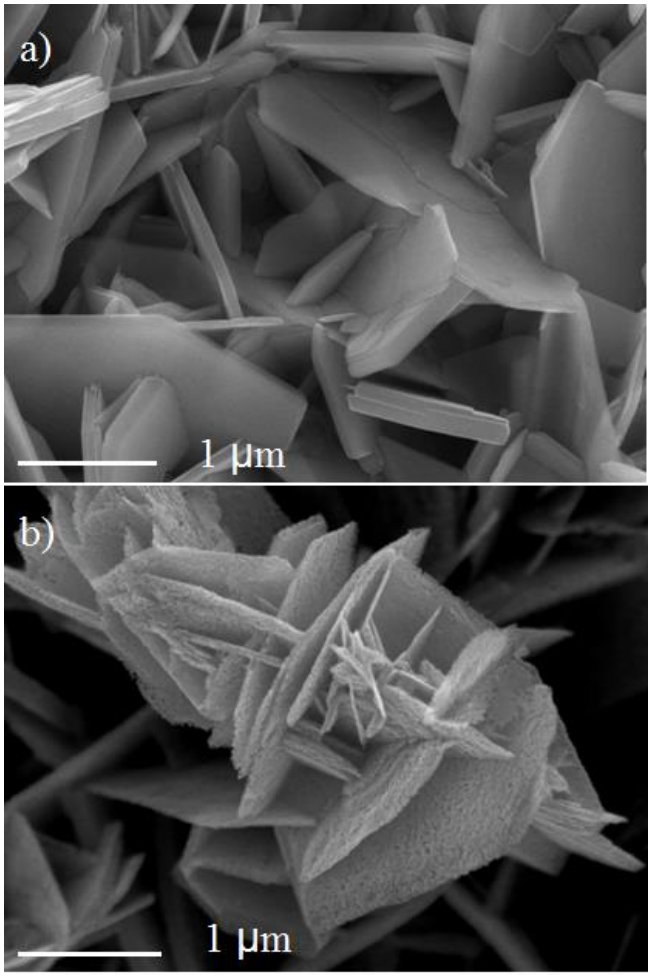

Figure 17.- SEM images for films obtained from a 0.1 M $Zn(NO_3)_2 \cdot 6H_2O$, 0.1 M KCl aqueous solution at pH= 6.0, 70 °C and 700 pulses of the procedure Z2: before (a) and after (b) a 250 °C thermal treatment.

Scanning electron microscopy (SEM) was employed to evaluate the morphology of the material synthesized by this route. Figure 17a shows that simonkolleite tends to electro-crystallize as well defined hexagonal sheets with low surface roughness and a non specific orientation with respect to the substrate; in addition, no dependence was found between the morphology and the number of pulses used, as can be seen in Figure A2. After thermal treatment of the film in the way previously described, the ZnO structures obtained (Fig. 17b)

still show the same hexagonal-sheets morphology, however a large amount of pores are now visible due to the dissolution of the $ZnCl_2$ grains after soaking the thermally treated film in water.

DSSCs were elaborated to evaluate the suitability of the ZnO obtained through this route in photovoltaic applications and relate the effect that the deposition conditions employed have on the overall performance. Below, some details on their elaboration:

- ZnO films were sensitized in a 0.5 mM OD-8 and 0.5 mM CDCA acetonitrile/t-butyl alcohol (1:1 v/v) solution for 2 h.

- An electrolyte solution 0.22 M $[Co(bpy)]^{2+}$, 0.05 M $[Co(bpy)]^{3+}$, 0.2 M TBP was used to fill the space between the photo anode and the Pt/FTO cathode.

It should be noted that no optimization has been performed yet in these devices and the following results are only to show that DSSCs can be prepared from this low temperature ZnO precursor.

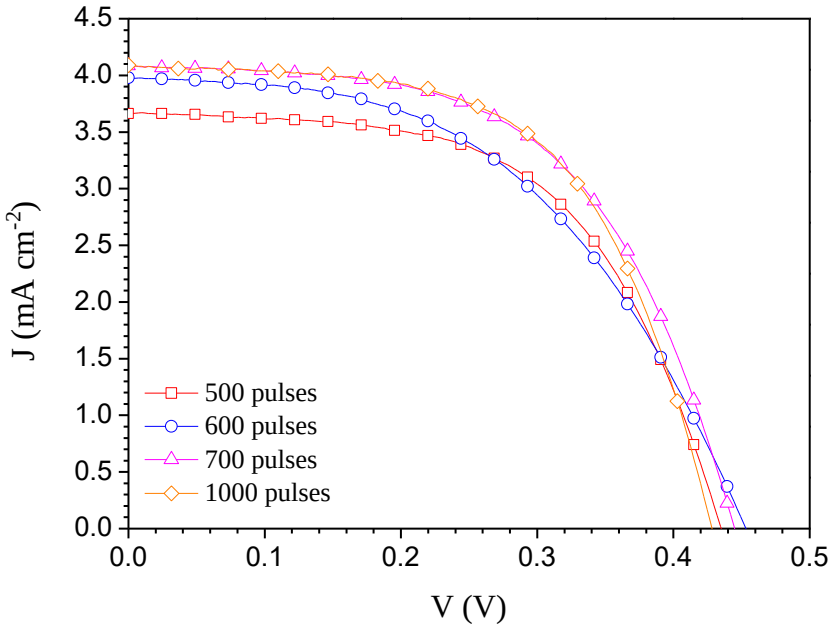

Figure 18.- I-V curves measured to DSSCs elaborated with ZnO films obtained from electrodeposited $Zn_5(OH)_8Cl_2*H_20$ as precursor, an electrolyte solution based in the $[Co(bpy)_3]^{2+/3+}$ redox couple and the organic dye OD-8.

Figure 18 presents a set of I-V curves measured on DSSCs prepared with ZnO films synthesized with the procedure Z2. An increase of the short-circuit current density was observed as a function of the number of pulses used; since the current measured in a DSSC is related (among other factors) with the amount of dye loaded that depends on the surface area of the particles and film thickness, we can interpret this result as a direct effect of the gradual increase of thickness up to 700 pulses. No difference was observed between the 700 and 1000 pulses cells, indicating that at some point in this range possibly the film stops to grow. Table 2 summarizes the parameters measured on these devices, where it is possible to

see that good quality DSSCs can be elaborated with simonkolleite films as precursor of crystalline ZnO.

Table 2. Short circuit current density (J_{SC}), open circuit potential (V_{OC}), efficiency (η) and fill factor (FF) for DSSCs made with different number of pulses.

# of pulses	Jsc (mA cm^{-2})	Voc (V)	η (%)	FF
500	3.67	0.434	0.914	0.57
600	3.98	0.453	0.886	0.49
700	4.09	0.444	1.024	0.56
1000	4.09	0.427	1.029	0.59

5.4 Conclusions

Mesoporous and nanostructured ZnO films with suitable characteristics for application in DSSCs have been obtained by galvanostatic electrodeposition either by the use of a current pulse at a steady-state current density or on-off pulsed procedures.

Different reaction schemes were observed depending on the Zn^{2+} precursor used, as cyclic voltammetry and X-ray diffraction experiments confirmed and, as a consequence, the nature and morphology of the deposited material. Semi-spherical ZnO particles were observed in the films electrodeposited from $ZnCl_2$/PVP40 baths due to the morphology-modulating effect of PVP40, a known effect in $Zn(NO_3)_2$ solutions but to our knowledge not yet reported in $ZnCl_2$ solutions, in which the Cl^- ions markedly tend to determine the (non-spherical)

morphology of the deposited material. In the case of the $Zn(NO_3)_2$/KCl baths, electrodeposition of simonkolleite crystals takes place, a promising precursor of crystalline ZnO for low-temperature applications, such as flexible-DSSCs, due to the relatively low sintering temperature needed to decompose this complex zinc compound to obtain highly porous, pure ZnO semiconducting films.

Finally, both materials have been used in the construction of DSSCs as electron transporting layers, with results that emphasize the good quality of the materials synthesized as well as the advantages of the electrochemical deposition routes. More details on the performance of the DSSCs prepared with the ZnO films obtained from $ZnCl_2$ solutions will be presented in the next chapter.

6. Fluorenyl-thiophene dye Sensitized ZnO-based Solar cells: Effects of redox couple and dye aggregation.

The use of organic dyes instead of the well known ruthenium complexes is a current trend in the fabrication of DSSCs not only for their superior optical properties but also for the so-called "blocking effect" they show on the semiconductor/electrolyte interface, which allows the use of fast redox couples increasing the open circuit potential, short circuit current density, and finally the overall performance of the solar devices when comparing with the traditional systems. On this observation, we have prepared solar cells with nanostructured, mesoporous ZnO films electrodeposited from an optimized aqueous $ZnCl_2$ solution, an organic fluorenyl-thiophene dye (OD-8) as sensitizer, and an electrolyte solution with either the I^-/I_3^- or the $[Co(2,2'\text{-bipyridyl})_3]^{2+/3+}$ redox couple. An improvement in efficiency may be expected, related to the more positive redox potential of the $[Co(2,2'\text{-bipyridyl})_3]^{2+/3+}$ couple and faster dye regeneration kinetics, but this can only be achieved if the recombination rate at the semiconductor/electrolyte interface is slow enough. Hence, we have evaluated the effect of CDCA (chenodeoxycholic acid) as coabsorbent in the dye solution, with the purpose to diminish the amount of uncovered area of the electrode surface (fig 19), in order to minimize recombination.

In this chapter we use current - potential curves in combination with intensity-modulated photovoltage spectroscopy, charge extraction measurements, and surface photovoltage spectroscopy to gain insight in the photochemical charge separation in ZnO-based organic-DSSCs.

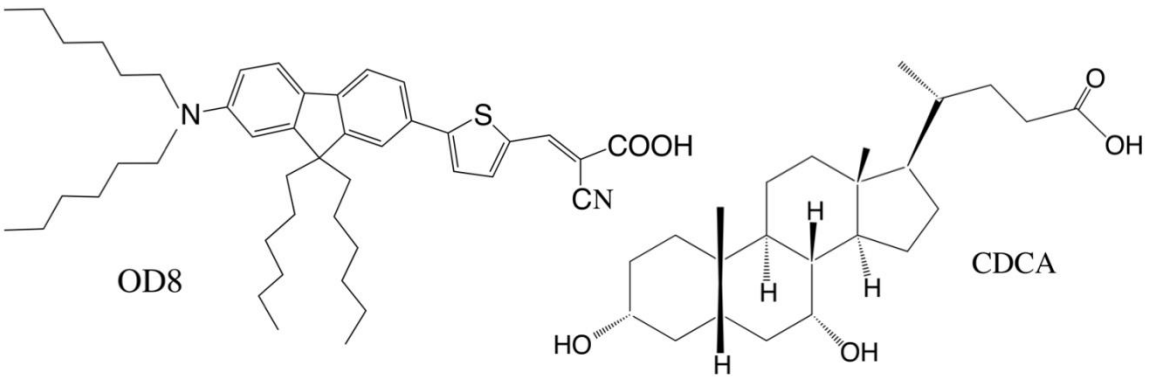

Figure 19.- Chemical structure of the organic dye (OD-8) and the coabsorbent (CDCA) used in this work.

6.1 Experimental procedure

Mesoporous ZnO films were deposited from a $ZnCl_2$, KCl and PVP40 bath as described in chapter 5. The thickness of the films was determined using a KLA Tencor D-120 profilometer.

The dye used in this work was the (Z)-2-Cyano-3-(5-(9,9-dihexyl-7-(dihexylamino)-9H-fluoren-2-yl)thiophen-2-yl)acrylic acid (OD-8; from Eversolar); 0.5 mM OD-8 and 0.5 mM CDCA solutions were prepared to dissolve the desired amounts of these reagents in a mixture of acetonitrile/t-butyl alcohol (1:1 v/v). ZnO films were heated at 90 °C for 20 min and immediately soaked in the dye solution (described above) for different times (1, 4, 8 and 24 h) in order to achieve sensitization. After sensitization, the films were removed from the dye solution and carefully washed with the same mixture of acetonitrile/t-butyl alcohol.

All the electrolyte solutions used were prepared in a 5 mL volumetric flask using acetonitrile as solvent. The cobalt redox couple consists of 0.22 M $[Co(2,2´\text{-bpy})_3][B(CN)_4^-]_2$, 0.05 M $[Co(2,2´\text{-bpy})_3][B(CN)_4^-]_3$ and 0.2 M 4-tert-butylpyridine. The I^-/I_3^- redox couple was prepared in the same molar ratio as for the Co-based redox couple, using 0.05 M I_2, 0.2 M TBP, and 0.27 M 1,2-dimethyl-3-propylimidazolium iodide.

Dye sensitized solar cells (DSSCs) were prepared with the sensitized ZnO films described previously and a FTO counter electrode with a thin coating of Pt, prepared by spreading a drop of Platisol (Solaronix) on the conductive side of the electrode and subsequent heating at 450 °C for 5 min. The photoanode and counter electrode were sealed in a sandwich configuration using a Surlyn (60 μm) separator by heating at 210 °C for 2.5 min. Finally, the electrolyte solution was introduced inside the cell through a pair of holes previously perforated in the counter electrode, which were subsequently sealed with Surlyn and microscope cover glass pressed under heating. Photovoltaic characterization was performed using a set-up consisting of a 450 W ozone-free Xe-lamp (Newport Corporation) with a water filter, calibrated to an irradiance of 100 mW cm^{-2} on the surface of the solar cell using an Air Mass 1.5 Global (AM 1.5G) optical filter (Newport Corporation). The intensity was calibrated using a certified 4 cm^2 monocrystalline silicon reference cell with incorporated KG-5 filter. Current–voltage curves (I–V), intensity modulated photovoltage spectroscopy (IMVS) and charge extraction measurements were recorded with an Autolab PGSTAT302N/FRA2 set-up (Metrohm Autolab). In charge extraction measurements, the dye-sensitized solar cells were illuminated under open circuit conditions until a steady photovoltage was obtained. The illumination was then switched off and the cell was switched to short circuit conditions where the resulting current collected for 90 s was integrated; this

integrated current corresponds to the electronic charge accumulated in the film. In the IMVS technique, a sinusoidal, small amplitude light perturbation at different frequencies superimposed on a bias light intensity is applied to the DSC under open circuit conditions. The transfer function between the modulated light intensity and the measured AC potential of the cell provides information on the electronic lifetime dynamics under open circuit conditions. IMVS measurements were performed at modulation frequencies between 1 mHz and 10 kHz. A red LED (625 nm) was used to illuminate the sample from the substrate side and it served both as the bias illumination and the small sinusoidally modulated probe beam.

UV-vis diffuse reflectance spectra were recorded on films using a Thermo Scientific Evolution 220 UV-Vis spectrometer.

Surface photovoltage (SPV) measurements were conducted under vacuum (1.6×10^{-4} mBar) on ZnO films over FTO substrate. A gold Kelvin probe (Delta PHI Besocke) served as the reference electrode. Samples were illuminated with monochromatic light from a 150 W Xe lamp filtered through an Oriel Cornerstone 130 monochromator with light intensity range of 0.1 to 0.3 mW cm^{-2}. The CPD spectra were corrected for drift effects by subtracting a dark scan. No correction for the variable light intensity from the Xe lamp was performed. Samples for SPS measurements were prepared by heating FTO/ZnO substrates at 310 ºC for 20 minutes followed by cooling to 80 ºC and followed by placement into the dye solutions for 1 hour to 24 hours. After sensitization, all films were rinsed with a mixture of acetonitrile/t-butyl alcohol (1:1 v/v) and stored in aluminium foil covered containers in the glovebox.

6.2 Electrochemical and optical characterization of redox couple and dye

The redox potential for the electrolyte solutions used in DSSCs was determined through near steady-state voltammetry. Figure 20 shows the current - potential curves obtained at a very low scan rate of 0.5 mV s^{-1} for the electrolyte solutions used in the solar cells. At conditions close to steady-state, the average potential where the current is zero corresponds to the redox potential (E*) of the couple. For the I^-/I_3^- redox couple, the redox potential is located at -0.170 V vs. Ag/Ag^+ while for the $[Co(bpy)_3]^{2+/3+}$ couple the redox potential is 0.014 V vs. Ag/Ag^+. Hence, the $[Co(bpy)_3]^{2+/3+}$ redox potential is 0.184 V more positive than that of the I^-/I_3^- redox couple, which implies that based on thermodynamic grounds a higher open circuit potential could be achieved in the DSSC [51–53], however, the open circuit potential may also be limited by the kinetics of the recombination process. Table 3 summarizes the electrochemical properties of the redox couples.

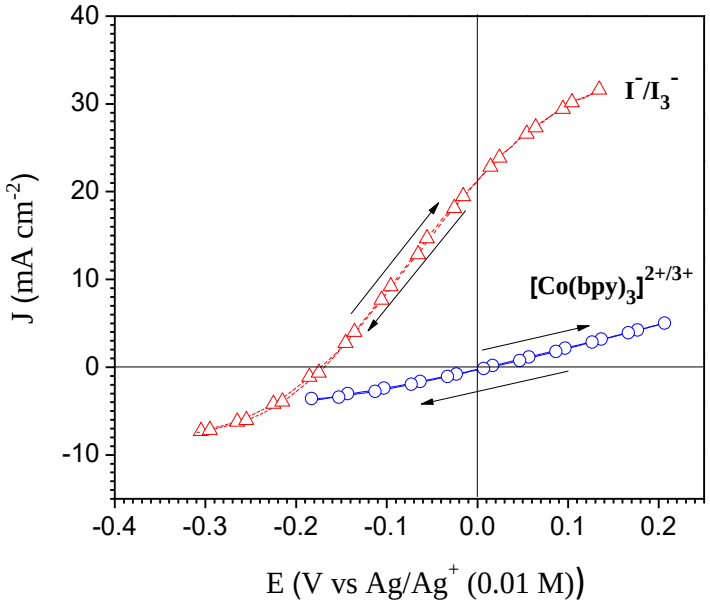

Figure 20.- Cyclic voltammetry at a scan rate of 0.5 mV s^{-1} for the electrolyte solutions: 0.22 M I^-, 0.05 M I_3^-, 0.2 M TBP in acetonitrile at a Pt electrode; 0.22 M $[Co(bpy)_3]^{2+}$, 0.05 M $[Co(bpy)_3]^{3+}$, 0.2 M TBP in acetonitrile at a Au electrode.

The two redox couples used in the acetonitrile-based electrolyte solution for the dye-sensitized solar cells were characterized using current - potential curves at a rotating disk electrode (RDE) as a function of the rotation rate. Figure A3 illustrates that the current - potential curves are characterized by current plateaus at sufficiently large overpotential in all cases, and the limiting current density versus the square-root of the angular rotation speed shows a linear behavior (Fig. 21) through the origin. The results indicate that the plateau current density is limited by diffusion according to the Levich equation (eq. 6.1):

$$I_L = 0.62\ n\ F\ D^{2/3}\ \nu^{-1/6}\ c^{\infty}\ \omega^{1/2} \qquad (6.1)$$

where I_L is the limiting current density (A cm^{-2}), n is the number of electrons involved in the reaction, F is the Faraday constant (C mol^{-1}), D is the diffusion coefficient of the electroactive species (cm^2 s^{-1}), ν is the kinematic viscosity of the solvent (4.484 x 10^{-3} cm^2 s^{-1} for acetonitrile), c^{∞} is the bulk concentration (mol cm^{-3}), and ω is the angular rotation speed (rad s^{-1}).

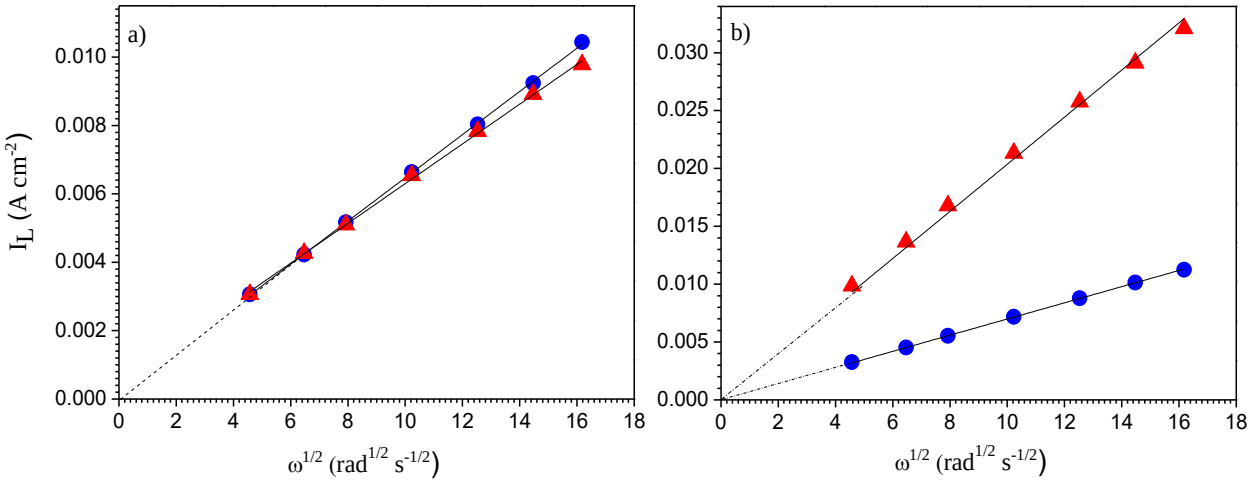

Figure 21.- Levich plots for: a) 10 mM $[Co(bpy)_3](PF_6)_2$ (circles) or 10 mM $[Co(bpy)_3](PF_6)_3$ (triangles), 0.1 M NH_4PF_6 in acetonitrile using a Au-RDE; b) 10 mM I^- (circles), 10 mM I_3^- (triangles), 0.1 M NH_4PF_6 in acetonitrile, using a Pt-RDE; all measurements were performed at 25 °C and a scan rate of 50 mV s^{-1}.

The Levich analysis allows us to determine the diffusion coefficients for both the reduced and oxidized species of the $[Co(bpy)_3]^{2+/3+}$ and I^-/I_3^- redox couples. In Table 3, the results are

summarized, and it can be observed that the diffusion coefficients for the I^-/I_3^- redox couple are about twice as large as those of the $[Co(bpy)_3]^{2+/3+}$ couple, which is likely related to the larger size of the latter molecules [11,51,52], since the addition of 0.1 M NH_4PF_6 in the electrolyte solution ensures in a good degree the absence of migration currents.

Table 3.- Diffusion coefficients and redox potentials calculated by electrochemical techniques. The values presented here are in a good agreement with the ones reported in literature [11,54].

Electroactive specie	**D ($cm^2 s^{-1}$)**	**Redox reaction**	**E* (V vs Ag/Ag^+)**	**E* (V vs NHE)**
I_3^-	1.8×10^{-5}	$I_3^- + 2e^- <----> 3I^-$	-0.17	0.37
I^-	1.9×10^{-5}			
$[Co(bpy)_3]^{3+}$	8.7×10^{-6}	$[Co(bpy)_3]^{3+} + e^- <----> [Co(bpy)_3]^{2+}$	0.014	0.554
$[Co(bpy)_3]^{2+}$	9.2×10^{-6}			

In order to determine the HOMO level of the dye, cyclic voltammetry was carried out for the OD-8 dye in solution and adsorbed onto an electrodeposited ZnO film. For the dye in solution (Fig. 22a), the electrochemical characterization was performed using platinum as working and counter electrodes and a 0.5 mM OD-8 + 0.1 M $[Bu_4N][PF_6]$ electrolyte solution in acetonitrile. Oxidation and reduction peaks attributed to the $(OD\text{-}8)^0/(OD\text{-}8)^+$ redox couple are observed at 0.403 V and 0.312 V vs. Ag/Ag^+, respectively. The observation that the cathodic and anodic current maxima are essentially the same in magnitude and that the peak separation is about ≈ 91 mV indicates that the redox reaction is close to reversible. Cyclic voltammetry of dyed ZnO films, prepared using a soaking time of 1.5 h in a 0.5 mM OD8 + 0.5 mM CDCA solution in acetonitrile/tert-butyl alcohol (1:1 v/v), shown in Figure 22b, reveals oxidation and reduction peaks at 0.453 and 0.370 V vs. Ag/Ag^+, respectively, with a

peak separation of ≈ 83 mV and symmetric oxidation and reduction waves at a scan rate of 50 mV s^{-1}. For the dye adsorbed on the ZnO surface, a slight shift of the redox potential to more positive values (approximately 62 mV with respect to the E* calculated in solution) was observed due to the interaction between ZnO and dye. Table 4 summarizes the electrochemical properties measured for the OD-8 dye.

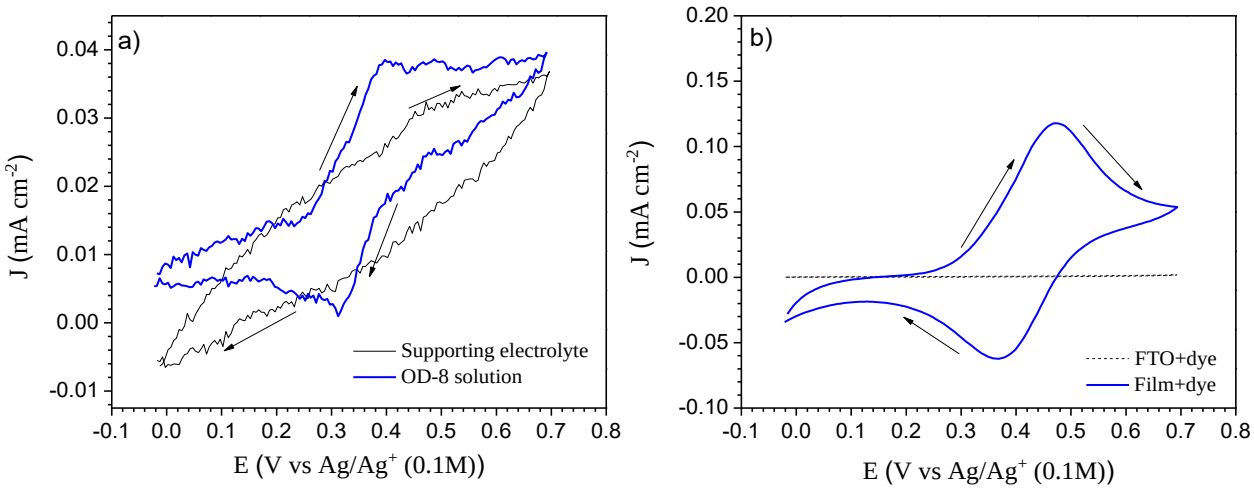

Figure 22.- a) Cyclic voltammetry at 50 mV s^{-1} for 0.5 mM OD-8 + 0.1 M $[Bu_4N][PF_6]$ in acetonitrile on a Pt working electrode; the supporting electrolyte measurements were performed on 0.1 M $[Bu_4N][PF_6]$ in acetonitrile; b) Cyclic voltammetry at 50 mV s^{-1} for OD-8 adsorbed onto a nanostructured, mesoporous ZnO film in a 0.1 M $[Bu_4N][PF_6]$ solution. Experiments were performed at 25 °C. The redox potentials (E*) for the dye in solution and adsorbed on ZnO films was calculated as the arithmetic mean value of the anodic and the cathodic peaks potentials in the voltammograms.

The absorbance spectra of the dye in acetonitrile/t-butyl alcohol solutions was determined through UV-vis spectrophotometry (Fig. 23). An intense absorption band was observed at 472 nm, related to the photoexcitation of the dye molecule that leads to the injection of

electrons from the dye excited state to the metal oxide conduction band when the molecule is anchored to the semiconductor surface; a molar extinction coefficient (ε) of 24,190 M^{-1} cm^{-1} was calculated for this absorption band, which is almost twice of the values reported for the widely used ruthenium-based N719 dye (Fig. A4) [55].

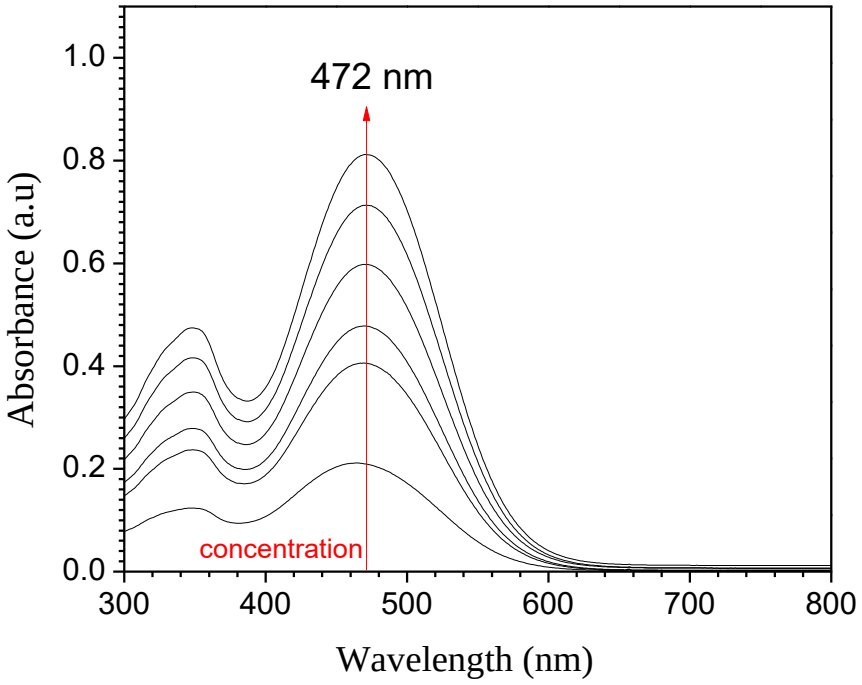

Figure. 23.- UV-vis spectra for the OD-8 dye in solution at various concentrations.

Table 4.- Data obtained from cyclic voltammetry for the dye in solution and adsorbed on ZnO films.

	OD-8 in solution	**OD-8 adsorbed onto ZnO**
E_{ox} (V vs Ag/Ag^+)	0.405	0.469
E_{red} (V vs Ag/Ag^+)	0.312	0.373
E* (V vs Ag/Ag^+)	0.359	0.421
E* (V vs NHE)	0.899	0.961
E_{HOMO} (eV) (estimated)[a]	-5.399	-5.461

[a] Calculated through the following expression : $E_{HOMO}(eV) = -[E^*(V \text{ vs NHE}) + 4.5]$

6.3 Photovoltaic performance: redox couple and dye aggregation.

Dye-sensitized solar cells were prepared using electrodeposited nanostructured, mesoporous ZnO films with a thickness of 9.23 ± 0.74 µm, the OD-8 dye, the CDCA coabsorbent, and both redox couples. Figure 24 presents a set of current - voltage curves for DSCs using the $[Co(bpy)_3]^{2+/3+}$ redox couple as a function of the immersion time of the ZnO films in the sensitizing OD-8/CDCA solution; after sensitization, the solar cell was assembled as described in section 6.1. The results are summarized in table 5.

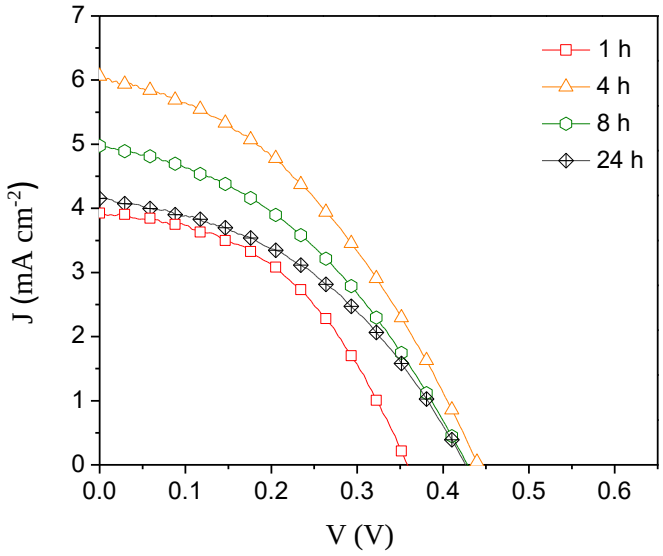

Figure 24.- Current density - voltage curves for electrodeposited ZnO-based DSCs with the organic dye OD-8, the CDCA coabsorbent, and $[Co(bpy)_3]^{2+/3+}$ redox couple as a function of sensitization time.

The progressive increase of the short circuit current density (J_{SC}) up to 4 h immersion time is related with the gradual increase of the number of dye molecules adsorbed to the ZnO surface (Figs. 28a, 28c). However, at longer immersion times J_{SC} decreases significantly, which can be interpreted in terms of the reported limited stability of ZnO in acidic media. Since the OD-8 dye has a carboxylic acid moiety as anchoring group, the dye solution is somewhat acidic, and ZnO has been known to partially dissolve and form Zn^{2+}-dye aggregates, which may block the pores in the nanostructure [17,20,56,57]. Although the aggregates are difficult to observe with SEM, the ZnO surface tends to become smoother with longer immersion times, which may be related to selective dissolution of ZnO material that can be incorporated in aggregates (Fig. 25).

Table 5.- Short current density (J_{SC}), open circuit potential (V_{OC}), fill factor (FF) and efficiency (η) for DSSCs at different sensitization times and redox couples.

Redox couple	**Time (h)**	**J_{SC} (mA cm^{-2})**	**V_{OC} (V)**	**FF**	**η (%)**
	1	3.91±0.18	0.34±0.02	0.46±0.01	0.62±0.06
	4	5.87±0.18	0.44±0.01	0.38±0.03	0.97±0.07
	8	5.39±0.4	0.42±0.01	0.4±0.02	0.91±0.11
$[Co(bpy)_3]^{2+/3+}$	24	4.2±0.16	0.41±0.02	0.46±0.05	0.79±0.14
I^-/I_3^-	4	4.47±0.27	0.58±0.03	0.26±0.02	0.66±0.03

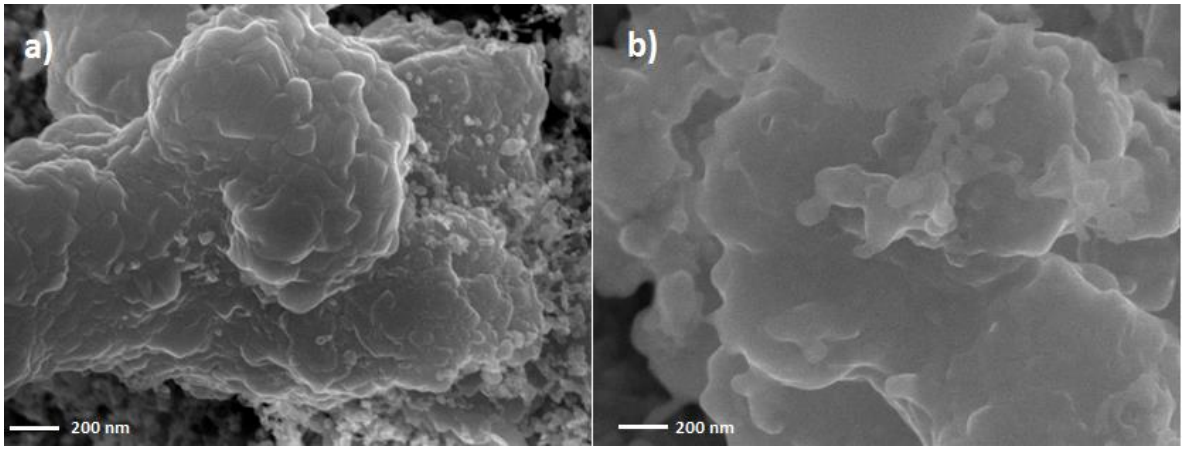

Figure 25.- SEM images taken to ZnO films before (a) and after 24 h of immersion (b) in a OD-8 dye solution.

The Zn^{2+}-dye aggregates may provide optical absorption, explaining the "colorful" appearance of the film, however, generally electron injection into the ZnO conduction band does not appear to occur from these aggregates. This interpretation is confirmed by surface photovoltage spectroscopy in combination with optical reflectance measurements on ZnO films sensitized at 1 and 24 h in the sensitizing dye solution. In figure 26, a more intense band can be seen at 2.7 eV (459 nm) in the optical spectrum for the ZnO film after 24 h of sensitization; however, the contact potential difference (ΔCPD) at that energy is in fact somewhat smaller than for the 1 h sample. Hence, in agreement with the desorption measurements shown in figure 28c, the higher absorption observed is related with the presence of more dye molecules in the mesoporous film after 24 hours, but the injection efficiency appears lower, resulting in a smaller ΔCPD signal; in addition, the spectrum is more noisy for the 24 h sample, which may be an indication of the presence of aggregates. Note that the lower injection efficiency is in agreement with the observation that the short circuit photocurrent is smaller for DSSC after 24 h of sensitization.

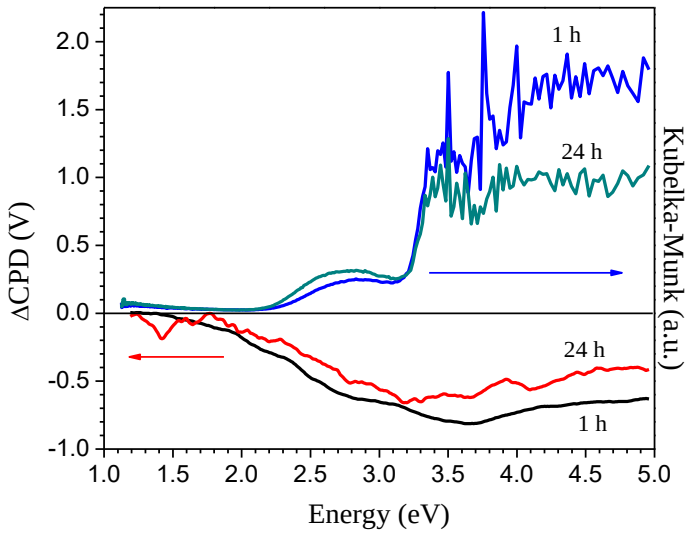

Figure 26.- Contact potential difference obtained from surface photovoltage spectroscopy and Kubelka-Munk function corresponding to the diffuse reflectance measured for dye-sensitized, electrodeposited ZnO film as a function of the sensitization time.

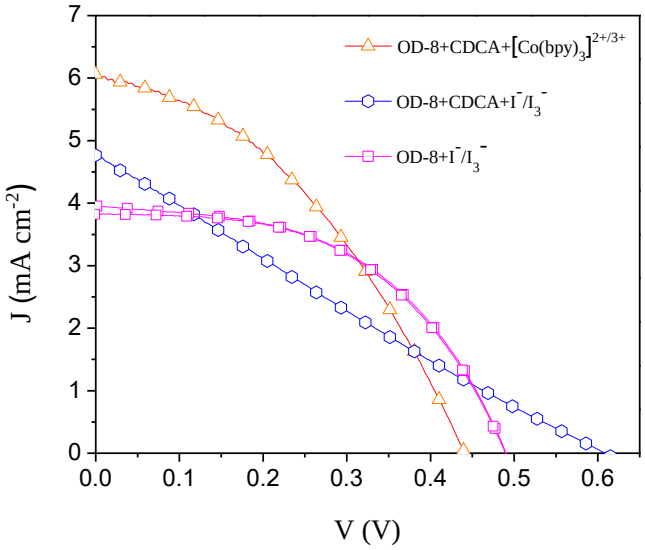

Figure 27.- Current density - voltage curves for electro-deposited ZnO-based DSSCs with the organic dye OD-8 sensitized for 4 h, for the two different redox couples used; in addition, a current-

voltage curve for a DSC with the I^-/I_3^- redox couple and a ZnO film sensitized for 2 h in a OD-8 dye solution without CDCA is presented.

Figure 27 shows the current - voltage curves for DSSCs prepared with the optimal 4 h immersion time for both redox couples. A pronounced difference in the fill factor (FF) is observed, where the solar cell prepared with the I^-/I_3^- redox couple shows the lower value. The diffusion coefficients determinate for the I^-/I_3^- redox couple are a factor 2 larger than for the $[Co(bpy)_3]^{2+/3+}$ redox couple, hence, one would not expect diffusion of the redox couple in the bulk solution to be a reason for the smaller fill factor for the I^-/I_3^- redox solution. However, transport of the redox couple in the mesoporous film is expected to depend on the interaction between the redox couple and the ZnO surface, the dye and the co-adsorbent; it appears that this combination of interactions causes the lower fill factor for the I^-/I_3^- solar cells. In fact, we have observed that if the co-adsorbent CDCA is not used, the classical I-V diode-shaped curve is recovered for the I^-/I_3^- solar cells; however, in the absence of CDCA, the DSSCs with the $[Co(bpy)_3]^{2+/3+}$ redox couple have a very low efficiency. Hence, for sake of comparison, we used the same solution chemistry for both redox couples.

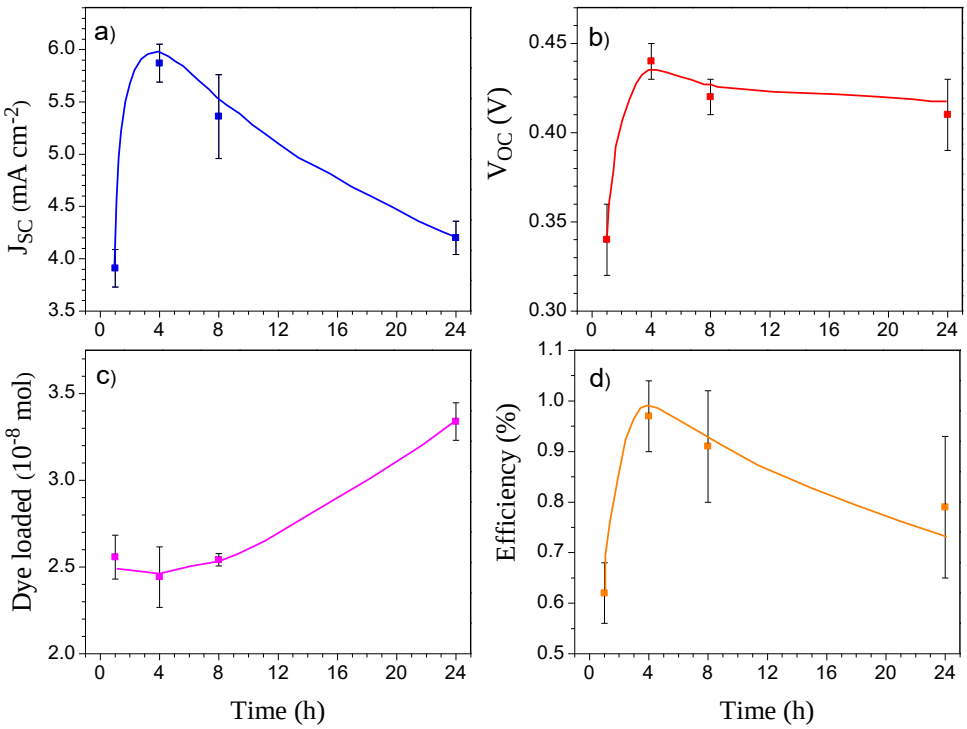

Figure 28.- Evolution of: a) short circuit current density, b) open circuit potential, c) dye loading, and d) efficiency of ZnO-OD8-$[Co(bpy)_3]^{2+/3+}$ based DSCs as a function of sensitization time.

The open circuit potential (V_{OC}) on the other hand increases with the immersion time, without showing a reversal in trend (Fig. 28b). This is generally observed for dye-sensitized solar cells (and many other types of solar cell) if the recombination kinetics do not increase markedly with dye coverage: upon increasing the dye coverage, the injection current increases, hence, in order to achieve zero current by balancing the injection with recombination rate, a higher voltage is required. The dependence of recombination rate on voltage thus defines V_{OC}. On the other hand, the recombination rate may actually decrease due to a better surface passivation with increased dye and / or co-adsorbent (CDCA)

coverage; this would also lead to an increase in V_{OC} with immersion time. However, since the decrease in J_{SC} is much more pronounced than the increase in V_{OC}, an optimum sensitization time exists for the ZnO - OD-8 dye system.

Figure 29 shows a band diagram illustrating the effects of the change in redox potential on the energetics and kinetics of the DSC: for the same quasi-Fermi level under open circuit conditions corresponding to the FTO/ZnO electrode, assuming the change in redox couple does not lead to a shift of the band edges, the open circuit potential of the DSC is expected to be 184 mV larger for the $[Co(bpy)_3]^{2+/3+}$ redox couple, but only if: (i) dye regeneration is sufficiently fast, and (ii) recombination of ZnO electrons with the oxidizing agent is sufficiently slow. If dye regeneration is slow due to the smaller driving force for the regeneration process with the $[Co(bpy)_3]^{2+/3+}$ redox couple, then recombination of ZnO electrons with the oxidized dye is expected to limit the open circuit voltage; if recombination of ZnO electrons with the oxidizing agent is fast, then the thermodynamically attainable open circuit potential cannot be maintained, and will be smaller than expected.

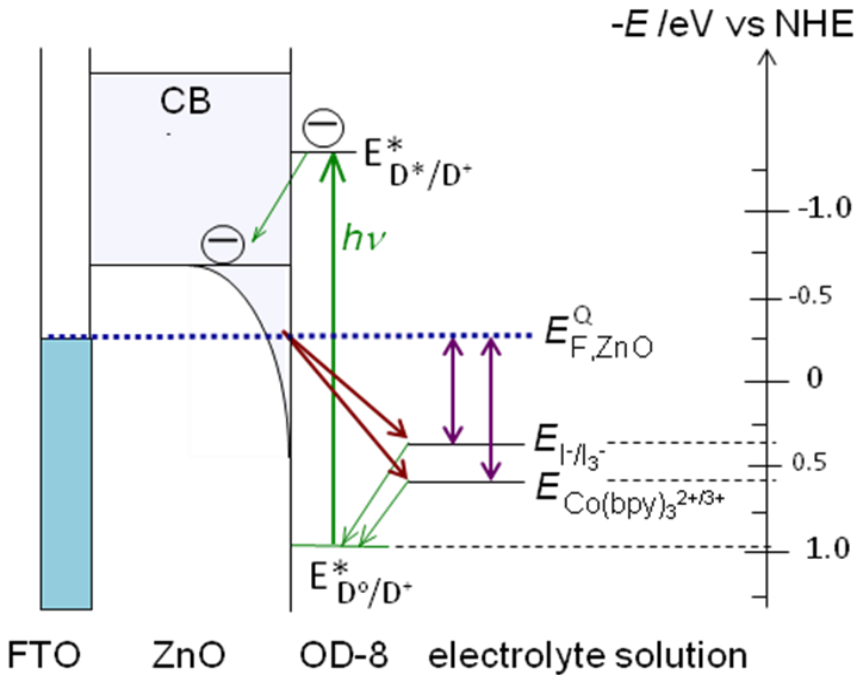

Figure 29.- Schematic band diagram illustrating the effect of the redox potential on the attainable open circuit potential of the DSC. If the recombination processes are sufficiently slow, then the open circuit potential is expected to be larger for the cells with the $[Co(bpy)_3]^{2+/3+}$ redox couple.

However, as can be observed from Figure 27 and Table 5, the open circuit potential for the cells with the $[Co(bpy)_3]^{2+/3+}$ redox couple was around 140 mV smaller than obtained for I^-/I_3^- solar cells. This can be related with the recombination processes that govern the efficiency of the DSSC.

In order to obtain a better insight into these processes, 3 cells of each redox couple were characterized via charge extraction and IMVS measurements. In charge extraction measurements, the cell is held at open circuit under illumination until the system is stable, and then the illumination is switched off and the cell is switched to short circuit

simultaneously, and the current transient corresponding to equilibration under dark conditions is integrated to obtain the charge. In IMVS, the cell is held at open circuit under illumination, and a small, sinusoidally modulated light intensity is applied to the cell and the corresponding modulated photovoltage is measured as a function of modulation frequency. In general, a single time constant is estimated from the frequency at the apex (inflection point) of the semicircle in the corresponding Nyquist plot (fig. A5), which is proportional to the electron lifetime (τ_n^{IMVS}). Both experiments are performed as a function of steady-state light intensity.

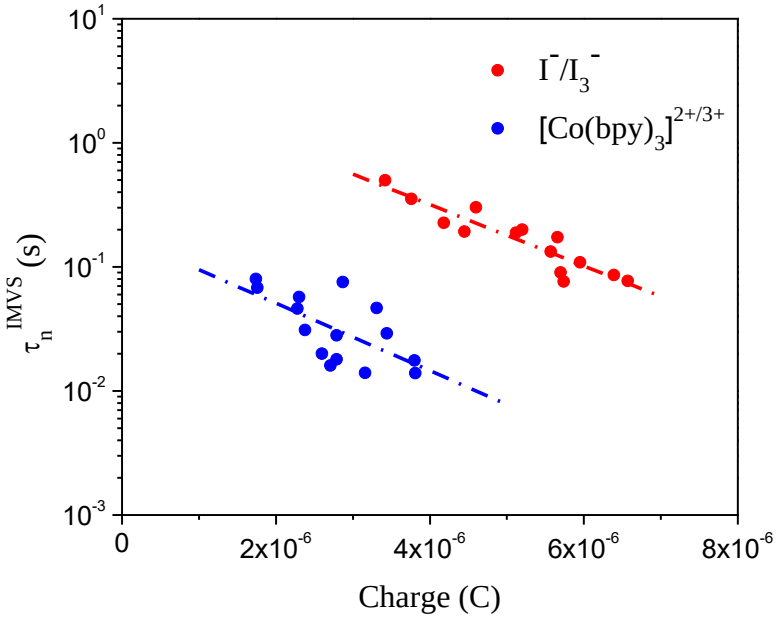

Figure 30.-Electron lifetime as a function of the amount of charge extracted. The data presented was obtained for three cells with each redox couple.

The linear trend observed in the semi-log plot of the electron lifetime with the charge extracted (fig. 30) is related with an exponential distribution of traps below the conduction

band, previously reported for TiO_2 and ZnO-based DSSCs[58], and schematically illustrated in Figure 29. The trap distribution parameter obtained from the slope is very similar for both redox couples, indicating that the general dependence of the trap states density with the charge concentration in the semiconductor is not affected by the redox potential in the electrolyte solution [59]. As can be seen in Figure 30, at the same charge, corresponding to the same quasi-Fermi level with respect to the ZnO conduction band edge, the electron lifetime is about 70x larger for the cells with the I^-/I_3^- redox couple. In addition, it can be seen that larger values for the charge can be extracted for the cells with the I^-/I_3^- redox couple, indicating that the quasi-Fermi level reached at a certain light intensity is higher than for the $[Co(bpy)_3]^{2+/3+}$ cells, corresponding to the capability to maintain a larger open circuit potential. These results imply that the OD-8 dye and CDCA treatment does not achieve complete passivation of the ZnO surface, allowing recombination corresponding to electron transfer from the ZnO to the $[Co(bpy)_3]^{2+/3+}$ redox couple.

6.4 Surface Photovoltage Spectroscopy (SPS): Characterization of Photochemical Charge Separation in ZnO-Based Dye-Sensitized Solar Cells

Surface photovoltage spectroscopy was performed on electrodeposited ZnO films onto FTO substrates, sensitized in a OD-8/CDCA solution and treated with a drop of the electrolyte solution for both redox couples using a Kelvin probe in a vacuum system.

Figure 31a shows the SPS results for ZnO films electrodeposited onto a FTO substrate. The ΔCPD signal starts to increase at a photon energy of about 3.2 eV (section III in the Figure), which corresponds to the band gap of ZnO. Hence, upon light absorption, electrons are excited from the valence band to the ZnO conduction band and charge separation is sustained, giving rise to a negative voltage. A negative voltage is typical for an n-type semiconductor, where electrons are driven to the FTO/ZnO interface and holes are trapped at the ZnO free surface [32] [31]; a maximum ΔCPD signal of -0.18 V was obtained for the ZnO film. At higher photon energy, both the light intensity of the Xenon lamp and the penetration depth of the photons decrease, leading to a decrease in the signal.

After sensitization (Fig. 31b) a shift in the ΔCPD onset to a lower energy (1.7 eV) was observed, as well as a first maximum at 2.7 eV, resembling the absorbance spectrum of the dye (Fig. 32). Hence this signal can be ascribed to absorption by the dye, and subsequent charge separation; charge separation occurs by electron injection from the dye in the excited

state into the ZnO conduction band, leaving behind an oxidized dye molecule. In this situation, recombination can occur by back electron transfer from the ZnO conduction band to the oxidized dye molecules attached to the semiconductor surface, a process that in the dye-sensitized solar cell needs to be intercepted by faster dye regeneration by an electron donor in solution. In this case, the absence of the redox couple allows electron back transfer to occur, and the steady-state photovoltage is rather low at only -0.04 V. The signal then decreases slightly up to a photon energy of 3.2 eV, where the ΔCPD starts to increase again, which corresponds to a contribution of the absorption of ZnO due to band-to-band transitions and subsequent transfer of the photogenerated hole to the dye molecule. Hence, sections I and II in Figure 31 correspond to the region where the dye absorbs light, while sections III and IV correspond to absorption by ZnO. Note that although dyes are specifically designed to have slow back transfer kinetics, taking into account that the dye is chemisorbed to the ZnO surface, the intimate electronic contact allows relatively fast back electron transfer, at least as compared to electron transfer from the ZnO conduction band to a non-adsorbed redox couple in solution.

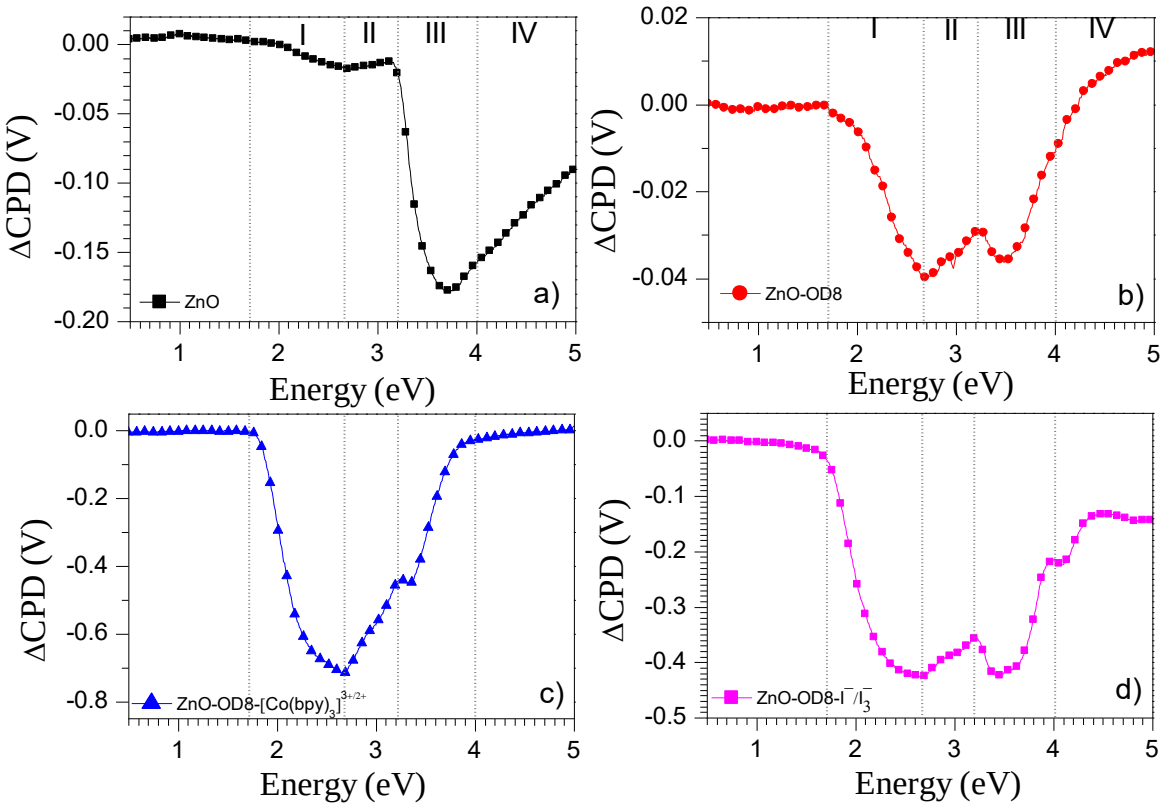

Figure 31.- Surface photovoltage measurements for: (a) Electrodeposited ZnO film; (b) ZnO film sensitized with OD-8; (c) ZnO film with OD-8 and the $[Co(bpy)_3]^{3+/2+}$ redox couple; and (d) ZnO film with OD-8 and the I^-/ I_3^- redox couple.

Figure 31c shows the ΔCPD signal obtained for a sensitized-ZnO film with a dry thin layer of the $[Co(bpy)_3]^{3+/2+}$ redox couple solution placed upon it. The spectrum follows the same trend as in Figure 31b, illustrating that the optical absorption by the $[Co(bpy)_3]^{3+/2+}$ redox couple can be neglected. The ΔCPD onsets at 1.7 eV and 3.2 eV indicate the absorption edges of the dye and ZnO, respectively. However, the surface photovoltage is significantly larger compared to the situations without the redox couple; at 2.7 eV, the ΔCPD maximum is -0.70 V, compared to -0.04 V in the absence of the redox couple. This result indicates that charge

separation can be maintained even at a large voltage, implying that the recombination process has become much slower. This can be understood as follows: upon light absorption and electron injection, instead of electron back transfer from ZnO as in the case of Figure 31b, the oxidized dye accepts an electron from the redox couple, and the positive charge is "stored" on the oxidized redox couple. Consequently, the recombination reaction now pertains to the electron transfer from the ZnO conduction band to the oxidized species of the redox couple, $[Co(bpy)_3]^{3+}$, which is much slower than the back electron reaction to the oxidized dye. This interpretation is in agreement with the general kinetics scheme in the dye solar cell: fast dye regeneration prevents electron back transfer from ZnO to the oxidized dye, and the much slower recombination kinetics corresponding to electron transfer from ZnO to the oxidized species of the redox couple allows for a larger cell voltage.

The addition of the I^-/I_3^- redox couple (Fig. 31d) to the sensitized films showed similar characteristics in the SPS spectra as observed for the cobalt-based redox couple, however, the ΔCPD_{MAX} at 2.7 eV was some smaller (-0.45 V compared to the -0.70 V for the $[Co(bpy)_3]^{3+/2+}$ redox couple).

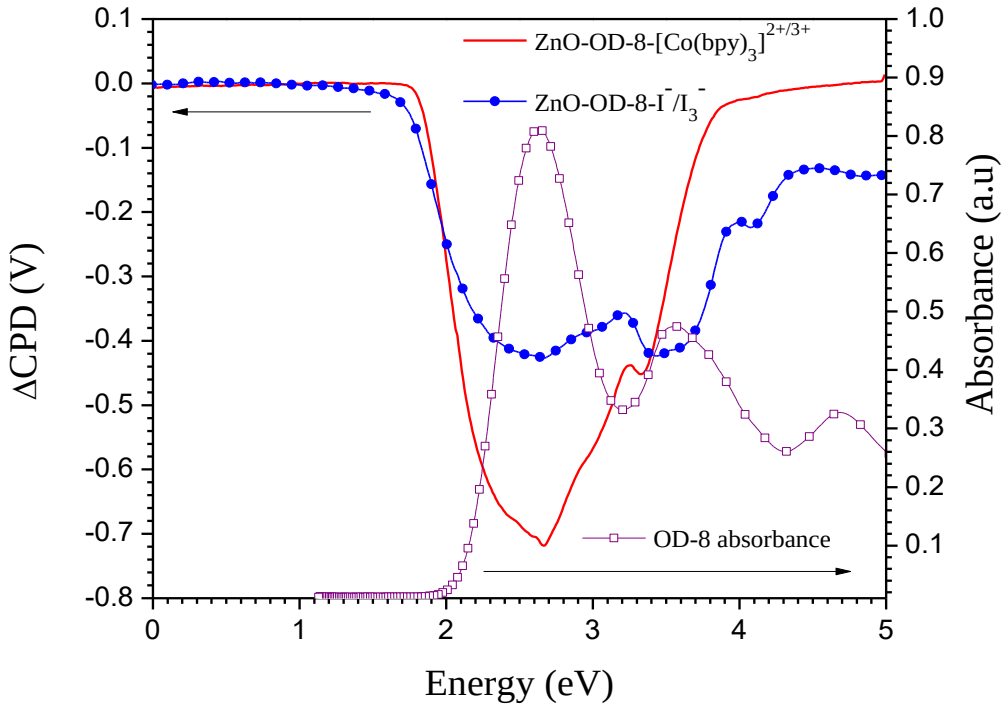

Figure 32.- SPS results for ZnO films sensitized with the OD-8 dye and with a drop of either the I^-/I_3^- or the $[Co(bpy)_3]^{3+/2+}$ redox couple; the absorbance spectra of the OD-8 dyes is also presented.

The difference in ΔCPD_{MAX} between these redox couples (fig. 32) is an interesting result, possibly more related with the regeneration efficiency of the dye cation after electron injection (since the different conditions of the electrolyte solution in the SPS vacuum measurement system prevent efficient mediation of the electron transfer from the semiconductor to the oxidized redox couple). Detailed studies on the iodine/iodide system have shown the presence of a number of one-electron redox reactions with a significant importance in the DSSCs, including the $I^{\bullet}/I^-$ or the $I_2^{-\bullet}/I^-$ redox couples. Thus, it is the I^-/I_3^- redox couple that sets the potential of the Pt-counter electrode (and the V_{oc} in the dye-

sensitized solar cell), but it is the $I_2^{-\bullet}/I^-$ redox couple (≤ 0.93 V vs NHE) that is responsible for reduction of the oxidized dye molecule in the SPS configuration [24][60]. In this way, a small driving force for the dye regeneration reaction with the $I_2^{-\bullet}/I^-$ redox couple (compared with the $|E^*([Co(bpy)_3^{2+/3+})\text{-}LUMO_{OD\text{-}8}|$= 0.407 V) seems to limit the charge separation at the ZnO/OD-8 interface mainly for the high recombination of the electrons injected in the semiconductor with the dye cations.

6.5 Conclusions

We have evaluated the performance of dye-sensitized solar cells based on electrodeposited nanostructured, mesoporous ZnO films sensitized with the organic OD-8 dye, in combination with two types of redox couple: the one-electron couple $[Co(bpy)_3]^{2+/3+}$ and the two-electron couple I^-/I_3^-. Electrochemical characterization of the two redox couples illustrate that the redox potential of the $[Co(bpy)_3]^{2+/3+}$ couple is about 0.18 V more positive than that of the I^-/I_3^- couple, however, a corresponding increase in the solar cell open circuit potential is not achieved. Steady-state current-voltage measurements as a function of the immersion time in the dye solutions show a decrease in performance after a sensitization time of approximately 4 hours, and results from scanning electron microscopy and surface photovoltage spectroscopy show that this is likely related to the formation of Zn^{2+}-dye aggregates in the pores of the ZnO film, lowering the injection efficiency and thus the short circuit current density. Combining the results from electron lifetime measurements and open circuit charge extraction leads to the conclusion that the electron transfer kinetics from ZnO to $[Co(bpy)_3]^{3+}$ are much faster than to I_3^-, which limits the V_{oc} and the performance of the ZnO-OD-8-

$[Co(bpy)_3]^{2+/3+}$ cells. However, the SPS results suggest a more efficient dye regeneration with this redox couple observed as a larger ΔCPD signal, in agreement with the J_{sc} measured in the solar devices.

Based on these results, it is concluded that higher efficiencies for the ZnO/OD-8 system can be obtained with the use of the $Co(bpy)_3]^{2+/3+}$ redox couple. In order to achieve this, an effective ZnO surface passivation method is needed to slow down the electron transfer rate at the semiconductor/electrolyte interface, which may lead to an increase in the open circuit potential and the short circuit current density of the cells, related to an increase in the collection efficiency for an improved electron diffusion length.

7. New metal-free dyes based on perylene-monoanhydride-monoimides applied to ZnO-DSSCs.

In this section a series of metal free dyes based on perylene derivatives (Fig. 33) were tested as molecular absorbers in which an anhydride group has been incorporated as anchoring group. The mechanism proposed for the rupture of that group (which leads to the molecule adsorption) does not imply the release of protons in the sensitizing solution. This anchoring group was specifically designed to try to improve the stability of the semiconductor during the sensitization process by avoiding the undesirable formation of dye aggregates usually observed with dyes having carboxylic an cyanoacrylic acid groups as anchoring groups. In the design of these dyes, changes in the position and number of the electron donating units in the perylene core as well as the size of the alkyl chains that substitute the imide group have a clear effect on their optical and energetic properties, and finally on the performance of the solar cell devices.

Only a few works on the use of perylene-monoanhydride derivatives as sensitizers in ZnO-based DSSCs can be found in the current literature, so that the aim of this chapter is to evaluate the performance of the non-commercial DG-perylene dyes applied to ZnO-based solar devices in terms of stability of the semiconductor as function of the sensitization time as well as photovoltaic performance related with their structural, optical and energetic features. These dyes were synthesized by the group of Dr. Angela Sastre from Elche University in Spain specifically for this collaborative research project and have not been reported previously.

In this work, we compared the performance of solar cells based on ZnO and TiO_2, which were both synthesized using solvothermal methods.

7.1 Experimental procedure

Porous films were prepared by depositing a home-made paste of ZnO nanoparticles (ZNW15WT%-GO, CIK), PEG 20000, PEG 500000 and Triton X (as surfactant), or a TiO_2 paste (PST-18NR, JGC catalysts and chemicals Ltd.) onto FTO (Asahi) conducting glass by the doctor blade technique, and sintering at 550 ºC or 450ºC ,respectively, for 30 minutes. The thickness of these films was measured with a stylus profiler DEKTAK 6M.

Pre-heated films were sensitized in perylene (0.5 mM in CH_3CN/t-BuOH 1:1 v/v) or D149 (0.3 mM in CH_3CN/t-BuOH 1:1 v/v) dye solutions at different immersion times. The counter electrodes were prepared to sputtered thin Pt-layers onto FTO substrates in a JEOL auto fine coater (JFC-1600). To prepare DSSCs, sensitized films and counter electrodes were sealed with a piece of Surlyn on a hot plate at 120 ºC and filling the space between both electrodes with an electrolyte solution.

Current-potential curves were measured using a solar simulator (100 mW cm^{-2} AM1.5G, Yamashita denso) and a Keithley 2400 source meter unit. The active area of the cells was delimitated with a 3 mm x 3 mm shadow mask. Incident photon to current conversion efficiency (IPCE) was measured with a Bunko keiki SM-25A monochromator-light source and a digital multimeter ADVANTEST AD7461A.

The absorbance spectra of the dyes in solution and adsorbed on films was measured using a spectrometer SEC2000-UV/VIS or an ocean optics miniature spectrometer respectively.

Stepped light-induced measurements of photocurrent and voltage (SLIM-PCV) and charge extraction were performed with a 635 nm diode laser as the light source, and a digital multimeter ADCMT 7461A to record the corresponding current/voltage transients. In the charge extraction measurement, the open circuit/short circuit sequence was applied for a potentiostat/galvanostat HOKUTO DENKO HBF500.

Cyclic voltammetry, for dye and electrolyte solutions as well as for dyed films used as working electrodes, was carried out using an electrochemical analyzer ALS/HACH intruments-1205B, a $Ag/AgNO_3$ (0.01 M) reference electrode, and (depending of the system) Pt as working and counter electrodes.

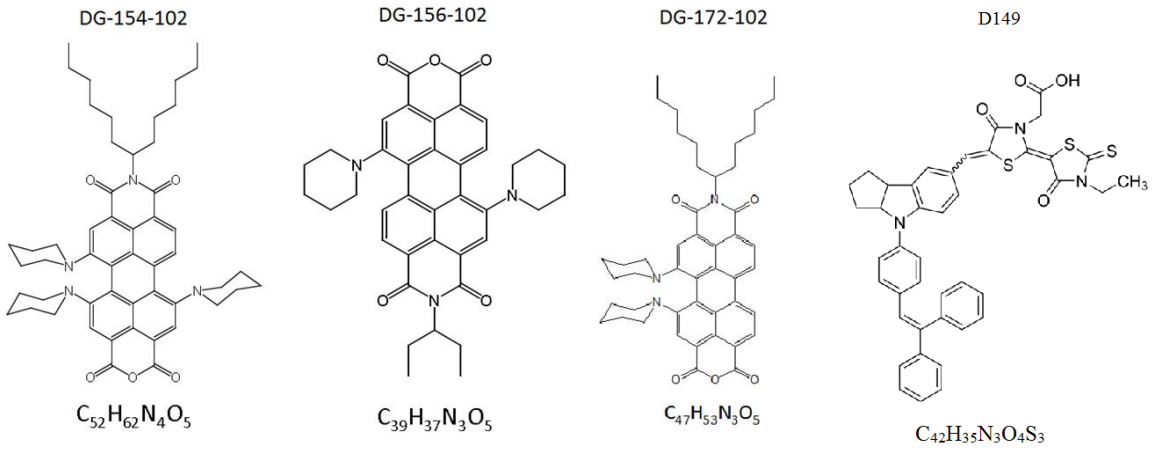

Figure 33. Chemical structures of dyes used.

7.2 Electrochemical and optical characterization of dyes and redox couples.

Cyclic voltammetry was used to determine the electrochemical properties and behavior of the dyes when in solution and adsorbed onto mesoporous ZnO and TiO_2 films. Dye solutions containing 0.3 mM Dye + 0.1 M tetrabutylammonium perchlorate in acetonitrile were analyzed in a classical three-electrode electrochemical cell in where the working and counter electrode were Pt, and a $Ag/AgNO_3$ (0.01 M) electrode calibrated versus ferrocene was employed as reference.

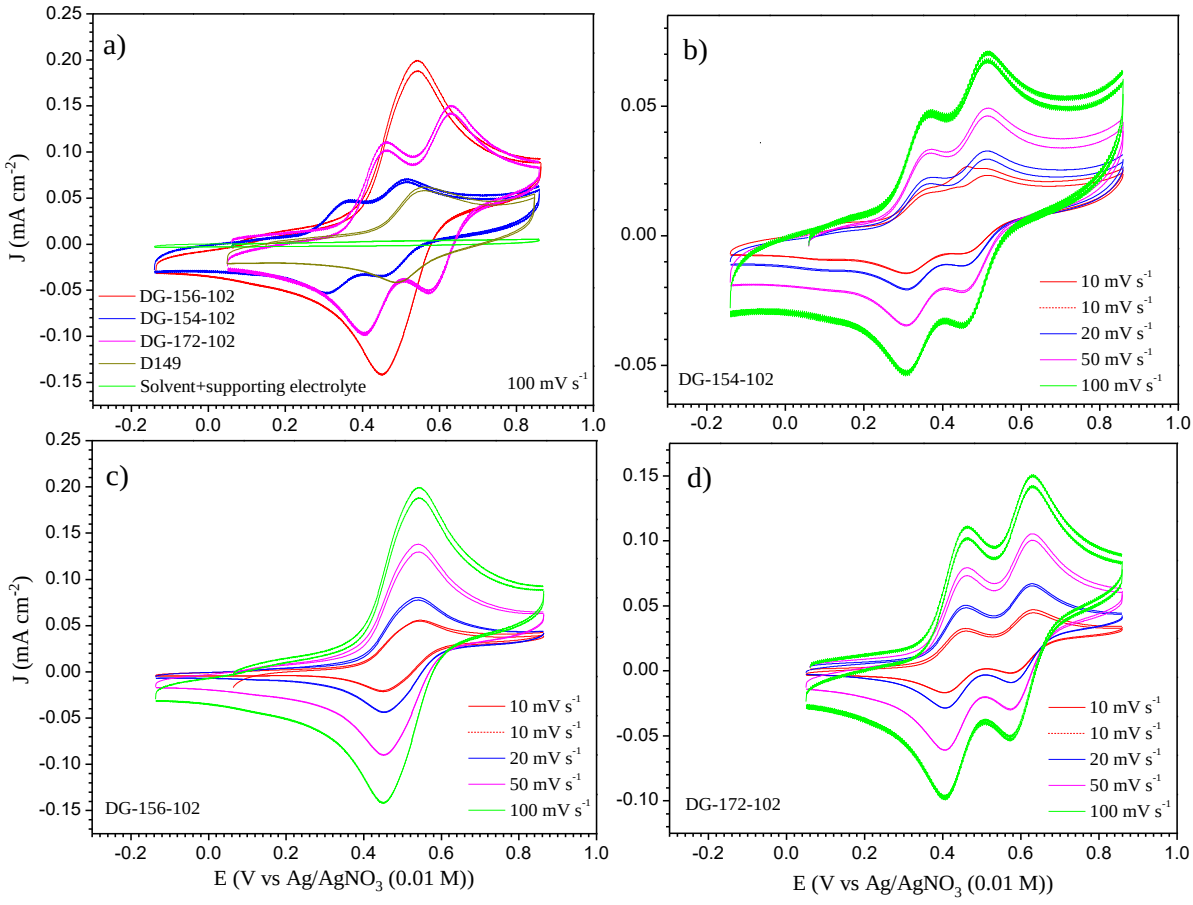

Figure 34.- Cyclic voltammograms for solutions 0.3 mM Dye + 0.1 M tetrabutylammonium perchlorate in acetonitrile at different scan rates and 25 ºC.

Figure 34a compares the voltammograms recorded for the perylenes dyes as well as for the indoline D149 dye, which has been chosen as reference, at a scan rate of 100 mV s^{-1}; In addition, cyclic voltammetries were performed at different scan rates (Fig. 34b, 34c and 34d) in where no dependence of the Ep (anodic or cathodic) with the scan rate used was observed, characteristic for fast redox couples only limited by mass transport. The DG-154-102 and DG-172-102 dyes showed two oxidation waves associated with the formation of the $D^{0/1+}$ and $D^{1+/2+}$ redox couples, a ΔEp of 52-60 mV for those redox reactions clearly indicates their high reversibility. A different behavior was observed for DG-156-102, which shows one oxidation wave with a ΔEp of 89 mV suggesting quasi-reversible electron transfer processes. In this figure also can be observed that DG-154-102 presents the most negative redox potential for the first oxidation reaction; this result is in good agreement with the molecule design in where piperidine units have been incorporated in the perylene core to improve the electron donating properties of the molecule, since the DG-154-102 has the largest number of such units, electrons can be detached from the molecule more easily; it is interesting to note that both DG-156-102 and DG-172-102 have two piperidine units but a different number of oxidation waves (and a different Ep^a for the first oxidation reaction), the reason seems to be related with the position of these units which may favor or suppress the loss of a second electron as in the case of DG-156-102. The D149 dye showed only one oxidation wave, with a difference of 70 mV between peaks and a redox potential very similar to the observed for the DG-156-102 dye. For fast electrochemical systems, the redox potential (E*) can be estimated from the half wave potential ($E^{1/2}= (Ep^a+ Ep^c)/2$) for the first oxidation reaction in the voltammograms, which is a good approximation of the HOMO level of the dye. The results are summarized in table 6.

Table 6. Redox potentials and HOMO levels for the dyes in solution.

Dye	**E* $_{(0/1+)}$ (V vs NHE)**	**E*$_{(1+/2+)}$ (V vs NHE)**	**HOMO (eV)[a]**
DG-154-102	0.873	1.021	-5.373
DG-156-102	1.037		-5.537
DG-172-102	0.9715	1.14	-5.471
D149	1.065		-5.56[b]

[a] Calculated through the following expression : $E_{HOMO}(eV) = -[E^* (V \text{ vs NHE}) + 4.5]$

[b] A HOMO level at -5.49 eV has been reported in reference [61].

After adsorption either on ZnO or TiO_2 (fig. A6), the perylene dyes showed a change in their HOMO level to more negative values due to a strong interaction of the non protonated carboxylic groups which result from the rupture of the anhydride ring initially present in the molecules with the semiconductor, while on the other hand a slight shift to more positive potentials was observed for the D149 dye (table 7).

Table 7.- Redox potentials and HOMO levels calculated for the dyes adsorbed on porous semiconducting films used as working electrodes in a three electrode electrochemical cell.

TiO_2		
Dye	**E* $_{(0/1+)}$ (V vs NHE)**	**HOMO (eV)**
DG-154-102	0.677	-5.17
DG-156-102	0.865	-5.36
DG-172-102	0.728	-5.22
D149	1.14	-5.64
ZnO		
Dye	**E* $_{(0/1+)}$ (V vs NHE)**	**HOMO (eV)**
DG-154-102	0.685	-5.18
DG-156-102	0.836	-5.33
DG-172-102	0.783	-5.28
D149	1.118	-5.61

UV-Vis spectroscopy was employed to determine the optical features of the dyes in acetonitrile/t-butyl alcohol based solutions and absorbed in semiconducting films, the absorbance spectra are shown in figure 35. For the perylene dyes absorption bands were observed between 400 to 800 nm as well as systematic differences related with their chemical structures such as the number and positions of the piperidine units that have been incorporated in the perylene chromophore. The DG-154-102 and DG-156-102 dyes showed a similar absorption onset ≈779-774 nm while DG-172-102 starts to absorb at 751 nm. As the absorption onset can be approximate to the band gap of the molecular absorber, we can estimate ≈1.6 eV for DG-154-102 and DG-156-102 and 1.65 eV for the DG-172-102 dye. The change of the absorbance with the dye concentration was also measured and the molar extinction coefficient (ε) calculated for the most intense absorption bands as can be seen in Table 8.

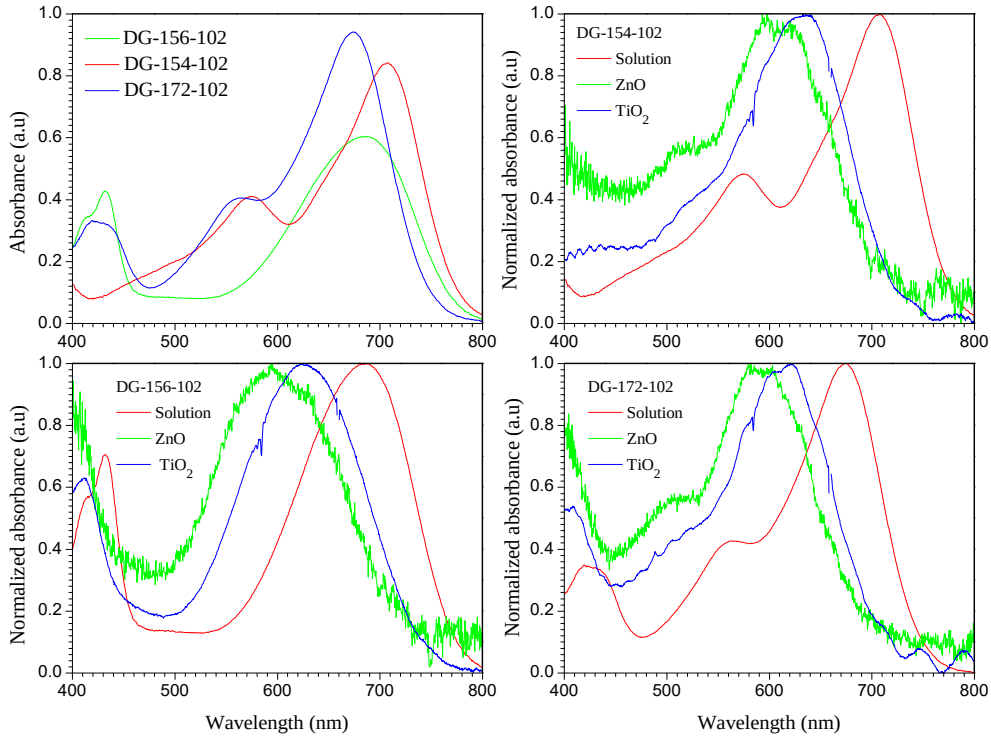

Figure 35.- Absorption spectra for the perylene dyes in solution and adsorbed onto ZnO and TiO_2 porous films.

All perylene dyes showed an hypsochromic shift in their absorption onset when adsorbed on semi conducting films, attributed to the rupture of the anhydride group which leads to the dye anchoring on the particles surface[62][63]. Edvinsson et al. have related this blue shift of the absorption onset with the intramolecular charge transfer (ICT) character toward the open anhydrous group; the wider the difference between the absorption onset of the dye in solution and onto the film the greater the ICT character in the molecule which can affect the charge transfer yield from the dye excited state (D*) to the semiconductor. Following this argument, the DG -154-102 dye shows the highest ICT character (with a difference of 74 to 49 nm in absorption onset in ZnO and TiO_2 respectively) while the DG-156-102 and the DG-

172-102 dyes presented similar ones (55 to 32 and 49 to 39 nm respectively). Clearly, the interaction of the dyes with the semiconductor changes their electrochemical and optical properties and, as consequence, the position of their HOMO and excited state levels, which can differ from the values observed when in solution.

Table 8.- Molar extinction coefficients for the main absorption bands and absorption onsets measured for the perylene dyes in solution and adsorbed on ZnO and TiO_2 films. The absorption onsets were calculated graphically as shown in figure A7.

Dye	λ (nm)	ε (10^4 M^{-1} cm^{-1})	λ^{Sol}_{onset} (nm)	λ^{ZnO}_{onset} (nm)	$\lambda^{TiO_2}_{onset}$ (nm)
DG-154-102	575	1.27	779	705	730
	707	2.61			
DG-156-102	415	1.06	774	719	742
	432	1.3			
	688	1.83			
DG-172-102	419	1	751	702	712
	434	0.95			
	562	1.21			
	674	2.8			

Two electrolyte solutions were tested to see their effect on the cell performance by varying the concentration of the well-known CB potential-determining additives (Li^+ ions and TBP molecules) in the solution. Their compositions are listed as follows:

- 42: 0.6 M BmImI, 0.05 M I_2, 0.1 M LiI, 0.5 M TBP in CH_3CN.

- E3: 0.05 M I_2, 0.7 M LiI in CH_3CN.

Figure 36 shows I-V curves for cyclic voltammetry experiments at a very slow scan rate of 0.5 mV s^{-1}; the average potential where the current density is zero corresponds to the redox potential of the electrolyte solution (E*). The results are presented in table 9.

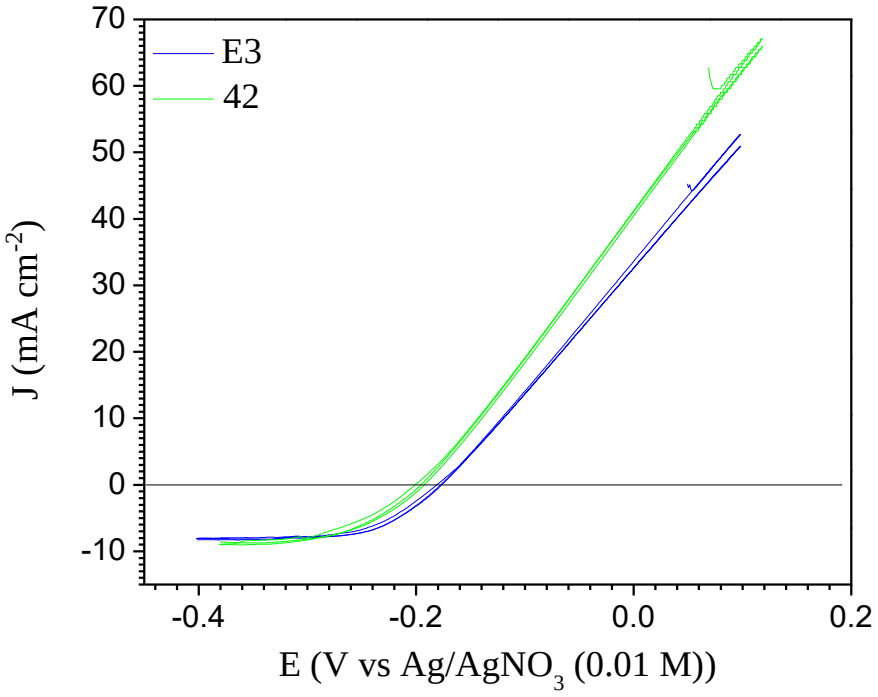

Figure 36.- Cyclic voltammograms measured to the electrolyte solution used in the solar devices on Pt working and counter electrodes at 0.5 mV s^{-1} and 25 ºC.

Table 9. Redox potential for the electrolyte solutions used in the solar devices determined by electrochemical methods.

Electrolyte	**E* (V vs Ag/Ag^{+})**	**E* (V vs NHE)**
42	-0.197	0.343
E3	-0.18	0.36

7.3 Characterization of solar cells.

Dye-sensitized solar cells were elaborated with ZnO films deposited onto FTO and sensitized in acetonitrile/t-butyl alcohol solutions of the perylene based dyes for 0.5, 1, 6, 12 and 24 h (before cell assembly with the counter electrode as described in section 6.1) and an I^-/I_3^- based electrolyte solution (electrolyte 42).

First, the effect of the sensitization time on the cell performance was studied in order to observe the presence of dye aggregation, either by formation of dye agglomerates or Zn^{2+}-dye complexes due to selective dissolution of the ZnO particles. Both types of aggregation represent a serious limiting factor in the efficiency of photovoltaic devices, especially due to their negative effect on the electron transfer processes that take place at the sensitizer-semiconductor interface.

Figure 37 shows current-potential curves as a function of the immersion time of the ZnO electrodes in the dye solutions, where a similar trend was observed for the three DG dyes. A slight increase of the J_{sc} was observed from 0.5 up to 6.0 h of sensitization followed by quite similar values at longer times, suggesting that no more dye loading takes place on the photoanode surface. The fact that no decrease of the Jsc is observed at longer times points to the absence of dye-dye aggregates or Zn^{2+}-dye complexes in the mesoporous film, which usually leads to a decrease of the injection efficiency. Several possible causes for the low injection efficiency include an unsuitable position of the aggregates-excited state level, poor orbital coupling between the dye molecule and the semiconductor, inter-molecular quenching, among others. This result can be rationalized in two ways: In the design of perylene-based sensitizers, several approaches have been tried in order to overcome the

inconvenient interaction of the dye molecules when in solution, such as the inclusion of alkyl chains with free rotation capacities in the imide group among others [64][65]; however, in our case, the lack of aggregation seems to be more related with the piperidine substituents in the perylene core than with the length of the hydrocarbon chains used. Then, the piperidine units not only increase the electron donating properties of the perylene chromophore, but also avoid the multi-stacking of dye-dye agglomerates on the semiconductor surface. Second, the anchoring of the dye molecule through the rupture of the anhydride ring when in contact with the semiconductor surface results in two non-protonated carboxylic groups, hence, the absence of protons (H^+) released during the film sensitization avoids the dissolution of the ZnO nanoparticles (as has been reported for dyes like N3 and N719 among others), which usually leads to Zn^{2+}-dye complexes blocking the pores in the semiconductor film. From this analysis, it can be concluded that the maximum dye up taking is reached at 6 h.

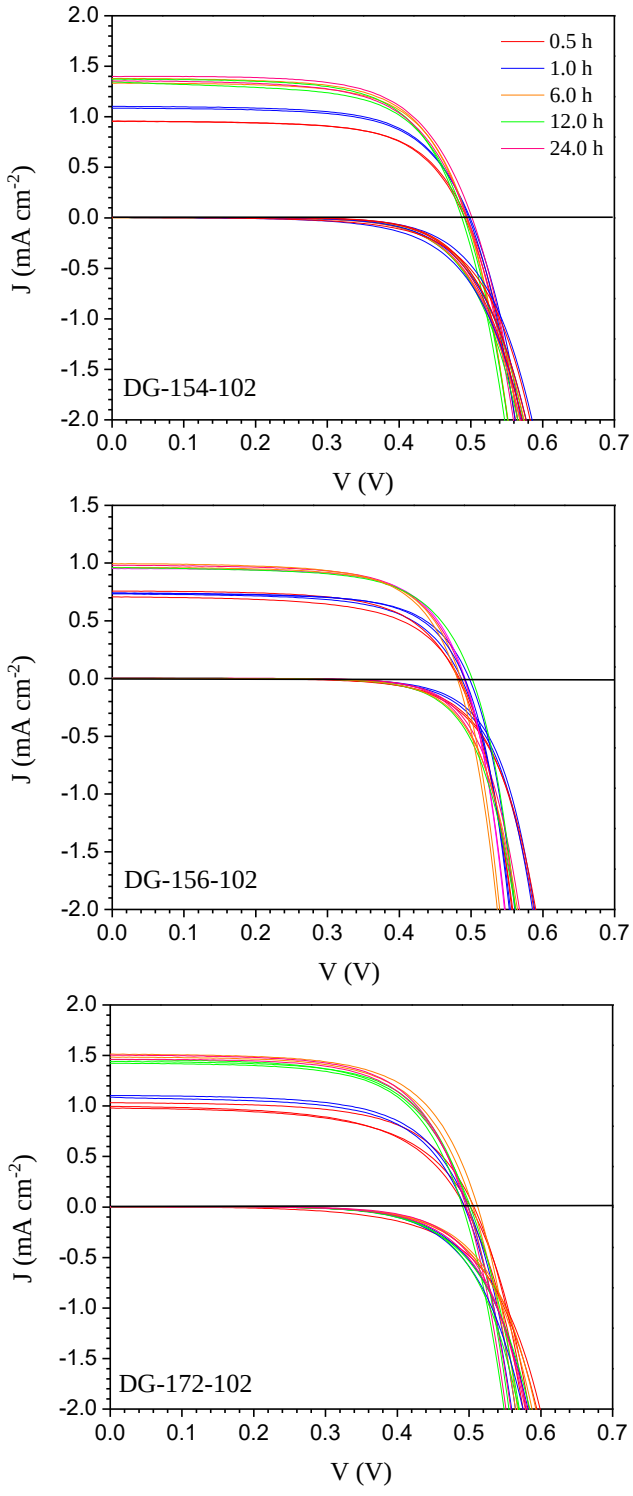

Figure 37. I-V curves for DSSCs elaborated with the perylene dyes as a function of sensitization time.

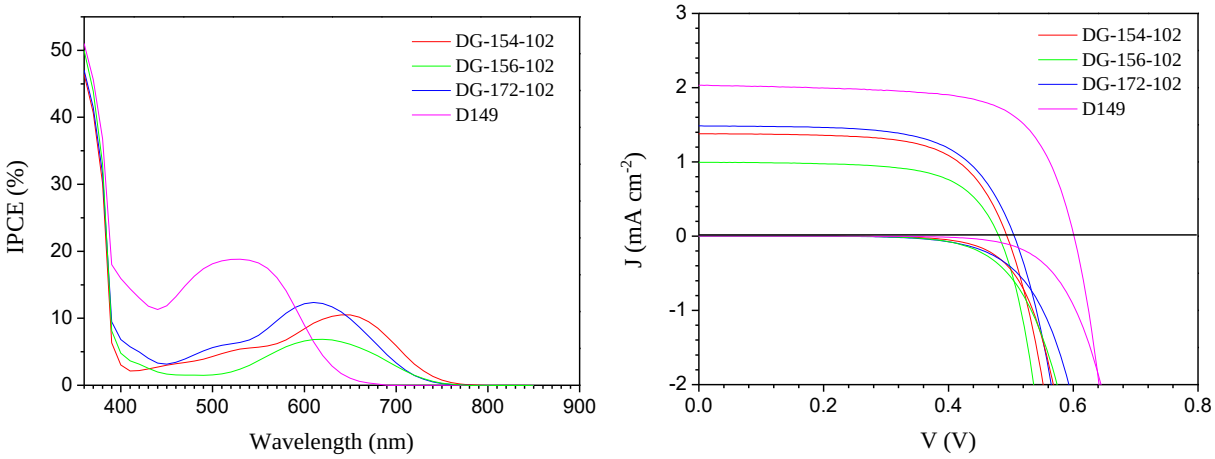

Figure 38. IPCE and I-V curves for perylene and D149 based DSSC at 6 h of sensitization time.

Figure 38 shows IPCE and I-V curves for perylene and D149 based solar devices elaborated with the optimum sensitization time. Table 10 summarize the parameters evaluated for curves in Figure 38. A similar V_{oc} was observed for the DG-154-102 and DG-156-102 cells, and slightly higher for the DG-172-102 cells (≈ 20 mV more), however the dark current measured, which can give us information about the transfer rate of the electrons injected in the working electrode with the oxidized species in the electrolyte solution, was quite similar suggesting a different reason for this gain in voltage. For the perylene dyes, the DG-172-102 cells showed the highest efficiency not only for the gain on V_{oc} commented above, but also for the better IPCE (λ) features especially in the range of 380-650 nm; in the case of the DG-154-102 and DG-156-102 cells the efficiency was mainly determined by J_{sc}, where DG-156-102 showed the lowest IPCE (λ) values. On the other hand, the cells made with the D149 dye showed, on average, almost twice the efficiency compared to those obtained with the perylene dyes, related to a higher V_{oc} (accompanied by a lower dark current density) and J_{sc} (due to the larger values of IPCE (λ) in the range of 390-570 nm). The higher V_{oc} of the D149

cells could be originated by a decreased recombination rate of the electrons injected in the semiconductor with the acceptors in the electrolyte solution as well as by a shift of the conduction band edge to negative potentials due to a strong interaction of the dye with the semiconductor; it is not possible to differentiate between both effects only with the current-potential curves; hence, more information about the semiconductor/dye/electrolyte interface is needed.

Table 10. Photovoltaic parameter measured to the DSSCs presented in Figure 38

Dye	**Time (h)**	**Voc (V)**	**Jsc(mA/cm^2)**	**FF**	**η (%)**
DG-156-102	6	0.48± 0.003	0.96± 0.60	0.66±0.01	0.31± 0.02
DG-154-102	6	0.49± 0.01	1.32± 0.07	0.65± 0.01	0.42± 0.03
DG-172-102	6	0.51± 0.01	1.52± 0.08	0.64± 0.01	0.50± 0.04
D149	6	0.57± 0.02	2.03± 0.25	0.68±0.01	0.79± 0.10

The diffusion coefficient and electron lifetime (Fig. 39 and 40) was determined by the measurement of stepped light induced photocurrent and photovoltage transients (fig. 7 presents a set of transients measured to cells elaborated for this study), while the charge extraction method was used to relate the open circuit potential with the electron density accumulated in the semiconductor. A similar dependence of D_n as function of J_{SC} (fig. 39a) was observed for the perylene and D149 solar cells, which implies similar electron transport features through the semiconductor film as the Fermi level changes with the light intensity,

apparently independent of the nature of the dye adsorbed, an interesting finding taking into account the different chemical nature between the perylene and the indoline dyes. Possibly this result is more related with the ZnO, since some studies have shown that standard dyes such as the ruthenium complex N719 can change under certain conditions the total amount of the charge trapping states in TiO_2 films and, as a consequence, modify its electron transport properties [66]. The position of the conduction band edge showed a different trend (fig 39b), where a shift to more negative values was found for the DG-172-102 dye (indicated for the much lower charge accumulated in the semiconductor at the same V_{oc}), possibly induced by the presence of a permanent dipole in the molecule due to its slightly asymmetrical structure (mainly for the position of the piperidine units).

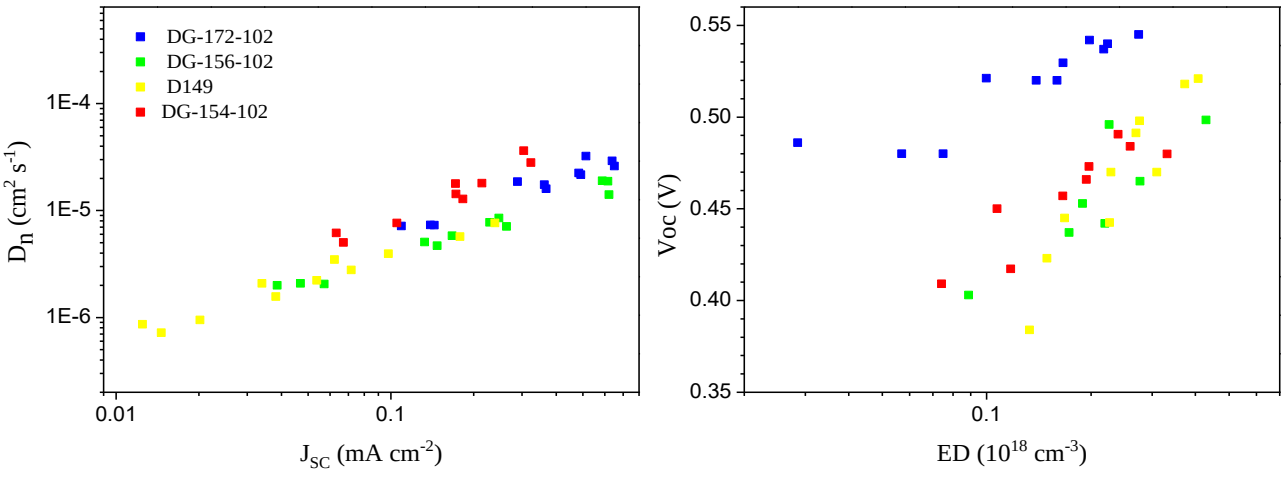

Figure 39. a) Diffusion coefficient (versus J_{sc}), and b) V_{oc} (versus electron density) for cells prepared at the same conditions as in Figure 36. The increase of the diffusion coefficient with the J_{SC} (due to an increase of the light intensity) is in agreement with the assumption of an exponential distribution of trap states below the conduction band.

Figure 40 shows the electron lifetime extracted from the SLIM voltage transients as a function of the electron density measured in the semiconductor. A similar lifetime was observed for the DG-154-102 and DG-156-102 cells which explains their similar V_{oc} too, while the D149 cells showed the highest values as well as the highest V_{oc} possibly due to a better blocking effect of the electrode surface related with its chemical structure. The DG-172-102 cells showed a slightly lower lifetime but at the same time the highest V_{oc} for the perylene dyes. The shift of the conduction band edge to more negative values in theory could allow an increase of ≈80 mV the V_{oc} for the same electron density, however, this shift also increases the free energy for electron transfer between the semiconductor and the acceptors in the electrolyte solution or to the dye cations, leading to only a 20 mV increase in V_{oc}.

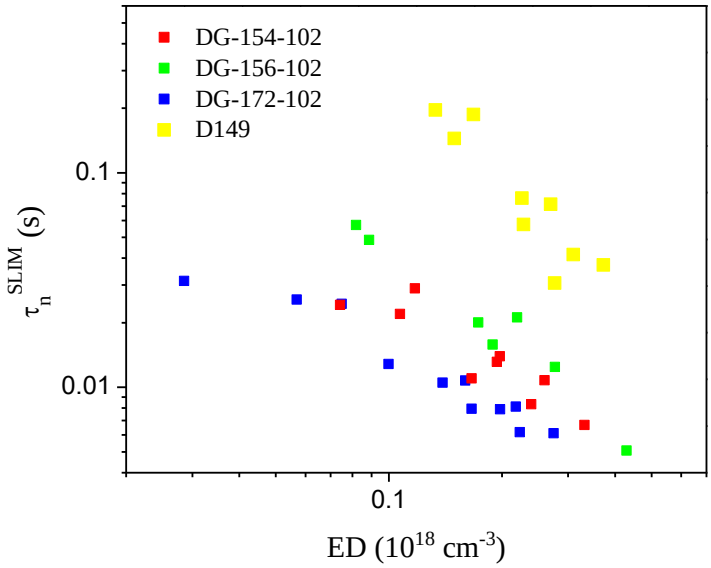

Figure 40. Electron lifetime versus electron density (ED) for DSSCs prepared at same conditions that Fig. 36. The decrease of the electron lifetime with the ED (due to an increase of the light intensity) is in agreement with the assumption of an exponential distribution of trap states below the conduction band.

The modest efficiencies observed in these devices could be originated by different factors, some of them dependent on the semiconductor nature. In order to identify these efficiency-limiting factors, TiO_2-based solar cells were prepared and characterized at the same conditions (similar film thickness and sensitization time). As defined above, if electron injection and collection efficiency are high, the J_{SC} will depend basically on the amount of dye loaded on the mesoporous film. Figure 41 shows the absorbance spectra of ZnO and TiO_2 mesoporous films sensitized at 6 h in the dye solutions previously described.

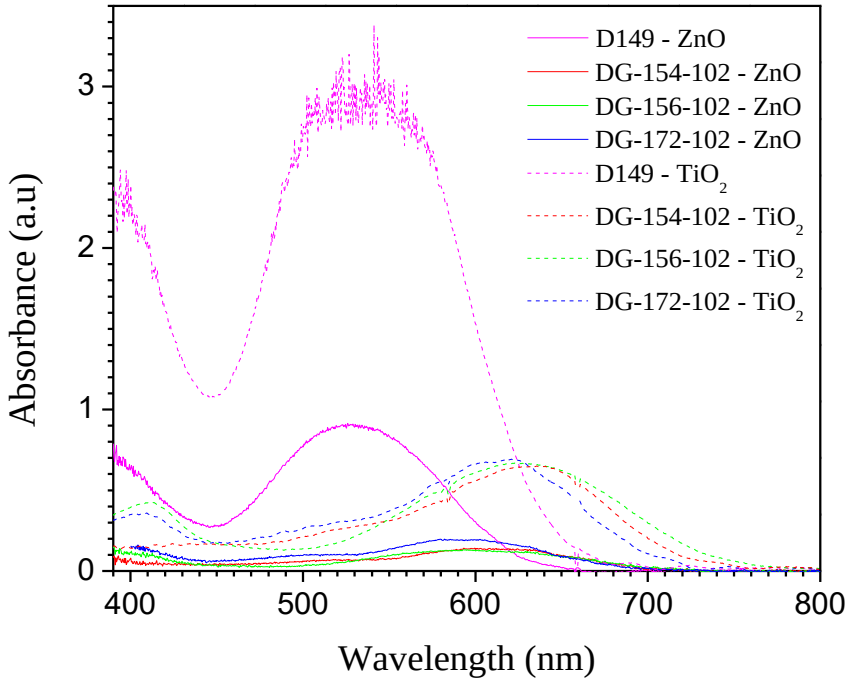

Figure 41.- Absorbance spectra for dyed ZnO and TiO_2 films.

As can be seen, the TiO_2 films showed high absorbance values due to a higher amount of dye loaded when comparing with the ZnO films. A correlation between the surface area of the film and the dye loaded is well known, and the former with a clear dependence on the particle

size and geometry, surface roughness and film porosity. SEM images taken of these films revealed some morphological differences, where small and elongated particles (Fig. 42a) were observed in the porous TiO_2 array, while larger granular particles (between 20-70 nm) as well as a higher porosity was found for the ZnO films (Fig. 42b). Unfortunately, the overall effect of these specific differences on the surface area cannot be properly determined only with SEM images.

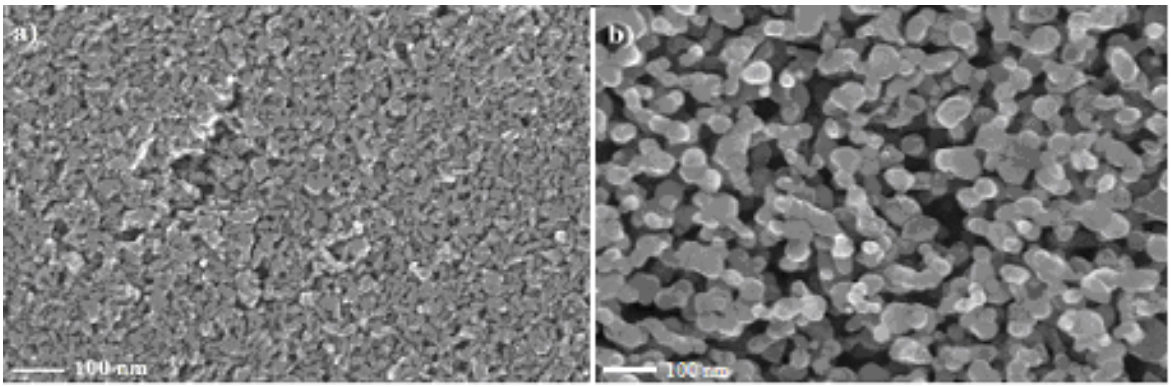

Figure 42.- SEM images taken of: a) TiO_2 and b) ZnO films deposited onto FTO and after sintering at 450 and 550 ºC respectively.

Lizama et al. [67] have shown a dependence of the surface chemistry of ZnO-nanoparticles on the cell performance, where the amount of dye loaded was mainly dominated by the strong presence of non-polar surfaces (instead of the measured surface area in the film) that can act simultaneously as Lewis acid and base sites, promoting a more efficient deprotonation/rupture of the anchoring groups and subsequent chemisorption of the molecules on the particles; hence, the chemical and crystallographic properties of each material have to be taken in to account in this analysis, which is beyond the scope of this work.

A difference in the light harvesting efficiency (Φ_{lh}), calculated from the total absorbance of the dyed films (eq. 7.1), and the IPCE measured to these cells (Fig. 43a and 43b) points out a low internal quantum efficiency.

$$LHE\ (\lambda) = (1-10^{-Abs(\lambda)}) * 100 \qquad (7.1)$$

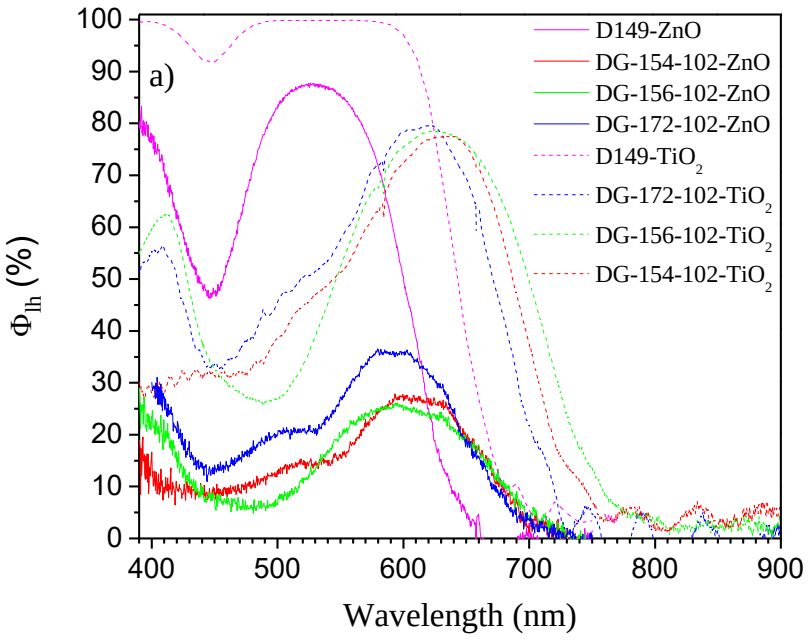

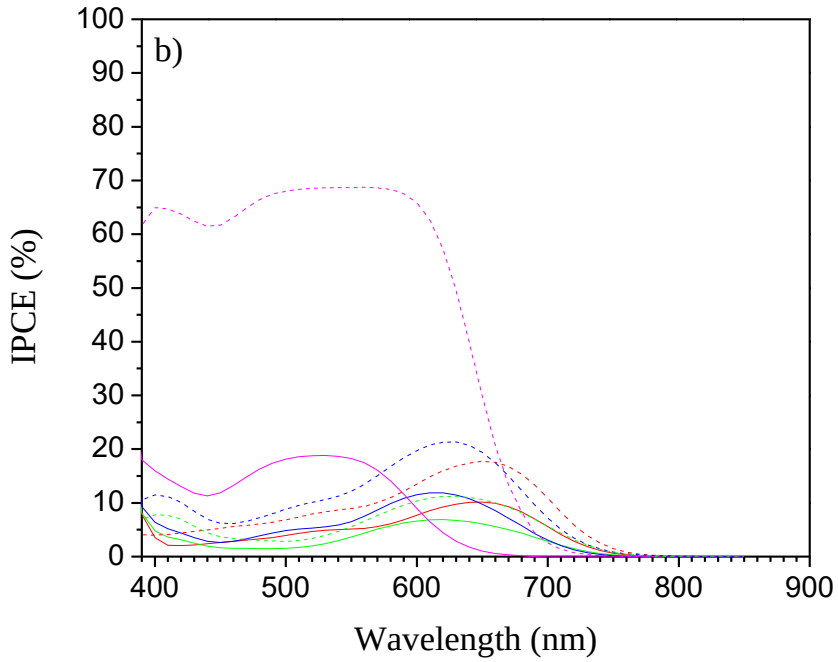

Figure 43.- Light harvesting efficiency (Φ_{lh}) and IPCE spectra for the perylene and D149 dye on ZnO and TiO_2 films.

The absorbed photon to current conversion efficiency (APCE), also called the internal quantum efficiency (IQE), provides information about the injection and collection efficiency (eq. 7.2); then, through the systematic change of some of the cell components it is possible to figure out the limiting factors involved.

$$APCE = IPCE(\lambda) / \Phi_{lh}(\lambda) = \Phi_{col} * \Phi_{inj} \qquad (7.2)$$

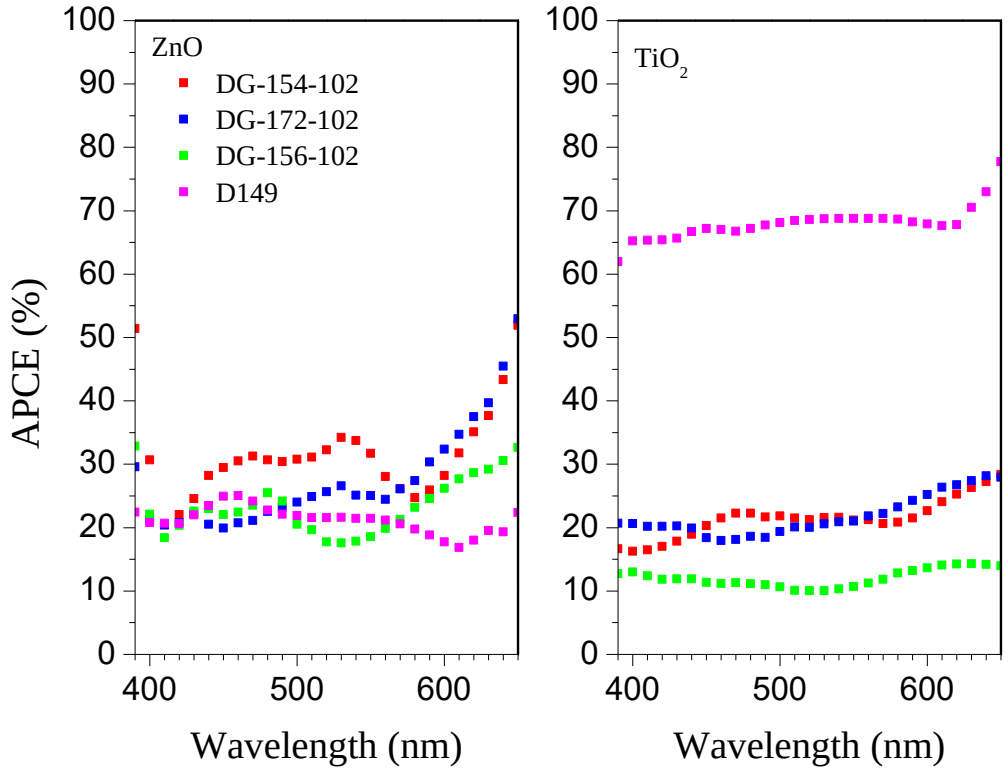

Figure 44.- APCE spectra calculated from the Φ_{lh} and IPCE in fig. 43.

A qualitative analysis of Figure 44 shows low APCE values for all the ZnO cells, and similar ones between the perylene based ZnO and TiO_2 cells, while the D149-TiO_2 cells showed the highest values. A previous report [68] emphasizes that the low performance of D149-ZnO cells is related with electron injection issues (due a lower density of acceptor states in the material or the presence of bound charge-transfer pairs which recombine faster than the full charge separation), whereas the electron collection and dye regeneration remained similar for both semiconductors; hence, while the D149 cells showed a material dependent IQE, the performance of the perylene cells results more complicated to be explained. In the rest of this work, DG-154-102 was chosen as the representative dye of the DG series and used to investigate the performance limiting factors in these molecular absorbers.

The electron collection efficiency depends on the film thickness (≈4 μm for TiO_2 and ≈3.4 μm for ZnO in our devices) and the electron diffusion length (L_n) defined as the average distance that electrons travel before recombination; high collection efficiencies are found when the film thickness is much less than the electron diffusion length. Figure 45 shows the change on IPCE as function of the film thickness, where an increase in this latter raise the IPCE due to an increase of the absorbance of the dyed films, pointing out a value of L_n that is larger than 7 μm in both semiconductors; however, it should to be noted that it is not possible to quantify Φ_{coll} based only on this result.

Upon light absorption the electron distribution in the excited dye molecule is displaced toward the anchoring group near to the dye/semiconductor interface which leads to the electron injection if the excited state level-CB energy difference is good enough to overcome the activation energy for this electron transfer process.

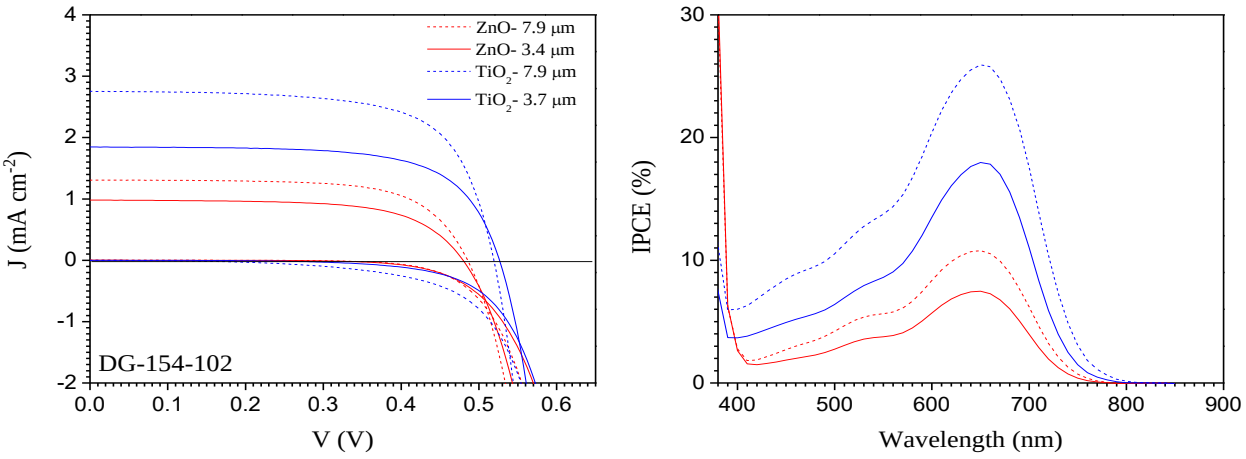

Figure 45.- I-V curves and IPCE spectra for DSSCs prepared with the DG-154-102 dye and ZnO/TiO_2 films with different thickness.

According to the Marcus theory for electron transfer, as the excited state level-CB energy difference increases the rate constant for this process also increases. For the invariant position of the excited state level of the dye, such energy difference can be tuned through the specific interaction of some additives in the electrolyte solution with the semiconductor, as the well known upward shift of the CB in presence of the TBP molecules or the downward shift induced by the Li^+ cations. An electrolyte solution with an increased concentration of LiI, in the absence of TBP, was used (E3), in order to determine the presence of electron injection issues due to an unfavorable position of the excited state level of the dye with respect to the metal oxide conduction band. Figure 46 shows IPCE and I-V curves for ZnO and TiO_2 solar devices elaborated with the E3 electrolyte solution.

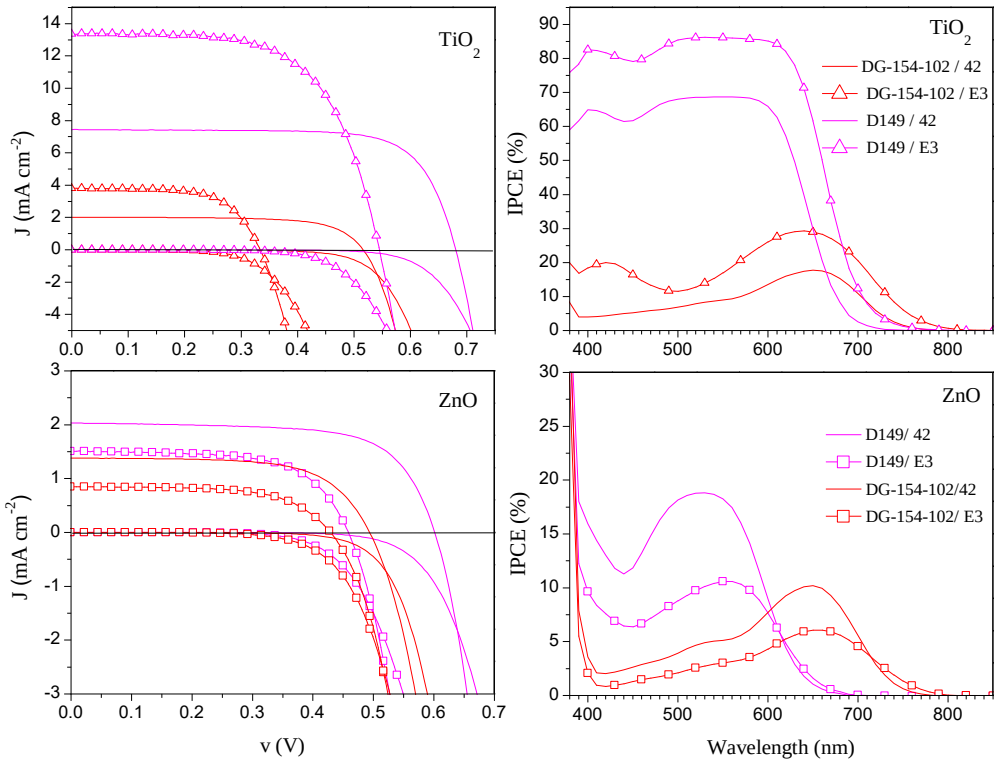

Figure 46.- I-V curves and IPCE spectra for TiO_2 and ZnO based solar cells prepared with the electrolyte solution ·42 (0.6 M BmImI, 0.05 M I_2, 0.1 M LiI, 0.5 M TBP in CH_3CN) and E3 (0.05 M I_2, 0.7 M LiI in CH_3CN).

As expected, the increase in the concentration of Li^+ cations in the electrolyte solution leads to a diminution of the open circuit potential of the solar cell devices mainly due to a shift of the metal oxide conduction band to more positive values (Fig. 47a), and not because of a decrease of the electron lifetime (for almost all devices) as shown in Figure 47b; in fact an increase of the latter accompanied the downward shift of the conduction band in the TiO_2 cells. Figure 47a also shows that the effect of E3 was less pronounced in the ZnO-based devices with only ≈68 mV of band shift (after correction for the difference in redox potential)

while more than 200 mV was observed for the TiO_2 cells; this is in good agreement with the observations of Idígoras et al., who attribute it to the low dielectric constant for ZnO that complicates the formation of the surface dipoles that induce shifts in the band position [69].

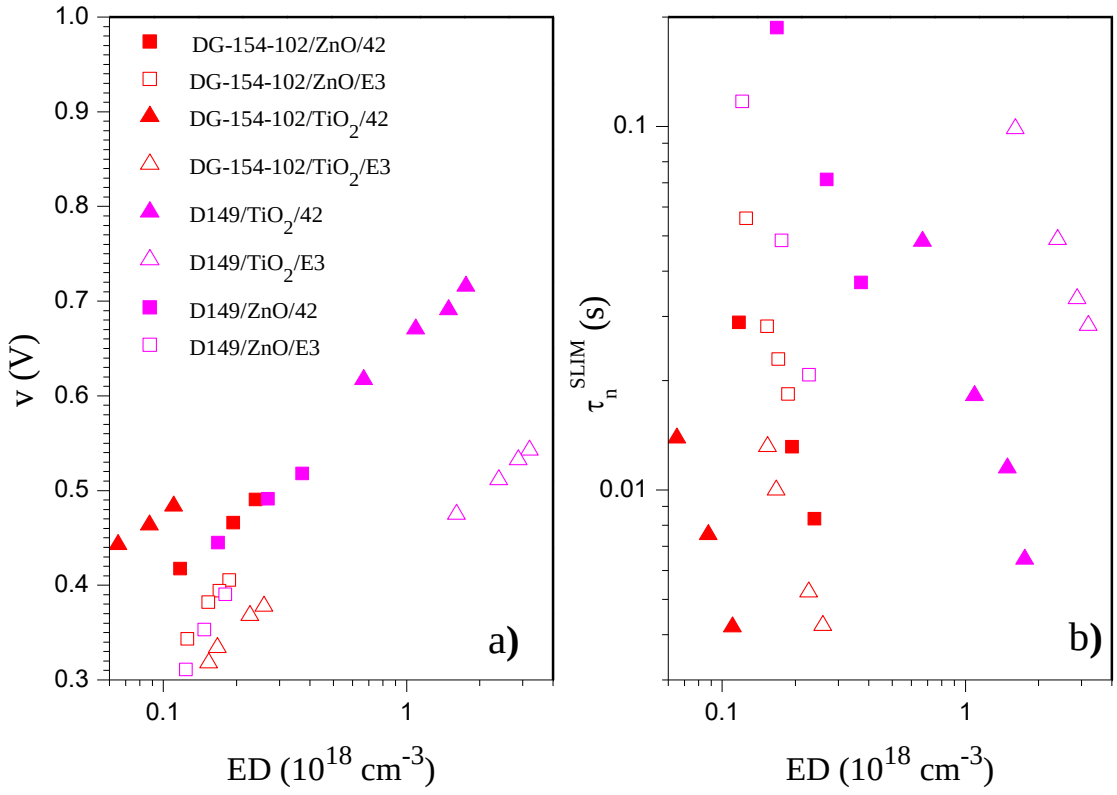

Figure 47.- a) V_{oc} and b) electron lifetime as function of the electron density in the semiconductor for TiO_2/DG-154-102/electrolyte 42 (solid red triangles), TiO_2/D149/electrolyte 42 (solid pink triangles), ZnO/DG-154-102/electrolyte E3 (hollow red squares) and ZnO/D149/electrolyte E3 (hollow pink squares). The porosity of the films has not been taken into account in the calculation of the electron density.

For the TiO_2 cells an increase of the J_{sc} was observed with the downward shift of the CB due to the increase of the excited state level-CB energy difference that makes the electronic transfer a more favorable thermodynamic process. Different to the high IPCE values observed for the D149 cells, the DG-154-102 cells only reached a 29% of $IPCE_{max}$ after a similar band shift, suggesting poor electron injection due to the inconvenient position of the dye excited level (relative to the CB) as one of the reasons for the low IQE previously and still observed.

The use of the E3 electrolyte in the ZnO cells lead to a loss in J_{sc} and IPCE of the solar devices, behavior that was indifferently observed for both dyes. When working with different semiconductors, electron injection also depends on the density of accepting states (DOS) in the semiconductor CB; hence, slow electron injection into the ZnO due to its lower DOS (reasoning in good agreement with the injection times experimentally determined for the ruthenium-N3 dye of 250 fs and 1.5 ps in TiO_2 and ZnO respectively [70]) has been suggested as the main reason of the low performance of ZnO solar cells. From the optical density spectra of the dyed films in Figure A8, a much lower amount of dye molecules per unit volume of porous ZnO can be observed compared to that for TiO_2 films. Together with the less compact arrangement of the ZnO particles observed in the SEM images, this suggests a lower surface coverage by the dye in the ZnO films, in other words, a less dense packing of the dye molecules on the particle surface. Due to the low surface coverage by the dye in the ZnO cells, the increase on the I^- and I_3^- concentrations at the electrode surface (as the decrease of τ_n in the D149 cells suggests), together with the slow electron injection process, mentioned above, may favor the reductive quenching of the excited dye molecules by I^- [24,71–73], or electron transfer from the excited state to the I_3^- ions, mechanisms that lead to a decrease in the Φ_{inj} from the dye excited state and, as a consequence, to a decrease of the J_{sc} in the cells.

Unfortunately, it is not possible to determine the predominant mechanism with the available results, hence, a more detailed study is needed.

The regeneration efficiency of the oxidized dye molecules after electron injection strongly depends on the driving force for this charge transfer process, proportional to the energy difference between the HOMO level and the redox potential of the electrolyte solution (E*), where 0.6 V or more, for the I^-/I_3^- redox couple, usually yields high efficiencies. After adsorption all the dyes showed changes in their HOMO level position when comparing with those measured in solution (to more negative potentials for the perylene dyes and slightly more positive for the D149 dye) as shown in table 11. Driving forces between 0.522 to 0.334 V were found for the perylene cells, values that do not allow us to rule out a poor dye regeneration as an efficiency limiting factor in these devices, especially for its great effect on Φ_{coll}.

Table 11.- Electrochemical features of the dyes in solution and adsorbed in porous semiconducting films.

	Solution	**TiO_2**	**ZnO**	**TiO_2**	**ZnO**
Dye	**HOMO (V vs NHE)**	**HOMO (V vs NHE)**	**HOMO (V vs NHE)**	**|E*-HOMO|**	**|E*-HOMO|**
DG-154-102	0.873	0.677	0.685	0.334	0.342
DG-156-102	1.037	0.865	0.836	0.522	0.493
DG-172-102	0.9715	0.728	0.783	0.385	0.44
D149	1.065	1.14	1.118	0.797	0.775

7.4 Conclusions

Metal free dyes based on perylene-monoanhydride-monoimides derivatives were used in the fabrication of ZnO-solar cells. The stability of the J_{sc} in function of the immersion time of the films in the sensitizing solution points out the absence of dye aggregation due to the formation of Zn^{2+}-dye complexes or multi-stacked dye-dye agglomerates on the semiconductor surface and in this way the excellent chemical compatibility of the anhydride ring (as anchoring group precursor) with the ZnO; for all the perylene dyes the maximum dye coverage was reached at approximately 6 h of sensitization. Despite their broad absorption spectra, electron injection and dye regeneration issues (especially for the appreciable shift of the HOMO level to less positive potentials upon adsorption) are the possible reasons for the low performance observed in the solar devices.

Different to the observations for the TiO_2 cells, the low surface coverage by dye, and the (well known) slow electron injection process in the ZnO-based devices lead to undesirable electron transfer reactions in the dye/electrolyte interface (observed indifferently in both the perylene and the indoline dye) for an increase on the concentration of either the I^- or I_3^- ions near to the electrode surface.

Our results point out the possibility to overcome these issues through a detailed study of the specific interactions of the additives with each semiconductor to the design of adequate electrolyte solutions, and the use of fast redox mediators less sensitive to small driving forces.

8. General conclusions

ZnO is an attractive alternative material for application in dye-sensitized solar cells (DSSCs), related to the wide range of morphologies that can be prepared at relatively low processing temperatures and the superior electrical properties as compared to TiO_2, which is currently the dominant material applied in DSSCs. However, there are several problems specifically related to the use of ZnO, that lead to the necessity to redesign all components of the solar cell. In this work, the materials aspects of ZnO-based dye-sensitized solar cells have been studied in detail, including the ZnO fabrication method and morphology, the dye and its anchoring group, and the redox couple in the electrolyte solution.

Mesoporous and nanostructured ZnO films have been prepared by electrodeposition, as well as by deposition via doctor blading using a paste of commercial ZnO nanoparticles, both onto an FTO substrate. Using electrodeposition, a dependence of the morphology and composition of the films obtained on the Zn^{2+} precursor used as well as the deposition conditions designed, was clearly observed. Semi-spherical ZnO particles were obtained from the $ZnCl_2$ bath with the addition of the water-soluble PVP40 polymer, a novel finding in these baths, where the selective adsorption of Cl^- ions tends to favor the growing of particles with more sharp geometries. Through the change in bath composition and deposition conditions used, a low-temperature crystalline ZnO precursor, simonkolleite, was obtained, opening the possibility to electrodeposit thin semiconducting films on flexible substrates based on conducting polymers for the construction of lightweight and portable photovoltaic devices. Both materials were used to prepare dye-sensitized solar cells, with results that emphasize the good quality and suitability of the films obtained for solar cell applications

One of the most important problems related with the use of ZnO is that the classical dyes used for TiO_2 are too acidic, resulting in partial dissolution of ZnO during the sensitization process. Hence, novel dyes need to be designed, and this is an important on-going research subject. It has been found that organic dyes with a single cyanoacrylic anchoring group are promising, however, multi-layer dye adsorption as well as ZnO surface stability remain an issue. In this work, we have compared a commercial dye, OD-8, that has not previously been used for ZnO-based DSSCs, and determined its promise. In addition, in collaboration with a synthetic group in Spain, we have designed a novel anhydride bonding moiety as a non-acidic anchoring group, and shown its promise for ZnO-based DSSCs. In particular, the anhydride anchoring group is shown to not degrade ZnO, in addition, the designed dyes do not show multi-layer adsorption, which is another undesirable dye aggregation process, that leads to lower injection efficiency.

As a constant in all the ZnO systems studied, low surface coverage by the dye was observed, which not only promotes efficient electron transfer at the semiconductor/electrolyte interface, which is an important recombination process, thus limiting the attainable open circuit potential and photocurrent in the cell due to a negative effect on the electron collection efficiency (as observed in the OD-8/$[Co(bpy)_3]^{2+/3+}$ solar cells), but also undesirable electron transfer reactions at the dye/electrolyte interface when increasing the concentration of the electron donor/acceptor species near to the electrode surface (behavior observed in the D149 and perylene based cells when the concentration of Li^+ was increased in the electrolyte solution). Thus, any strategy designed to improve the efficiency of ZnO-based DSSCs has to aim for a complete surface coverage with adsorbed dye, thus effectively passivation the main recombination process. This implies finding a sensitizer that is highly compatible with the

ZnO surface chemistry, in other words, dyes with high adsorption yields when in contact with the particle surface, but that do not contain or release chemical species that compromise the stability of the ZnO surface during this process.

Appendix

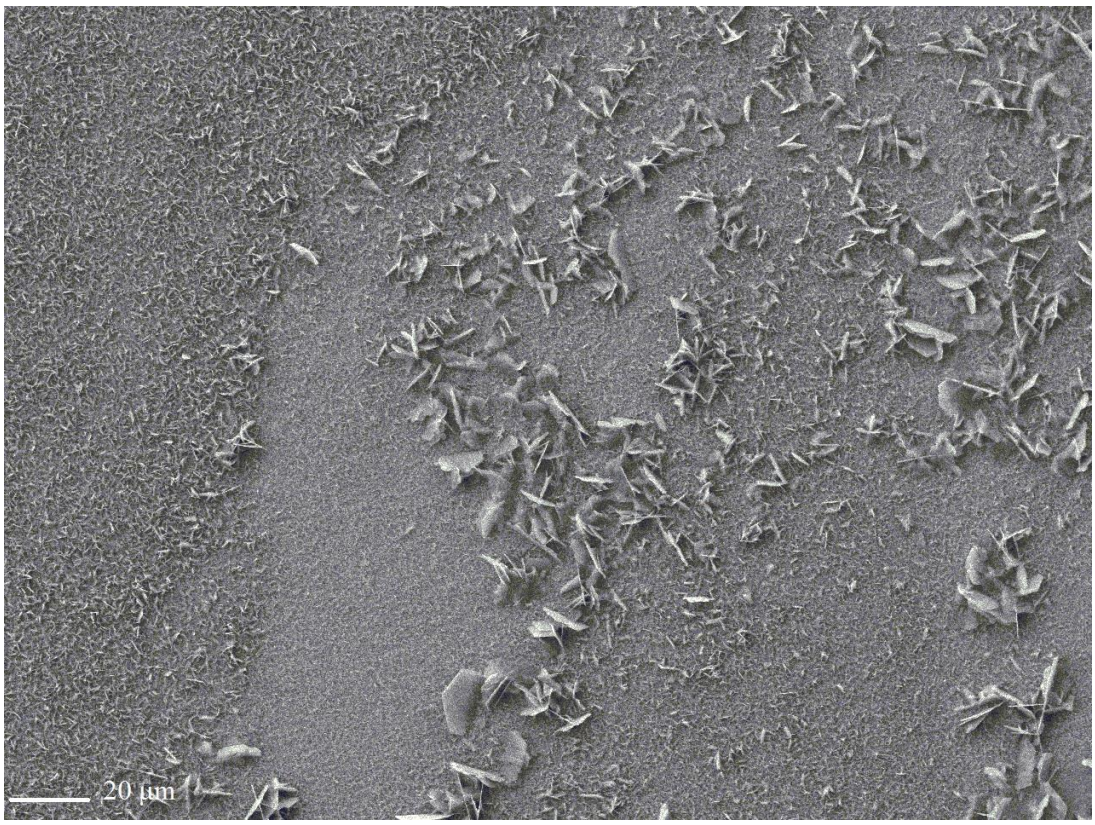

Figure A1.- SEM image for a Simonkolleite film electrodeposited from a 0.1 M $Zn(NO_3)_2 \bullet 6H_2O$, 0.1 M KCl aqueous solution at pH= 6.0, 70 °C and the procedure Z1.

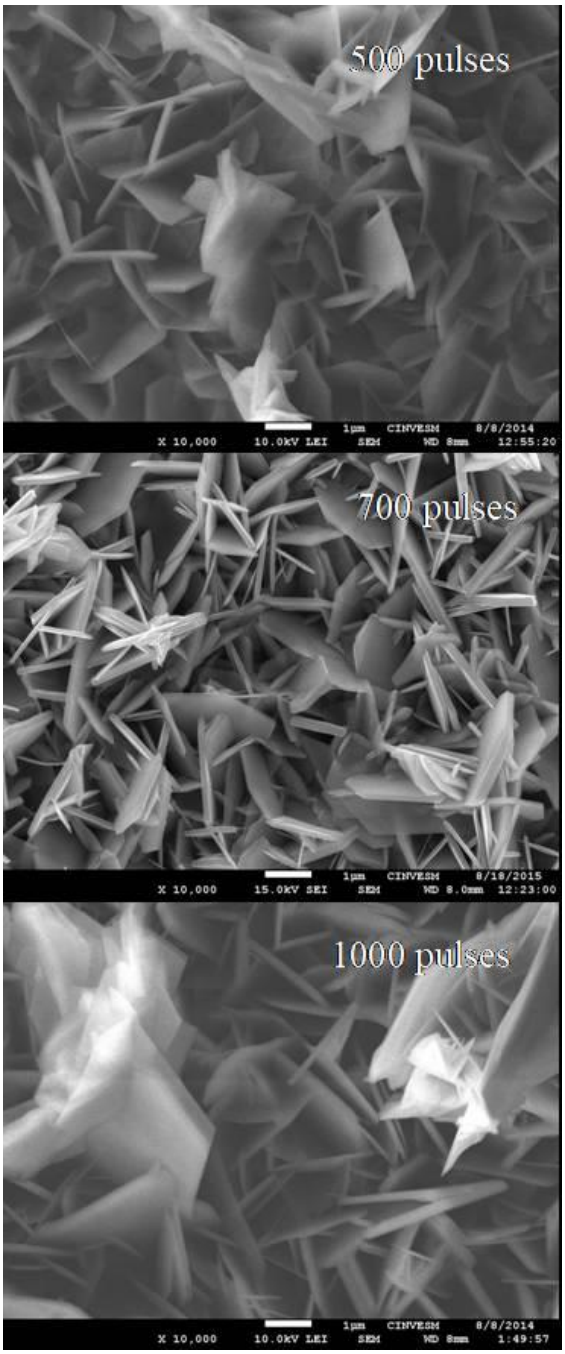

Figure A2.- SEM images of Simonkolleite film electrodeposited from a 0.1 M $Zn(NO_3)_2 \bullet 6H_2O$, 0.1 M KCl aqueous solution at pH= 6.0, 70 °C, the procedure Z2 and changing the number of pulses used.

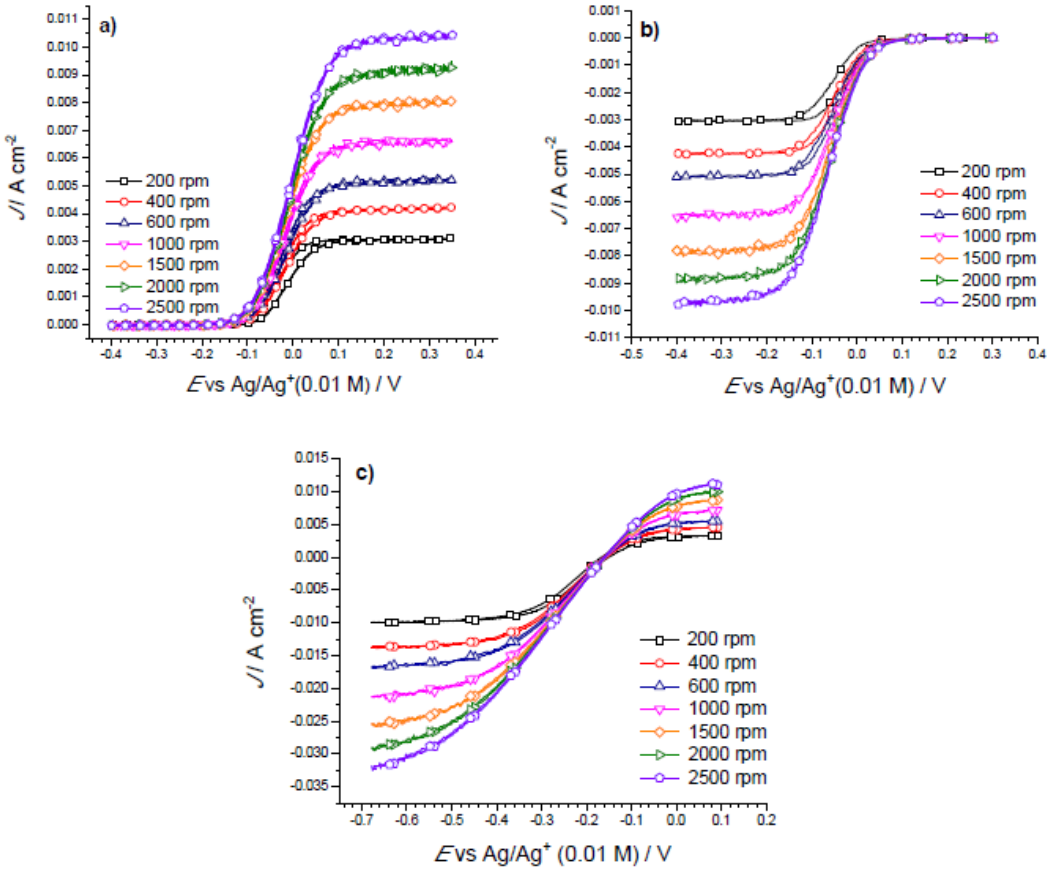

Figure A3. Current-voltage plots for: a) 10 mM $[Co(bpy)_3](PF_6)_2$, b) 10 mM $[Co(bpy)_3](PF_6)_3$, 0.1 M NH_4PF_6 in acetonitrile using a Au-RDE; c) 10 mM I^-, 10 mM I_3^-, 0.1 M NH_4PF_6 in acetonitrile, using a Pt-RDE; all measurements were performed at 25 °C and a 50 mV s^{-1} scan rate.

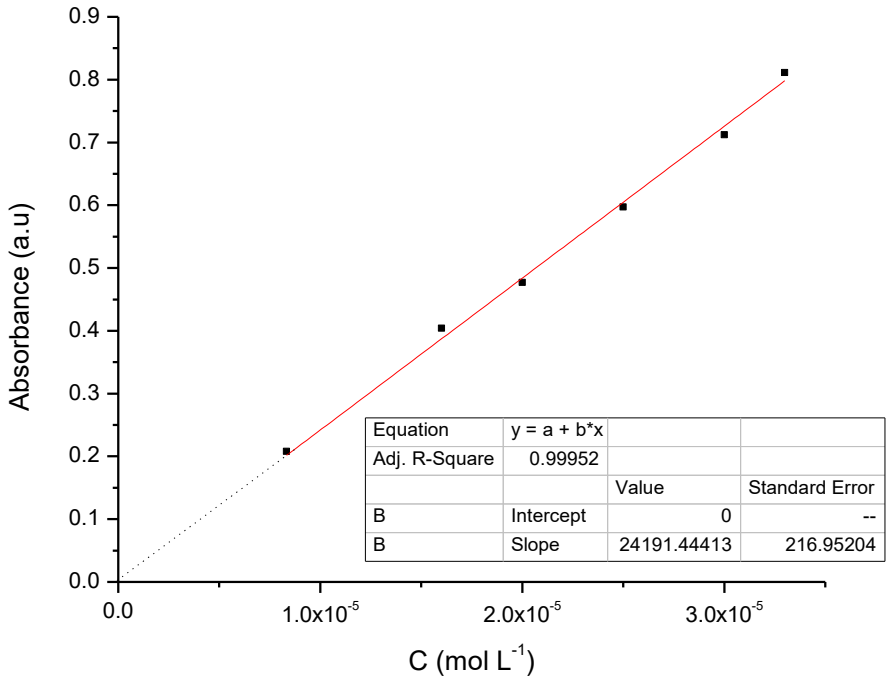

Figure A4.- Absorbance (at 472 nm) in function of the change in concentration of OD-8 acetonitrile/t-butyl alcohol solutions.

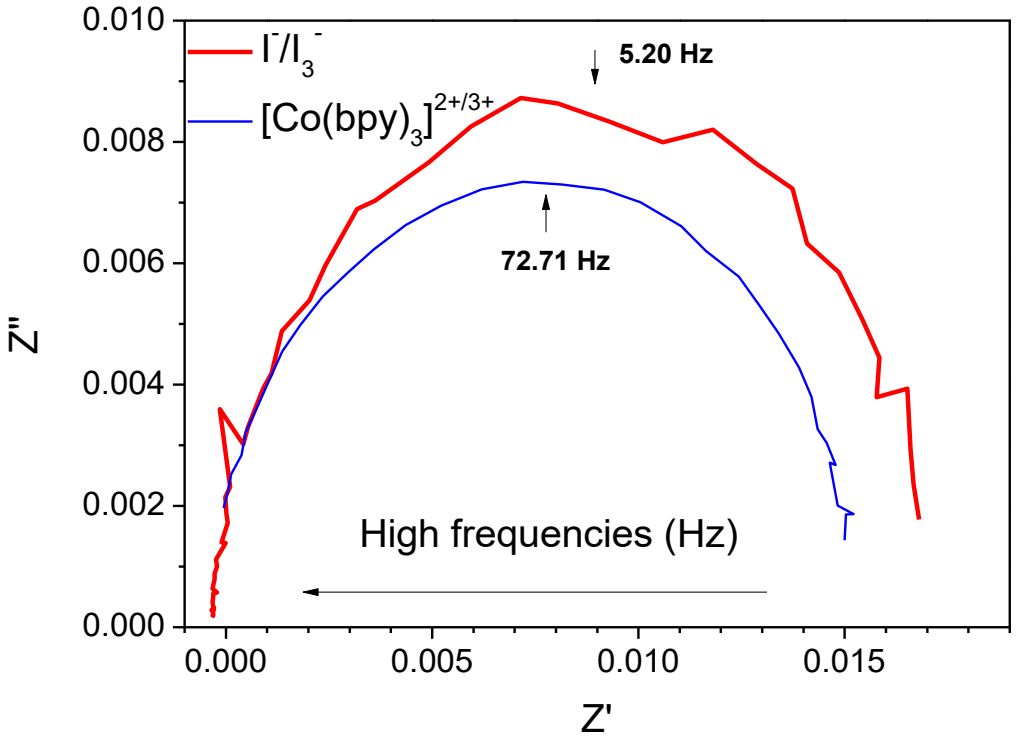

Figure A5.- IMVS Nyquist plots measured at the same light intensity for OD-8 -ZnO DSSCs elaborated with different redox couples. The semicircles were fitted with the use of the Zview software, and the resulting maximum frequencies found related with the electron lifetime as τ_n^{IMVS} α $(\omega^{max})^{-1}$

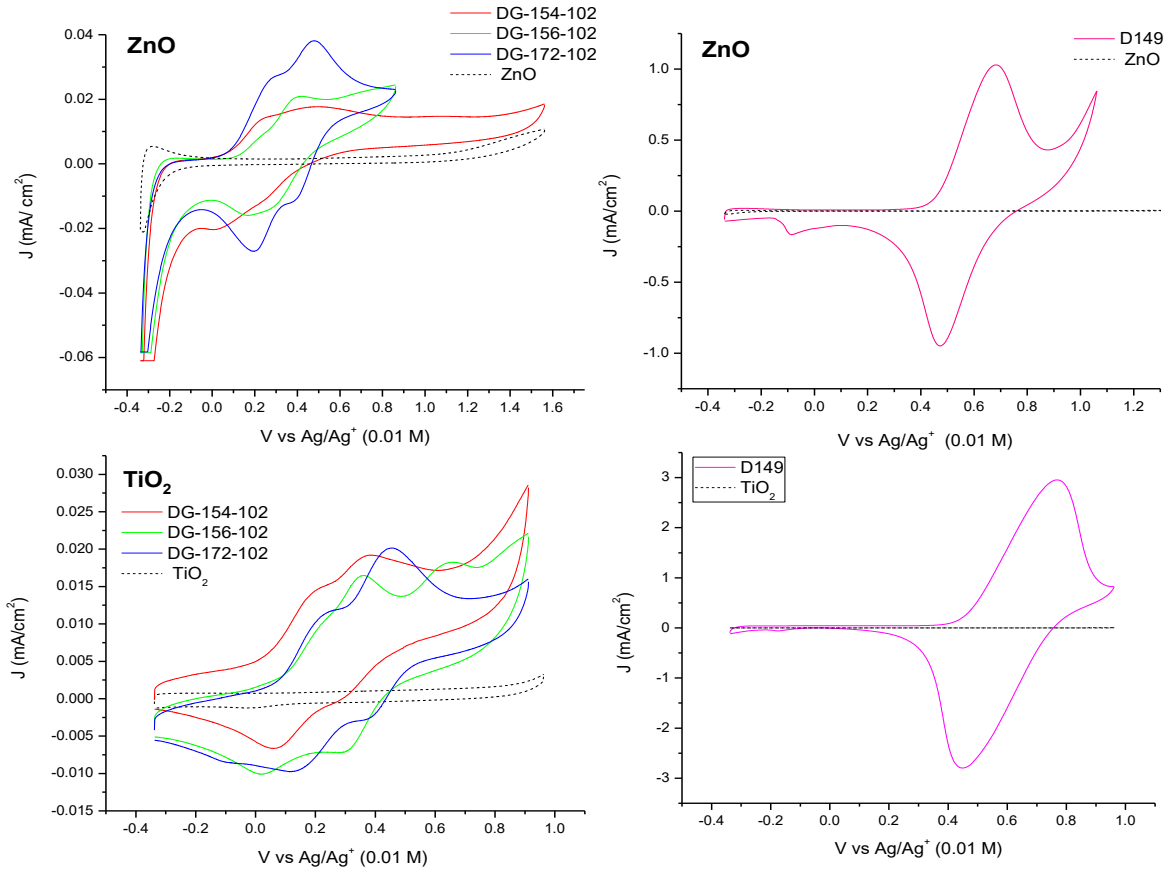

Figure A6. Cyclic voltammetry for the dyes adsorb on TiO_2 and ZnO films as working electrodes, and using Pt and a $Ag/AgNO_3$ (0.01 M) electrode as counter and reference electrode respectively. The experiments were performed at 25 ºC and at a scan rate of 0.1 V s^{-1}.

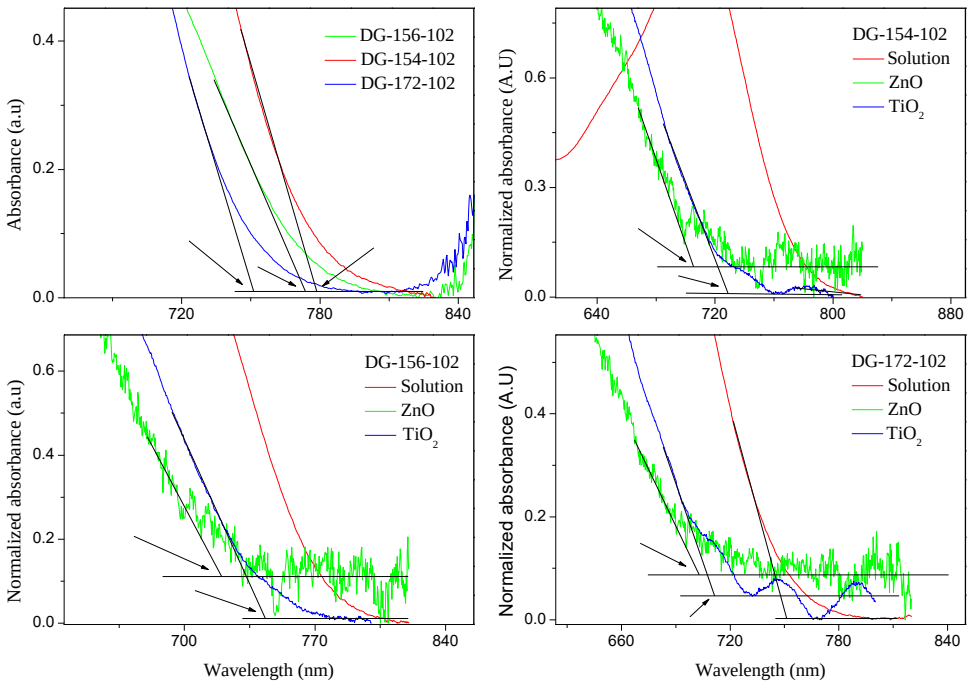

Figure A7. Absorbance spectra of the perylene dyes in solution and adsorbed on ZnO an TiO_2 films.

The black arrows indicate how the absorption onset (λ_{onset}) was graphically calculated.

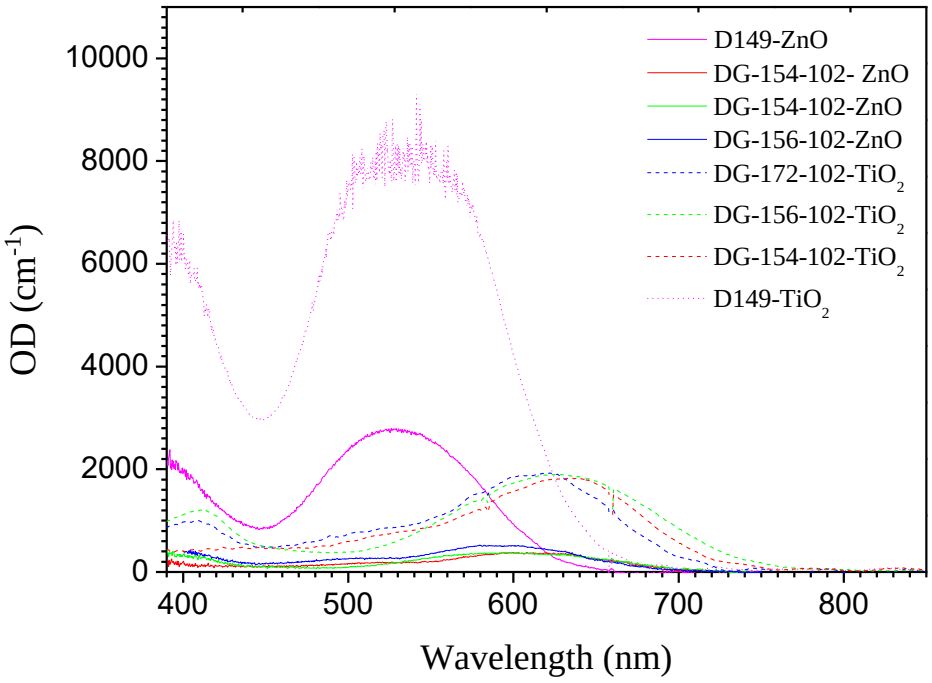

Figure A8. Optical density (OD= absorbance/film thickness) spectra for ZnO and TiO_2 sensitized films.

References

[1] U. Nations, World Population Prospects The 2015 Revision, (2015).

[2] J. Nelson, The physics of solar cells, Imperial College Press, 2003.

[3] B. O'Regan, M. Grätzel, A low-cost, high-efficiency solar cell based on dye-sensitized colloidal TiO2 films, Nature. 353 (1991) 737–740. doi:10.1038/353737a0.

[4] K. Kakiage, Y. Aoyama, T. Yano, K. Oya, J. Fujisawa, M. Hanaya, Highly-efficient dye-sensitized solar cells with collaborative sensitization by silyl-anchor and carboxy-anchor dyes, Chem. Commun. 51 (2015) 15894–15897. doi:10.1039/C5CC06759F.

[5] Q. Zhang, C.S. Dandeneau, X. Zhou, G. Cao, ZnO Nanostructures for Dye-Sensitized Solar Cells, Advanced Materials. 21 (2009) 4087–4108. doi:10.1002/adma.200803827.

[6] K. Keis, C. Bauer, G. Boschloo, A. Hagfeldt, K. Westermark, H. Rensmo, H. Siegbahn, Nanostructured ZnO electrodes for dye-sensitized solar cell applications, Journal of Photochemistry and Photobiology A: Chemistry. 148 (2002) 57–64. https://ac.els-cdn.com/S1010603002000394/1-s2.0-S1010603002000394-main.pdf?_tid=37049399-ad91-4c19-9267-6450542bbd11&acdnat=1520020216_aeb03c6df6224d07a52615c8d5578a66 (accessed March 2, 2018).

[7] K. Keis, E. Magnusson, H.L. Om, S.-E. Lindquist, A. Hagfeldt, A 5% efficient photoelectrochemical solar cell based on nanostructured ZnO electrodes, Solar Energy Materials & Solar Cells. 73 (2002) 51–58. https://ac.els-cdn.com/S0927024801001106/1-s2.0-S0927024801001106-main.pdf?_tid=ce0d8382-eac6-45e0-9bf9-c33fe9819a0e&acdnat=1520019806_bdfdd7799c646c2753147f07b33a1090 (accessed March 2, 2018).

[8] J.A.J. Anta, E. Guille, E. Guillén, R. Tena-Zaera, E. Guillén, R. Tena-Zaera, E. Guille, ZnO-Based Dye-Sensitized Solar Cells, The Journal of Physical …. 116 (2012) 11413–11425. doi:10.1021/jp3010025.

[9] M. Saito, S. Fujihara, Large photocurrent generation in dye-sensitized ZnO solar cells, (2008). doi:10.1039/b806096g.

[10] R. Vittal, K.-C. Ho, Zinc oxide based dye-sensitized solar cells: A review, (2017). doi:10.1016/j.rser.2016.11.273.

[11] S.M. Feldt, E. a. Gibson, E. Gabrielsson, L. Sun, G. Boschloo, A. Hagfeldt, Design of organic dyes and cobalt polypyridine redox mediators for high-efficiency dye-sensitized solar cells, Journal of the American Chemical Society. 132 (2010) 16714–16724. doi:10.1021/ja1088869.

[12] N.S. Lewis, Toward Cost-Effective Solar Energy Use, Proc. Natl. Acad. Sci. U.S.A. Nature. 798 (2007). doi:10.1126/science.1137014.

[13] Solar Spectral Irradiance: Air Mass 1.5, (n.d.). http://rredc.nrel.gov/solar/spectra/am1.5/ (accessed January 28, 2018).

[14] A. Hagfeldt, G. Boschloo, L. Sun, L. Kloo, H. Pettersson, Dye-sensitized solar cells., Chem. Rev. 110 (2010) 6595–6663. doi:10.1002/chem.201101923.

[15] and M.G. M. K. Nazeeruddin, A. Kay, I. Rodicio, R. Humpbry-Baker, E. Muller, P. Liska, N. Vlachopoulos, Conversion of Light to Electricity by cis-XzBis(2,2'-bipyridyl-4,4'-dicarboxylate)ruthenium(11) Charge-Transfer Sensitizers (X = C1-, Br-, I-, CN-, and SCN-) on Nanocrystalline Ti02 Electrodes, J. Am. Chem. SOC. 115 (1993). http://pubs.acs.org/doi/pdf/10.1021/ja00067a063 (accessed January 22, 2018).

[16] K. Keis, J. Lindgren, S. Lindquist, A. Hagfeldt, Studies of the Adsorption Process of Ru Complexes in Nanoporous ZnO Electrodes Studies of the Adsorption Process of Ru Complexes in Nanoporous ZnO Electrodes, (2000) 4688–4694. doi:10.1021/la9912702.

[17] I. Gonzalez-Valls, M. Lira-Cantu, Dye sensitized solar cells based on vertically-aligned ZnO nanorods: effect of UV light on power conversion efficiency and lifetime, Energy & Environmental Science. 3 (2010) 789. doi:10.1039/b922354a.

[18] R. Scholin, M. Quintana, E.M.J. Johansson, M. Hahlin, T. Marinado, a Hagfeldt, H. Rensmo, Preventing Dye Aggregation on ZnO by Adding Water in the Dye-Sensitization Process, Journal of Physical Chemistry C. 115 (2011) 19274–19279. doi:Doi 10.1021/Jp206052t.

[19] N. Shahzad, D. Pugliese, a Lamberti, a Sacco, a Virga, R. Gazia, S. Bianco, M.I. Shahzad, E. Tresso, C.F. Pirri, Monitoring the dye impregnation time of nanostructured photoanodes for dye sensitized solar cells, Journal of Physics: Conference Series. 439 (2013) 1–12. doi:10.1088/1742-6596/439/1/012012.

[20] W.-C. Chang, C.-H. Lee, W.-C. Yu, C.-M. Lin, Optimization of dye adsorption time and film thickness for efficient ZnO dye-sensitized solar cells with high at-rest stability., Nanoscale Research Letters. 7 (2012) 688. doi:10.1186/1556-276X-7-688.

[21] S. Mathew, A. Yella, P. Gao, R. Humphry-Baker, B.F.E. Curchod, N. Ashari-Astani, I. Tavernelli, U. Rothlisberger, M.K. Nazeeruddin, M. Grätzel, Dye-sensitized solar cells with 13% efficiency achieved through the molecular engineering of porphyrin sensitizers, Nature Chemistry. 6 (2014) 242–247. doi:10.1038/nchem.1861.

[22] J. Bisquert, V.S. Vikhrenko, Interpretation of the Time Constants Measured by Kinetic Techniques in Nanostructured Semiconductor Electrodes and Dye-Sensitized Solar Cells, The Journal of Physical Chemistry B. 108 (2004) 2313–2322. doi:10.1021/jp035395y.

[23] J. Bisquert, A. Zaban, The trap-limited diffusivity of electrons in nanoporous

semiconductor networks permeated with a conductive phase, Applied Physics A: Materials Science & Processing. 77 (2003) 507–514. doi:10.1007/s00339-002-1479-4.

[24] G. Boschloo, A. Hagfeldt, Characteristics of the Iodide/Triiodide Redox Mediator in Dye-Sensitized Solar Cells, (2009). doi:10.1021/ar900138m.

[25] G. Oskam, B. V Bergeron, G.J. Meyer, P.C. Searson, Pseudohalogens for dye-sensitized TiO_{2} photoelectrochemical cells, J. Phys. Chem. B. 105 (2001) 6867–6873. doi:10.1021/jp004411d.

[26] Y. Saygili, M. Sö, N. Pellet, F. Giordano, Y. Cao, A. Belen Muñ Oz-García, S.M. Zakeeruddin, N. Vlachopoulos, M. Pavone, G. Boschloo, L. Kavan, J.-E. Moser, M. Grä, A. Hagfeldt, M. Freitag, Copper Bipyridyl Redox Mediators for Dye-Sensitized Solar Cells with High Photovoltage, (n.d.). doi:10.1021/jacs.6b10721.

[27] W. Yang, N. Vlachopoulos, Y. Hao, A. Hagfeldt, G. Boschloo, Efficient dye regeneration at low driving force achieved in triphenylamine dye LEG4 and TEMPO, Physical Chemistry Chemical Physics. 17 (2015) 15868–15875. doi:10.1039/C5CP01880C.

[28] N.W. Duffy, L.M. Peter, R.M.G. Rajapakse, K.G.U. Wijayantha, A novel charge extraction method for the study of electron transport and interfacial transfer in dye sensitised nanocrystalline solar cells, Electrochemistry Communications. 2 (2000) 658–662. doi:10.1016/S1388-2481(00)00097-7.

[29] S. Nakade, T. Kanzaki, Y. Wada, S. Yanagida, Stepped light-induced transient measurements of photocurrent and voltage in dye-sensitized solar cells: Application for highly viscous electrolyte systems, Langmuir. 21 (2005) 10803–10807. doi:10.1021/la051257j.

[30] N. Kopidakis, E.A. Schiff, N.-G. Park, J. Van De Lagemaat, A.J. Frank, Ambipolar Diffusion of Photocarriers in Electrolyte-Filled, Nanoporous TiO 2, (n.d.). doi:10.1021/jp9936603.

[31] L. Kronik, Y. Shapira, Surface photovoltage phenomena: Theory, experiment, and applications, Surface Science Reports. 37 (1999) 1–206. doi:10.1016/S0167-5729(99)00002-3.

[32] J. Zhao, F.E. Osterloh, Photochemical charge separation in nanocrystal photocatalyst films: Insights from surface photovoltage spectroscopy, Journal of Physical Chemistry Letters. 5 (2014) 782–786. doi:10.1021/jz500136h.

[33] F. Lenzmann, J. Krueger, S. Burnside, K. Brooks, M. Grätzel, D. Gal, S. Rühle, D. Cahen, Surface photovoltage spectroscopy of dye-sensitized solar cells with TiO2, Nb2O5, and SrTiO3 nanocrystalline photoanodes: Indication for electron injection from higher excited dye states, Journal of Physical Chemistry B. 105 (2001) 6347–6352. doi:10.1021/jp010380q.

[34] C. Rogero, D.F. Pickup, J. Colchero, E. Azaceta, R. Tena-Zaera, E. Palacios-Lidón,

Nanophotoactivity of Porphyrin Functionalized Polycrystalline ZnO Films, ACS Applied Materials & Interfaces. 8 (2016) 16783–16790. doi:10.1021/acsami.6b03544.

[35] L. Barnea-Nehoshtan, S. Kirmayer, E. Edri, G. Hodes, D. Cahen, Surface Photovoltage Spectroscopy Study of Organo-Lead Perovskite Solar Cells, (n.d.). doi:10.1021/jz501163r.

[36] B. Canava, D. Lincot, Nucleation eff€ ects on structural and optical properties of electrodeposited zinc oxide on tin oxide, Journal of Applied Electrochemistry. 30 (2000) 711–716. doi:10.1023/A:1003857026200.

[37] R. Tena-Zaera, J. Elias, G. Wang, C. Lévy-Clément, Role of Chloride Ions on Electrochemical Deposition of ZnO Nanowire Arrays from O_2 Reduction, J. Phys. Chem. C. 111 (2007) 16706–16711. doi:10.1021/jp073985g.

[38] S. Peulon, Sophie; Lincot, Mechanistic Study of Cathodic Electrodeposition of Zinc Oxide and Zinc Hydroxychloride Films from Oxygenated Aqueous Zinc Chloride Solutions, Journal of The Electrochemical Society. 145 (1998) 864. doi:10.1149/1.1838359.

[39] Z. Chen, Y. Tang, L. Zhang, L. Luo, Electrodeposited nanoporous ZnO films exhibiting enhanced performance in dye-sensitized solar cells, Electrochimica Acta. 51 (2006) 5870–5875. doi:10.1016/j.electacta.2006.03.026.

[40] T. Yoshida, J. Zhang, D. Komatsu, S. Sawatani, H. Minoura, T. Pauporté, D. Lincot, T. Oekermann, D. Schlettwein, H. Tada, D. Wöhrle, K. Funabiki, M. Matsui, H. Miura, H. Yanagi, Electrodeposition of Inorganic/Organic Hybrid Thin Films, Advanced Functional Materials. 19 (2009) 17–43. doi:10.1002/adfm.200700188.

[41] T. Yoshida, H. Minoura, Electrochemical self-assembly of dye-modified zinc oxide thin films, Advanced Materials. 12 (2000) 1219–1222. doi:10.1002/1521-4095(200008)12:16<1219::AID-ADMA1219>3.0.CO;2-5.

[42] T. Yoshida, D. Komatsu, N. Shimokawa, H. Minoura, Mechanism of cathodic electrodeposition of zinc oxide thin films from aqueous zinc nitrate baths, Thin Solid Films. 451–452 (2004) 166–169. doi:10.1016/j.tsf.2003.10.097.

[43] X. Gan, X. Gao, J. Qiu, X. Li, Growth and characterization of ZnO-SDS hybrid thin films prepared by electrochemical self-assembly method, Applied Surface Science. 254 (2008) 3839–3844. doi:10.1016/j.apsusc.2007.12.005.

[44] F.I.L. Tzec, M. a A. Frutis, G.R. Gattorno, G. Oskam, Electrodeposition of ZnO for Application in Dye-sensitized Solar Cells, 215 (2013) 209–215.

[45] F. Hu, Y. Xia, Z. Guan, X. Yin, T. He, Low temperature fabrication of ZnO compact layer for high performance plastic dye-sensitized ZnO solar cells, Electrochimica Acta. 69 (2012) 97–101. doi:10.1016/j.electacta.2012.02.084.

[46] E. Barrera, M.P. Pardavé, N. Batina, I. González, Formation Mechanisms and

Characterization of Black and White Cobalt Electrodeposition onto Stainless Steel, Journal of The Electrochemical Society. 147 (2000) 1787. doi:10.1149/1.1393435.

[47] M.R. Mahmoudian, W.J. Basirun, Y. Alias, M. Ebadi, Facile fabrication of Zn/Zn5(OH)8Cl 2·H2O flower-like nanostructure on the surface of Zn coated with poly (N-methyl pyrrole), Applied Surface Science. 257 (2011) 10539–10544. doi:10.1016/j.apsusc.2011.07.046.

[48] Daniel Melciu Navin Maidee, P. Uta Klement, Pulse-Electroplating: Process Parameters and Their Influence on the Formed Microstructure, (n.d.). http://publications.lib.chalmers.se/records/fulltext/219169/219169.pdf (accessed January 5, 2018).

[49] D.S. M. Rudolph, T. Loewenstein, E. Arndt, Y. Zimmermann, A. Neudeck, Pulsed electrodeposition of porous ZnO on Ag-coated polyamide filaments, Physical Chemistry Chemical Physics. 11 (2009) 3010. doi:10.1039/b905911n.

[50] O. Garcia-Martinez, E. Vila, J.L. Martin de Vidales, R.M. Rojas, K. Petrov, On the thermal decomposition of the zinc(II) hydroxide chlorides Zn5(OH)8Cl2·H2O and B-Zn(OH)Cl, Journal of Materials Science. 29 (1994) 5429–5434. doi:10.1007/BF01171557.

[51] H. Nusbaumer, J.-E. Moser, S.M. Zakeeruddin, M.K. Nazeeruddin, M. Grätzel, $Co^{II}(dbbip)_2^{2+}$ Complex Rivals Tri-iodide/Iodide Redox Mediator in Dye-Sensitized Photovoltaic Cells, The Journal of Physical Chemistry B. 105 (2001) 10461–10464. doi:10.1021/jp012075a.

[52] H. Nusbaumer, S.M. Zakeeruddin, J.-E. Moser, M. Grätzel, An Alternative Efficient Redox Couple for the Dye-Sensitized Solar Cell System, Chemistry - A European Journal. 9 (2003) 3756–3763. doi:10.1002/chem.200204577.

[53] J.-H. Yum, E. Baranoff, F. Kessler, T. Moehl, S. Ahmad, T. Bessho, A. Marchioro, E. Ghadiri, J.-E. Moser, C. Yi, M.K. Nazeeruddin, M. Grätzel, A cobalt complex redox shuttle for dye-sensitized solar cells with high open-circuit potentials, Nature Communications. 3 (2012) 631–639. doi:10.1038/ncomms1655.

[54] J. Fan, Y. Hao, A. Cabot, E.M.J. Johansson, G. Boschloo, A. Hagfeldt, Cobalt(II/III) redox electrolyte in ZnO nanowire-based dye-sensitized solar cells, ACS Applied Materials and Interfaces. 5 (2013) 1902–1906. doi:10.1021/am400042s.

[55] N. Ahmad-Ludin, N. Abdul-Karim, M.A. Mat-Teridi, M.A. Ibrahim, S. Sepeai, K. Sopian, M.Y. Sulaiman, Absorption Spectrum of N719 and SQ1 dye on TiO 2 Surface of Dye- sensitized Solar Cell, (n.d.). http://www.wseas.us/e-library/conferences/2013/Malaysia/RESEN/RESEN-40.pdf (accessed January 11, 2018).

[56] H. Shahroosvand, P. Abbasi, M. Ameri, M. Riahi, Dye-sensitized nanocrystalline ZnO solar cells based on ruthenium(II) phendione complexes, International Journal of Photoenergy. 2011 (2011). doi:10.1155/2011/634147.

[57] H. Horiuchi, R. Katoh, K. Hara, M. Yanagida, S. Murata, H. Arakawa, M. Tachiya, Electron Injection Efficiency from Excited N3 into Nanocrystalline ZnO Films: Effect of (N3−Zn 2+) Aggregate Formation, The Journal of Physical Chemistry B. 107 (2003) 2570–2574. doi:10.1021/jp0220027.

[58] J.A. Anta, J. Idigoras, E. Guillen, J. Villanueva-Cab, H.J. Mandujano-Ramirez, G. Oskam, L. Pelleja, E. Palomares, A continuity equation for the simulation of the current-voltage curve and the time-dependent properties of dye-sensitized solar cells, Physical Chemistry Chemical Physics. 14 (2012) 10285–10299. doi:10.1039/c2cp40719a.

[59] P.R.F. Barnes, K. Miettunen, X. Li, A.Y. Anderson, T. Bessho, M. Gratzel, B.C. O'Regan, Interpretation of optoelectronic transient and charge extraction measurements in dye-sensitized solar cells, Advanced Materials. 25 (2013) 1881–1922. doi:10.1002/adma.201201372.

[60] S. Pelet, J.-E. Moser, M. Gra, Cooperative Effect of Adsorbed Cations and Iodide on the Interception of Back Electron Transfer in the Dye Sensitization of Nanocrystalline TiO 2, (n.d.). doi:10.1021/jp9934477.

[61] Z. Liu, H. Ojima, Z. Hong, J. Kido, W. Tian, X. Wang, Solution-Processed Organic Photovoltaics Based on Indoline Dye Molecules Developed in Dye-Sensitized Solar Cells, (2013) 3107–3117. doi:10.3390/molecules18033107.

[62] T. Edvinsson, C. Li, N. Pschirer, J. Scho, F. Eickemeyer, diger Sens, G. Boschloo, A. Herrmann, K. Mu, A. Hagfeldt, Intramolecular Charge-Transfer Tuning of Perylenes: Spectroscopic Features and Performance in Dye-Sensitized Solar Cells, (2007). doi:10.1021/jp076447c.

[63] M. Planells, F.J. Céspedes-Guirao, L. Gonçalves, A. Sastre-Santos, F. Fernández-Lázaro, E. Palomares, Supramolecular interactions in dye-sensitised solar cells, Journal of Materials Chemistry. 19 (2009) 5818. doi:10.1039/b903682b.

[64] C. Zafer, M. Kus, G. Turkmen, H. Dincalp, S. Demic, B. Kuban, Y. Teoman, S. Icli, New perylene derivative dyes for dye-sensitized solar cells, Solar Energy Materials & Solar Cells. 91 (2007) 427–431. doi:10.1016/j.solmat.2006.10.004.

[65] J. Otsuki, Y. Takaguchi, D. Takahashi, P. Kalimuthu, S.P. Singh, A. Islam, L. Han, Piperidine-Substituted Perylene Sensitizer for Dye-Sensitized Solar Cells, 2011 (2011). doi:10.1155/2011/860486.

[66] S. Nakade, Y. Saito, W. Kubo, T. Kanzaki, T. Kitamura, Y. Wada, S. Yanagida, Enhancement of electron transport in nano-porous TiO 2 electrodes by dye adsorption, (n.d.). doi:10.1016/j.elecom.2003.07.008.

[67] F.I. Lizama-Tzec, R. García-Rodríguez, G. Rodríguez-Gattorno, E.J. Canto-Aguilar, A.G. Vega-Poot, B.E. Heredia-Cervera, J. Villanueva-Cab, N. Morales-Flores, U. Pal, G. Oskam, Influence of morphology on the performance of ZnO-based dye-sensitized solar cells, RSC Adv. 6 (2016) 37424–37433. doi:10.1039/C5RA25618F.

[68] J. Sobus, G. Burdzinki, J. Karolczak, J. Idígoras, J.A. Anta, M. Zioek, Comparison of TiO 2 and ZnO Solar Cells Sensitized with an Indoline Dye: Time-Resolved Laser Spectroscopy Studies of Partial Charge Separation Processes, (n.d.). doi:10.1021/la404782s.

[69] J. Idígoras, G. Burdziński, J. Karolczak, J. Kubicki, G. Oskam, J.A. Anta, M. Ziółek, The Impact of the Electrical Nature of the Metal Oxide on the Performance in Dye-Sensitized Solar Cells: New Look at Old Paradigms, The Journal of Physical Chemistry C. 119 (2015) 3931–3944. doi:10.1021/jp512330f.

[70] V. Thavasi, V. Renugopalakrishnan, R. Jose, S. Ramakrishna, Controlled electron injection and transport at materials interfaces in dye sensitized solar cells, Materials Science and Engineering: R: Reports. 63 (2009) 81–99. doi:10.1016/j.mser.2008.09.001.

[71] C. Nasr†, S. Hotchandani‡, § Prashant V. Kamat*, Role of Iodide in Photoelectrochemical Solar Cells. Electron Transfer between Iodide Ions and Ruthenium Polypyridyl Complex Anchored on Nanocrystalline SiO2 and SnO2 Films, (1998). doi:10.1021/JP9811427.

[72] David W. Thompson, Craig A. Kelly, and Fereshteh Farzad, G.J. Meyer*, Sensitization of Nanocrystalline TiO2 Initiated by Reductive Quenching of Molecular Excited States, (1998). doi:10.1021/LA980809D.

[73] J.M. Gardner, J.M. Giaimuccio, G.J. Meyer, Evidence for Iodine Atoms as Intermediates in the Dye Sensitized Formation of I−I Bonds, Journal of the American Chemical Society. 130 (2008) 17252–17253. doi:10.1021/ja807703m.